**U.S. Army
Environmental
Center**

PULSED ELECTROMAGNETIC INDUCTION (PEMI) SCIENTIFIC AND TECHNICAL REPORT (FINAL)

9 NOVEMBER 1995

Prepared by Alliant Techsystems Inc.

19960322 021

Distribution Unlimited; Approved for Public Release

DTIC QUALITY INSPECTED 1

REPORT DOCUMENTATION PAGE		*Form Approved* *OMB No. 0704-0188*

Public reporting burden for this collection of information is estimated to average 1 hour per response, including the time for reviewing instructions, searching existing data sources, gathering and maintaining the data needed, and completing and reviewing the collection of information. Send comments regarding this burden estimate or any other aspect of this collection of information, including suggestions for reducing this burden to Washington Headquarters Services, Directorate for Information Operations and Reports, 1215 Jefferson Davis Highway, Suite 1204, Arlington, VA 22204-4302, and to the Office of Management and Budget, Paperwork Reduction Project (0704-01881, Washington. DC 20503.

1. AGENCY USE ONLY (Leave Blank)	2. REPORT DATE 9 November 1995	3. REPORT TYPE AND DATES COVERED 8 September 1994 - 8 September 1995	

4. TITLE AND SUBTITLE	5. FUNDING NUMBERS
Pulsed ElectroMagnetic Induction (PEMI) Scientific and Technical Report (Final)	

6. AUTHOR(S)

7. PERFORMING ORGANIZATION NAME(S) AND ADDRESS(ES)	8. PERFORMING ORGANIZATION REPORT NUMBER
Naval Explosive Ordnance Disposal Technology Division Project Engineer: David Gill 301/743-6850 2008 Stump Neck Road Indian Head, Maryland 20640-5070	

9. SPONSORING / MONITORING AGENCY NAME(S) AND ADDRESS(ES)	10. SPONSORING / MONITORING AGENCY REPORT NUMBER
U.S. Army Environmental Center Project Officer: Kelly Rigano 410/612-6868 SFIM-AEC-ETP Aberdeen Proving Ground, Maryland 21010-5401	SFIM-AEC-ET-CR-95092

11. SUPPLEMENTARY NOTES

Supporting Contractor: Alliant Techsystems Inc.
Marine Systems West
6500 Harbour Heights Parkway
Mukilteo, Washington 98275-4844

12a. DISTRIBUTION / AVAILABILITY STATEMENT	12b. DISTRIBUTION CODE
Unlimited Distribution; Approved for Public Release	"A"

13. ABSTRACT (Maximum 200 words)

This report documents the FY95 Pulsed ElectroMagnetic Induction (PEMI) project. This project was a component of the Unexploded Ordnance (UXO) Detection, Identification, and Remediation Advanced Technology Demonstration (ATD) program. Work under the UXO-ATD program began as a result of the new U.S. Government emphasis on Department of Defense reductions and consolidations, the need to close and clean-up military bases and ranges, and return them to the public. The PEMI was one of several projects performed under the UXO-ATD program in support of sensor development to increase the reliability, accuracy, and cost effectiveness of the methods used for UXO detection, identification, and characterization.

The PEMI project included several phases of work: modelling and simulation, assembling data collection hardware, performing a field experiment in March and April 1995 in Washington state, and performing a second field demonstration at the Naval Explosive Ordnance Disposal Technology Division magnetometer test range in Indian Head, Maryland in July 1995. The results of the project indicate that the PEMI method will be useful in UXO remediation efforts. Additional work is required to develop a field prototype that will be able to detect, localize, characterize, and identify UXO.

14. SUBJECT TERMS			15. NUMBER OF PAGES
pulsed electromagnetic induction, time domain electromagnetic method, unexploded ordnance, detection, forward modelling			
			16. PRICE CODE

17. SECURITY CLASSIFICATION OF REPORT	18. SECURITY CLASSIFICATION OF THIS PAGE	19. SECURITY CLASSIFICATION OF ABSTRACT	20. LIMITATION OF ABSTRACT
Unclassified	Unclassified	Unclassified	Unlimited

NSN 7540-01-280-5500

Standard Form 298 (Rev 12-94)
Prescribed by ANSI Sta 239-18
298-102

ALLIANT TECHSYSTEMS

PULSED ELECTROMAGNETIC INDUCTION (PEMI)

CDRL A003
Scientific and Technical Report
September 8, 1994 through September 8, 1995
Contract #N00174-94-C-0083

PULSED ELECTROMAGNETIC INDUCTION (PEMI)

DATA ITEM COVER SHEET

PREPARED BY: _____

P. KACZKOWSKI (APL/UW) 206-543-1283

PREPARED BY: _____

E. J. RISSBERGER (ATK) 206-356-3490

REVIEWED BY: _____

M. C. YOUNG (ATK) 206-356-3184

PULSED ELECTROMAGNETIC INDUCTION (PEMI)
Scientific and Technical Report
September 1995
CDRL A003

Table of Contents

Table of Figures

This page is intentionally left blank

1. Summary

The FY95 Pulsed ElectroMagnetic Induction (PEMI) project was a component of the Unexploded Ordnance Detection, Identification and Remediation Advanced Technology Demonstration Program (UXO-ATD) sponsored by the Army Environmental Center and managed by the Naval Explosive Ordnance Disposal Technology Division (NEODTD) located in Indian Head, Maryland. Work under the UXO-ATD Program began as a result of the new U.S. Government emphasis on Department of Defense reductions and consolidations, and the need to close, clean-up, and return military bases and ranges to the public. This is one of several projects being performed under the UXO-ATD program in support of sensor development to increase the reliability, accuracy, and cost effectiveness of the methods used for UXO detection, identification, and characterization.

The PEMI project was carried out by Alliant Techsystems (ATK), Mukilteo and the Applied Physics Laboratory (APL), University of Washington, Seattle. The project included several phases of work: modeling and simulation, assembling data collection hardware, performing a first field experiment in March/April 1995 in Washington state, and a second field demonstration conducted at the NAVEODTECHDIV magnetometer test range in Indian Head, MD in July 1995.

The problem of efficiently detecting UneXploded Ordnance (UXO) has been rendered difficult by the usually high density of associated clutter from shrapnel and other metallic debris. Techniques currently in use do not provide much information as to the size and nature of the target(s) whose signature is measured. The PEMI method has been successfully used in geophysical prospecting for conductive ore bodies precisely because it does provide more information about the target for classification. The purpose of this program has been to evaluate the PEMI method in the context of the UXO detection and classification problem by modeling and measuring responses from several samples of UXO using Commercial Off-The-Shelf (COTS) equipment if possible. The results of the program confirm that the PEMI method is likely to be very useful in UXO remediation and has provided modeling tools that will make designing a fieldable prototype device possible. The successful application of PEMI to the UXO problem will nevertheless greatly benefit from further adaptation and development of the method, including enhancements to the signal processing, expansion of the UXO response database, as well as the development of specialized hardware.

The PEMI method is an active electromagnetic technique and requires a transmitter system, a receiver system, a positioning system, and signal processing to interpret the data. The method works by setting up a primary magnetic field and then abruptly shutting it off, thereby creating an electromagnetic pulse which induces currents in nearby conductors. The currents decay due to resistive losses, creating a secondary magnetic field which can be detected above the surface of the earth. The rate of decay of the secondary magnetic field contains information about the size, conductivity, and magnetic permeability of the object, and can be used as a classification tool. The PEMI system operates at very low frequencies compared to radar, and thus does not detect changes in the earth's composition. However, the decay time constant is very useful in determining the size of a metallic object. The spatial character of the secondary field can be used to locate the target. This program has applied this method to characterize UXO targets and to test electromagnetic models describing PEMI responses of simple shapes.

Several PEMI models have been developed as part of this program. The primary field model computes the excitation magnetic field given transmitter loop geometry. The target response model and secondary field model are used to compute the received signal from the currents induced in a known target. In this program, targets are modeled as thin conductive rings. The data indicate that such a simple model is useful in parameterizing UXO responses for classification, though it is still too elementary to describe the response in full.

The models are used to interpret data. By fitting a model response to measured data the location and size of the unknown target can be parameterized. In this program, finding an optimal fit is achieved using the Damped Least Squares (DLS) algorithm, which is a well known nonlinear inverse technique.

A PEMI hardware system was configured to make basic measurements of responses from several real UXO. The system included a commercially available transmitter, designed for use in geophysical applications. The commercial receiving coils that were supplied with the transmitter were not suitable for the UXO application since the scale of the problems is very different. UXO responses vary over distances which are very short compared to most geophysical features of interest. Therefore, two sets of 3-axis coils and receiver amplifiers were built for this program. The data was collected using an 8-channel Macintosh based data acquisition system. The data acquisition software was specifically designed for this program to permit in-field monitoring of data quality.

The PEMI receiver is inherently broad band and techniques to improve the signal to noise are an integral part of the system. After increasing transmitter power, the simplest means of reducing random noise is by averaging a number of pulses. Coherent noise such as power line emissions are filtered out using narrow band techniques. However, each of these methods has limits, and a noise cancellation scheme using multiple receivers has been studied and tested as part of this program. The analysis indicates that extremely high coherence between the noise measured by the UXO sensor and the noise detection sensor is required to achieve significant gains in signal to noise ratio. In this program, only 3 to 7 dB improvement was possible.

The PEMI models were first verified in tests held in Mukilteo by comparing them with PEMI data from several aluminum and steel ring test targets. Then 3 different UXO (80mm, 122mm, and 155mm shells) were used as targets and characterized using the thin ring model parameterization. The time constants for the UXO are 14ms, 29ms, and 30ms, respectively. The two large shells have very similar time constants and are not readily differentiable using time constant information alone. Spatial responses led to determination of position and orientation and the tests indicate typical accuracy of better than 10 cm in depth, 5 cm in horizontal location, 5 degrees in tilt with respect to the vertical, and about 10 degrees in bearing.

A blind test was held on the "magnetometer test range" at the NAVEODTECHDIV base, in which three, 10 by 10 meter, sites were surveyed by magnetometer and PEMI sensors. Targets were detected and located in each site using both methods.

2. Introduction

This report documents the proof-of-concept demonstration of an advanced and innovative approach to improve the detection and identification of buried UneXploded Ordnance (UXO) using state of the art electromagnetic induction sensors. The objective of this effort is to demonstrate the capability of the Pulsed Electromagnetic Induction (PEMI) technique to detect and identify UXO. To accomplish the primary objective, the effort was broken into four sub-tasks which formed the basis of the program approach and are outlined below:

1) Develop models to represent the response of UXO to a PEMI sensor.
2) Employ the models as a design aid-in the development of proof-of-concept hardware for demonstration of PEMI performance
3) Perform preliminary PEMI tests on UXO to calibrate models and validate performance
4) Perform blind demonstration of the proof-of-concept PEMI sensor at NAVEODTECHDIV magnetometer test range.

The objectives of this program were successfully met, and are documented in this report.

2.1. Report Organization

This report is organized in accordance with DI-MISC-80711. The remainder of Section 2, **Introduction**, provides a brief discussion of the UXO remediation problem, and a top level description of the pulsed electromagnetic induction (PEMI) technique. Section 3.0, **Methods, Assumptions, and Procedures** , is a more detailed examination of PEMI, in particular providing the mathematical foundation for the material in Section 2.0. A complete description of the analytical models and processing employed by the PEMI sensor is covered in Section 3.1. Section 3.2 gives an overview of the proof-of-concept hardware used to validate PEMI performance. Section 4.0, **Results and Discussion**, documents the results of this effort, including both the model validation tests conducted at Mukilteo Wa. (Section 4.2), and the blind demonstration at NAVEODTECHDIV (Section 4.3). Section 5 summarizes the conclusions reached during this effort, and Section 6 proposes recommendations for further work. The appendixes contain reference material for various activities performed during this effort.

2.2. Description of the UXO Contamination Problem

The UXO contamination problem involves a multitude of complex issues associated with both the technology and logistics of selection of candidate UXO remediation sites, UXO site surveying, UXO hunting and UXO site remediation. Subsequent to the selection of a site for UXO remediation, the initial activities include definition of the mission requirements for the individual site remediation. These mission requirements include the constraints on the intended usage of the site subsequent to the remediation effort, the agreed to validation methods to assure that the site has been remediated to the required level, identification of site specific UXO hunting and remediation equipment, and cost of remediation constraints. The

solution approach to the UXO site survey, UXO hunting and UXO site remediation, as indicated in Figure 1, constitute a complex, coordinated methodology designed to perform the best possible remediation error within the cost, schedule, and risk constraints.

1.	**Planning, requirements, site analysis, risk assessments**

2.	**Survey, search, detect, classify, and locate** o GPR, magnetometer, electromagntetic induction o Helo, vehicle, handheld

3..	**Area and point clearance** o Pick,shovel, backhoe, etc

4.	**Disposal** o Point detonation o Remote detonation/demil

5.	**Restoration** o Recontouring, replanting o Soil stabilization
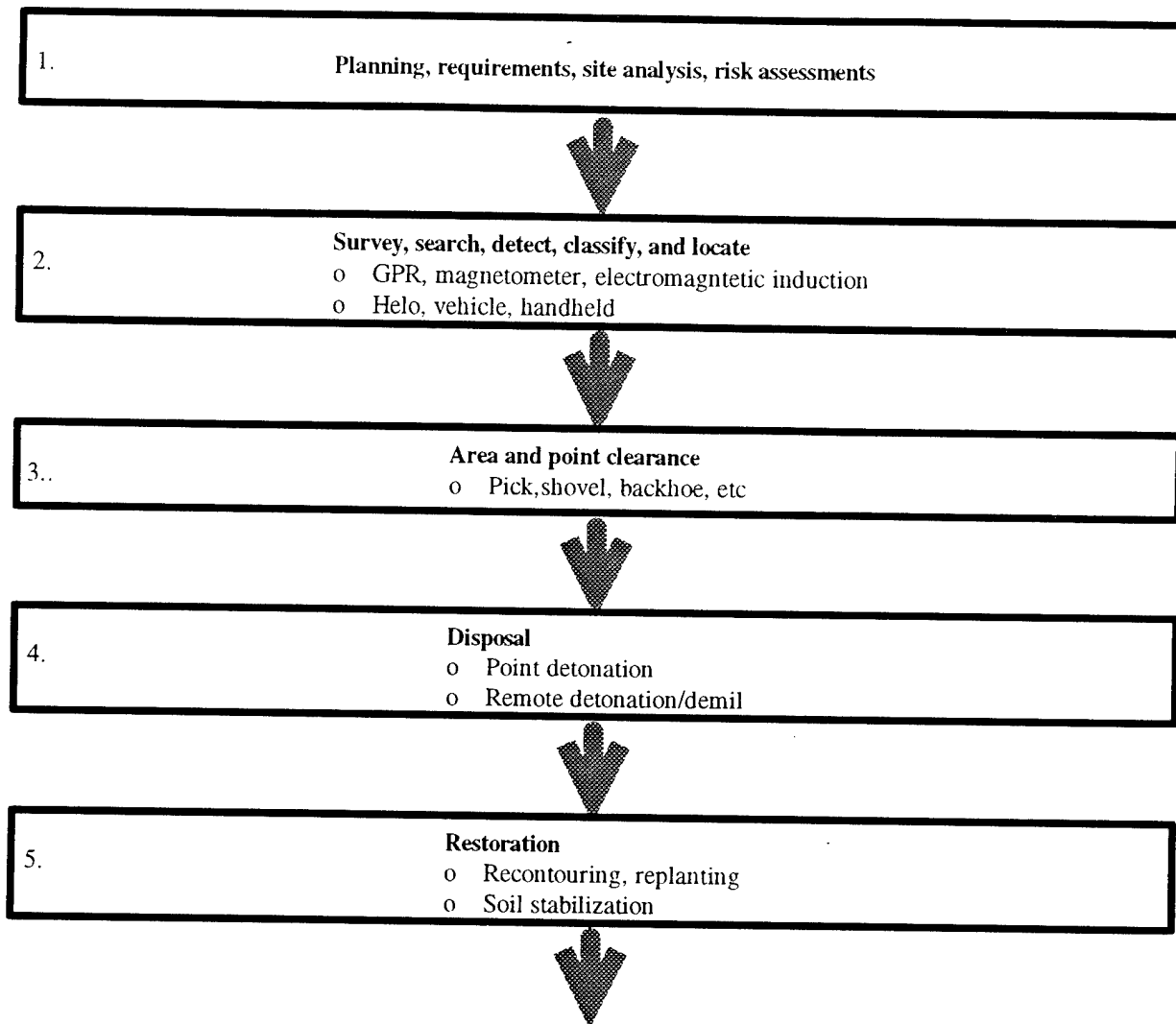
Figure 1: Five Steps of the UXO Remediation Process (A PEMI sensor system for Step #2 is this programs focus).

During the initial site analysis and survey, historical as well as physical information is reviewed and analyzed. The objective of this phase is the identification of the scope of remediation effort based on the sites history as well as the physical constraints imposed by the terrain and geophysical characteristics of the site.

The results of the initial sites analysis are then compared with the remediation objective of the sites and a plan to perform an initial detailed site survey is prepared. This is the first stage of step 2, UXO hunting. A variety of sensing methodologies can be employed in this phase to identify the most promising areas for further UXO hunting. The primary objective of this phase is to provide a good characterization of the areas and to reduce the overall area where more detailed UXO hunting is performed.

For those areas identified as being of high priority for remediation and as having a high UXO contamination potential, a high resolution survey is performed. The objective of this phase is the detection, localization, and classification of the UXOs with sufficient confidence that the time consuming and expensive activities of remediation of the UXO are initiated. This requires a high probability of correct detection/location/classification as well as a low probability of false detection/localization/classification. While the sensors and signal processing selected for UXO hunting can be site dependent, the generic performance of the sensor system must satisfy some basic requirements to be considered effective. It is obvious that an effective sensor system must have a high probability of detection (i.e. Identify that a UXO is present when a UXO is present). However, it is equally important that the sensor have a low probability of false alarm (i.e. Identify that a UXO is present when a UXO is not present). High false alarm rates (FAR) can significantly increase the cost of clearance operations (i.e. Step 3), and reduce confidence in the detection/classification process. Figure 2 illustrates the impact of FAR for a site with an average of six UXO's per acre (or an average of 1.4×10^{-4} UXO's per square foot), e.g., as found on Kaho'olawe in the Hawaiian Islands.

The curve is based on a simple application of Bayes' formula:

$$P(O|D) = \frac{P(O)P(D|O)}{P(O)P(D|O) + P(\theta)P(D|\theta)} \qquad (2\text{-}1)$$

Where

$P(O|D) = $ Confidence in detection
Probability that UXO is present
when a detection occurs

$P(O) = $ Probability that a UXO is present
at that specific location

$P(D|O) = $ Correct Detection Probability
Probability that detection occurs when
a UXO is present

$P(\vartheta) = $ Probability that a UXO is not
present at that specific location

$P(D|\vartheta) = $ False alarm rate; probability that
a detection occurs when a UXO is
not really present

PULSE ELECTROMAGNETIC INDUCTION (PEMI)
N00174-94-C-0083
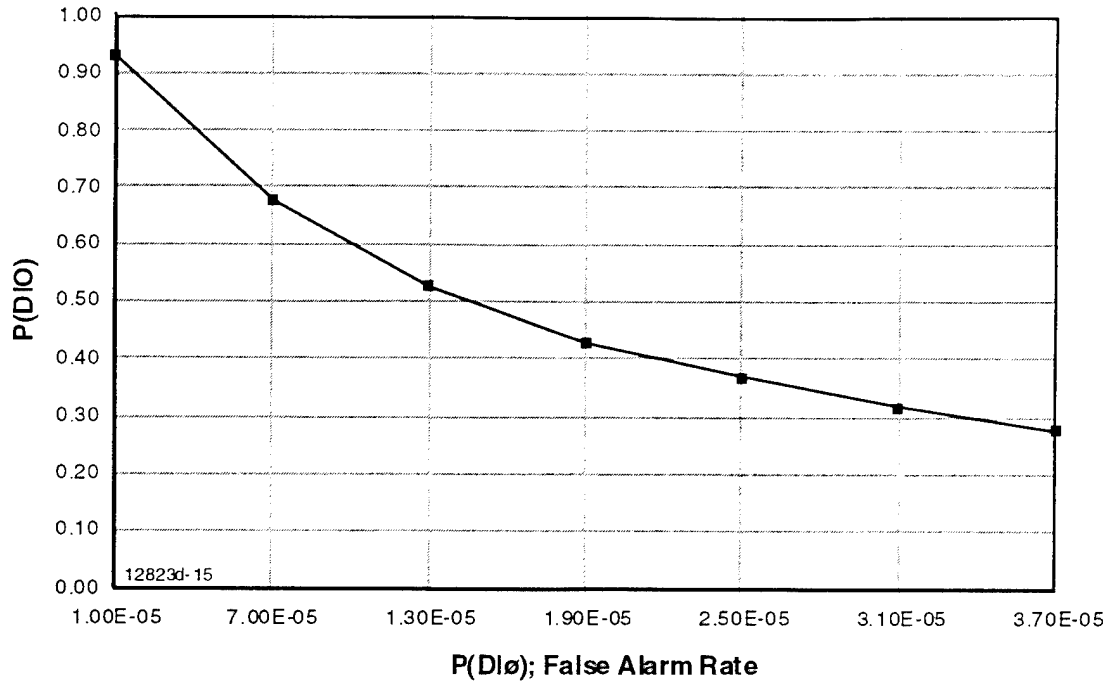
Figure 2: Probability that a detection is a UXO (Bayes Formula Model for P(DIO) = 0.99 and P(O) = 1.4X10^{-4})

The probability that a UXO is actually present for any detection is less than 30% if the FAR is greater than 3.1 X 10^{-4}. The curve shown is for a probability of detecting a UXO of 99%. To interpret these results further, consider an area which must be remediated and contains 100 UXO. The sensor system represented in the figure would produce about 300 detection's which would require clearance (i.e. step 3). Of the 300 clearance areas 99 would contain UXO, and 201 would contain something else. Finally, after remediation there would remain a single undiscovered UXO.

This simple example illustrates two of the fundamental issues which must drive the development of any UXO hunting system. Firstly, a high probability of detection is required to ensure clearance of nearly all the UXO. Secondly, an extremely low false alarm rate is required to make the clearance economically feasible. Satisfying point number one requires an extremely sensitive detection and coarse localization system. Furthermore, the system will need to be capable of searching large areas quickly. Satisfying point number two requires an effective classification system, which does not necessarily have to be quick since it need only look at those areas which have been previously determined to contain a detection. It is not a requirement that the same sensor system be used to meet both these criterion. In fact, it is highly unlikely that a single sensor can be developed which meets both these goals. A more reasonable approach is two sensors, each of which is optimized to either detection or classification.

In this program we have investigated the potential of Pulsed Electromagnetic Induction (PEMI) for UXO hunting. While PEMI can be used in search applications, its most promising application is in classification. This is because it detects a critical UXO parameter, the late time constant, which is directly dependent on object size. This critical classification clue can enable a substantial reduction in the number of false alarms, and consequently the number of excavations which must be performed, during UXO remediation of a site.

2.3. Description of Pulsed Electromagnetic Induction (PEMI)

The very large electrical conductivity contrast between metals, soil, and rock makes electromagnetic induction a promising technique for UXO hunting. Electrical currents can be readily induced in a UXO by immersion in a time varying magnetic field (Primary Field). This is due to the highly conductive nature of a UXO (since a significant portion of the object is metallic). The currents induced in the UXO in turn create a secondary magnetic field which can be detected by a receiver coil. The temporal and spatial variation of the secondary magnetic fields contain information about the conductor, such as position, size, and conductivity.

In PEMI, the primary current waveform is essentially a step function. Hence, the method inherently makes use of information from a wide spectrum of frequencies. Consider a horizontal transmitter loop above a single conductive body, as represented in figure 3A. The primary current in the transmitter coil is a series of pulses as illustrated in figure 3B. During the transmitter on time, the current in the transmitter loop reaches a constant value, creating a constant primary magnetic field in the vicinity of the target conductor. The primary magnetic field exists in all space but is strongest near the transmitter, as indicated by the density of field lines in figure 3A. When the transmitter current is rapidly turned off, the primary magnetic field is turned off, creating a large electromotive force (emf) by Faraday's law. This emf drives an induced current pulse in the conductor. The induced current is such that, at the instant after turn off, the magnetic field within the confines of the conductor is the same as it was when the primary current was on. Immediately afterwards, resistive losses cause the secondary currents to decay with time, leading to further induction of other currents within the target.

The pulse response of a solid conductor is conveniently divided into three time intervals, each of which corresponds to a different response mechanism[1,2]. PEMI responses are typically categorized as early time, late time, and intermediate time. The latter is merely the transition between the two limiting regimes. The induced response has different properties in each time stage, with greatest sensitivity to target bulk parameters found in the late stage.

At turn off, the primary field currents form on the outside of the conductor in such a way as to exactly preserve the magnetic field that was inside the conductor before turn off. In the very early instants after turn off, the induced currents are confined to the outermost parts of the conductor. This is consistent with the idea that early time can be thought of as corresponding to very high frequencies. At high frequencies the skin effect prevents currents from penetrating into the conductor. During this stage, it is clear that the current distribution depends on the primary field and on the external shape of the conductor, but is independent of its conductivity.
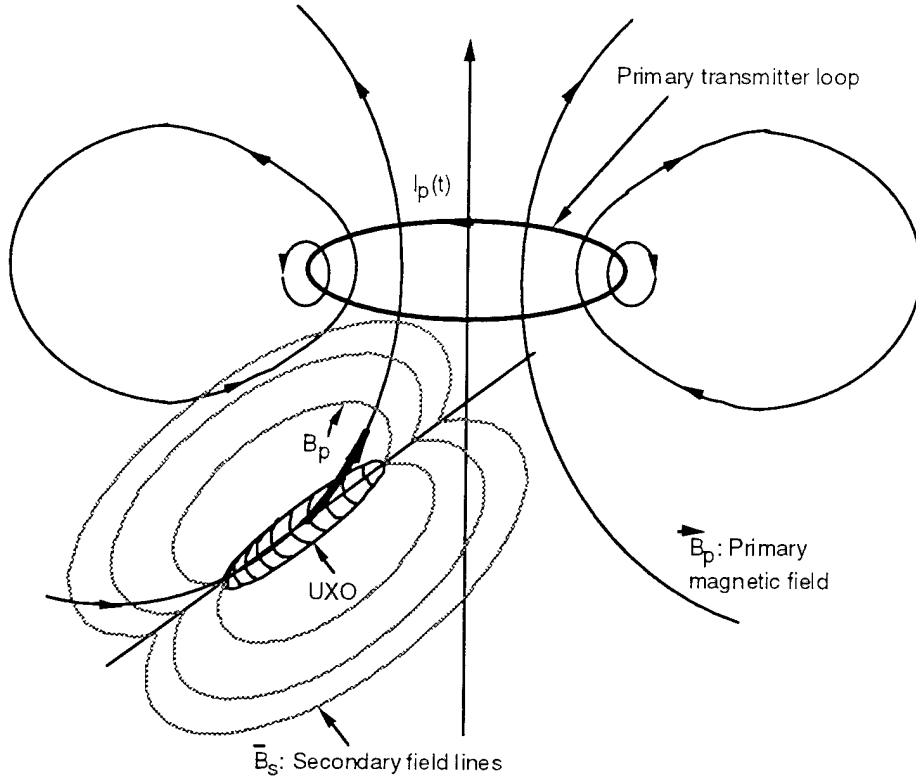
12823-6

Figure 3A: Transmitter Loop Above Conductive Target
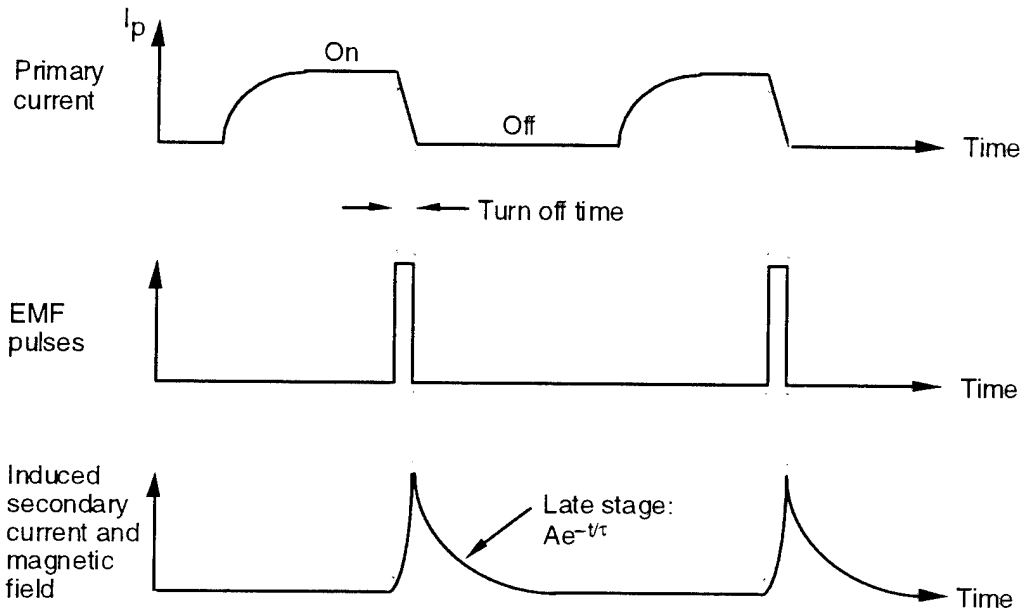
12823d-5

Figure 3B: PEMI Waveforms

The surface currents are soon attenuated by resistive losses and begin decaying with time, thereby inducing other currents further inside the conductor. As time progresses, the distribution of currents changes to include the entire conductor. This diffusion of currents happens during the intermediate time stage. As this diffusion process subsides, the spatial distribution of the currents stabilizes, and all currents merely decay at the same exponential rate. We refer to this as the late time stage. The time constant characterizing this "late stage" exponential decay is determined by the overall size, shape, and conductivity of the buried object. In the case of metallic objects made from uniform material, the conductivity is the same; consequently, only the size and shape determine the time constant, τ.

Kaufman[3] shows that the induced current response of a confined conductor to an emf pulse is a combination of infinitesimal current loops, each of which follows a path with some resistance R_n and some inductance L_n. The current in a simple RL circuit decays exponentially with time as $I(t) = Ae^{-t/\tau}$, where $\tau=L/R$. Thus, the combined current decays as a sum of exponentials with different decay rates, until such time that only the currents with longest time constants dominate the response. The currents exist throughout the conductor in a complicated distribution making formal evaluation of the effective resistance and inductance for all current paths difficult. Nevertheless, for solid cylindrical symmetric bodies, a simple conductive loop circuit of radius a, with inductance L and resistance R, is often a satisfactory late stage model; as shown in Figure 4. Indeed, a current in such a loop decays exponentially as $I(t) = Ae^{-t/\tau}$. The late stage behavior for confined conductors allows straightforward characterization of the conductor from measurements of the secondary magnetic field which must also decay with the same exponential time dependence.
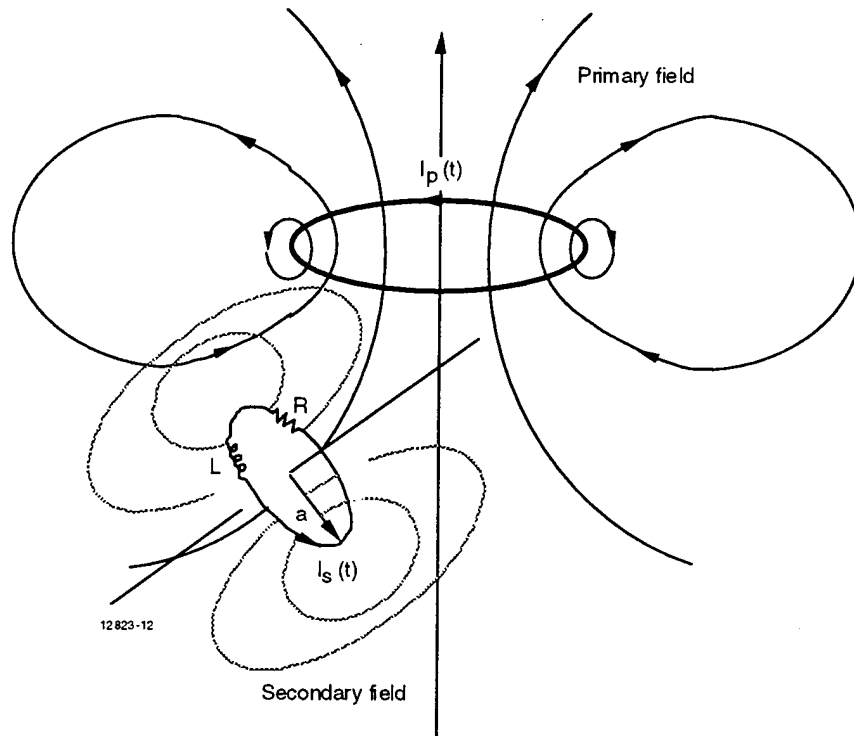
Figure 4: Conductive Loop Model for Solid Target

9

This page is intentionally left blank

3.   Methods, Assumptions, and Procedures

3.1.   PEMI Methods and Models

The PEMI method and models employed in this effort are detailed in this section. The "forward" models are used to compute PEMI responses given knowledge of the transmitter and receiver locations as well as of the model target parameters such as size, location, and orientation. The interpretation of data is also done using these forward models. The process of finding an optimal model fit to data is facilitated by the Damped Least Squares (DLS) algorithm. This algorithm automates iteration of the forward models until a good fit to the data is found and is quite general. In this application, UXO data are fit using a thin conductive ring target model. This simple model is shown in Chapter 4 to be a good parametric representation of the UXO for modeling PEMI responses.

3.1.1. PEMI Forward Modeling

This section describes the modeling of a target conductor's response to a pulsed electric current in a transmitter loop, and its subsequent measurement by a receiver coil. This consists of several models linked together as shown in Figure 5. The primary field model calculates the magnetic field at the known target location due to the primary current in the transmitter loop. When the primary current is turned off, the resultant magnetic flux change produces an electromotive force (emf) which induces a secondary electric current in the target conductor. The induced secondary current and its decay is modeled in the target response model. The changing magnetic field from this decaying secondary current, and the voltage measured by a receiver loop, are modeled in the secondary field model. These models are described in Sections 3.1.1.1-3.1.1.3. The response of the ground to a pulsed emf is computed in the earth response model which is discussed in section 3.1.1.4.
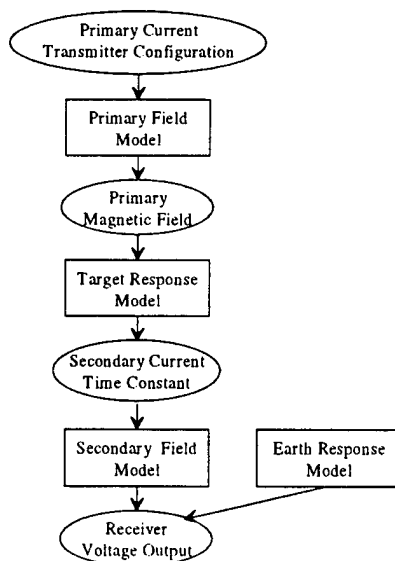
Figure 5: PEMI Forward Models

3.1.1.1. Primary Field Model

The primary field model computes the magnetic field due to a current in a transmitter loop. Models for three transmitter loop configurations: a magnetic dipole, a circular loop and a rectangular loop, are implemented.

The basic equation used in these models is the Biot-Savart law[4] which calculates the magnetic intensity $(\vec{H})$ at a point $\vec{r}$ due to the electric current by integrating along the transmitter loop,

$$\vec{H}(\vec{r}) = \frac{nI}{4\pi} \oint \frac{d\vec{l}_1 \times (\vec{r} - \vec{r}_1)}{\left| \vec{r} - \vec{r}_1 \right|^3} \tag{3.1}$$

where $d\vec{l}_1$ is an infinitesimal element along the transmitter loop, $\vec{r} - \vec{r}_1$ the location of that element relative to $\vec{r}$, I the current in the transmitter loop, and n the number of turns in the loop.

At locations far away from the transmitter, the magnetic field can be approximated by that of a magnetic dipole with a magnetic moment $\vec{M} = nI\vec{A}$, $\vec{A}$ being the area vector of the dipole. With the dipole located at the origin, Eqn. 3.1 is reduced to

$$\vec{H}(\vec{r}) = \frac{1}{4\pi} \left[-\frac{\vec{M}}{r^3} + \frac{3(\vec{M} \cdot \vec{r})\vec{r}}{r^5} \right] \tag{3.2}$$

For a rectangular loop with half-lengths A and B, and centered at the origin, $(\vec{H})$ can be written as the sum of four fields.

$$\vec{H}(\vec{r}) = \sum_{s=1}^{4} \vec{H}_s(\vec{r}), \text{ where}$$

$$\vec{H}_1(\vec{r}) = \frac{nI}{4\pi} \left\{ \frac{x+A}{\left[(x+A)^2 + (y+B)^2 + z^2\right]^{1/2}} - \frac{x-A}{\left[(x-A)^2 + (y+B)^2 + z^2\right]^{1/2}} \right\} \Psi_{1p}$$

$$\vec{H}_2(\vec{r}) = \frac{nI}{4\pi} \left\{ \frac{-(x+A)}{\left[(x+A)^2 + (y-B)^2 + z^2\right]^{1/2}} + \frac{x-A}{\left[(x-A)^2 + (y-B)^2 + z^2\right]^{1/2}} \right\} \Psi_{2p}$$

$$\vec{H}_3(\vec{r}) = \frac{nI}{4\pi} \left\{ \frac{y+B}{\left[(x+A)^2 + (y+B)^2 + z^2\right]^{1/2}} - \frac{y-B}{\left[(x+A)^2 + (y-B)^2 + z^2\right]^{1/2}} \right\} \Psi_{3p}$$

$$\vec{H}_4(\vec{r}) = \frac{nI}{4\pi} \left\{ \frac{-(y+B)}{\left[(x-A)^2 + (y+B)^2 + z^2\right]^{1/2}} + \frac{y-B}{\left[(x-A)^2 + (y-B)^2 + z^2\right]^{1/2}} \right\} \Psi_{4p}$$

$$\Psi_{1p} = \frac{-z\hat{j} + (y+B)\hat{k}}{(y+B)^2 + z^2}$$

$$\Psi_{2p} = \frac{-z\hat{j} + (y - B)\hat{k}}{(y - B)^2 + z^2}$$

$$\Psi_{3p} = \frac{-z\hat{i} + (x + A)\hat{k}}{(x + A)^2 + z^2}$$

$$\Psi_{4p} = \frac{-z\hat{i} + (x - A)\hat{k}}{(x - A)^2 + z^2} \qquad (3.3)$$

where $\hat{i}, \hat{j}, \hat{k}$ are unit vectors in the x, y and z directions, respectively.

For the circular loop with radius a centered at the origin, $\vec{H}$ at location $\vec{r} = (x,y,z)$ is computed by integrating over the polar angle θ (see figure 6).

$$H(\vec{r}) = \frac{nIa}{4\pi} \int_0^{2\pi} \frac{\left[z\cos\theta\,\hat{i} + z\sin\theta\,\hat{j} + (a - x\cos\theta - y\sin\theta)\hat{k} \right]}{\left[a^2 + x^2 + y^2 + z^2 - 2a(y\sin\theta + x\cos\theta) \right]^{3/2}} d\theta \qquad (3.4)$$
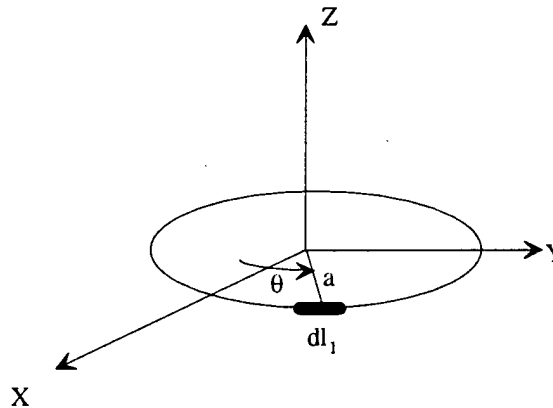
Figure 6: Illustration of polar angle integration

Figure 7 shows an example of the spatial distribution of the magnetic field due to a square transmitter loop. The vertical axis represents the amplitude of the magnetic field components (H_x, H_y and H_z) on a horizontal (x,y) grid at a depth of 2 m (z=-2). The transmitter is a 5 x 5 m^2 square loop lying on the ground (z=0) and centered at the origin. There are 14 turns in the transmitter and it carries an anticlockwise current of 17 amperes. These transmitter parameters correspond to the baseline transmitter configuration for the Mukilteo PEMI field test.

12
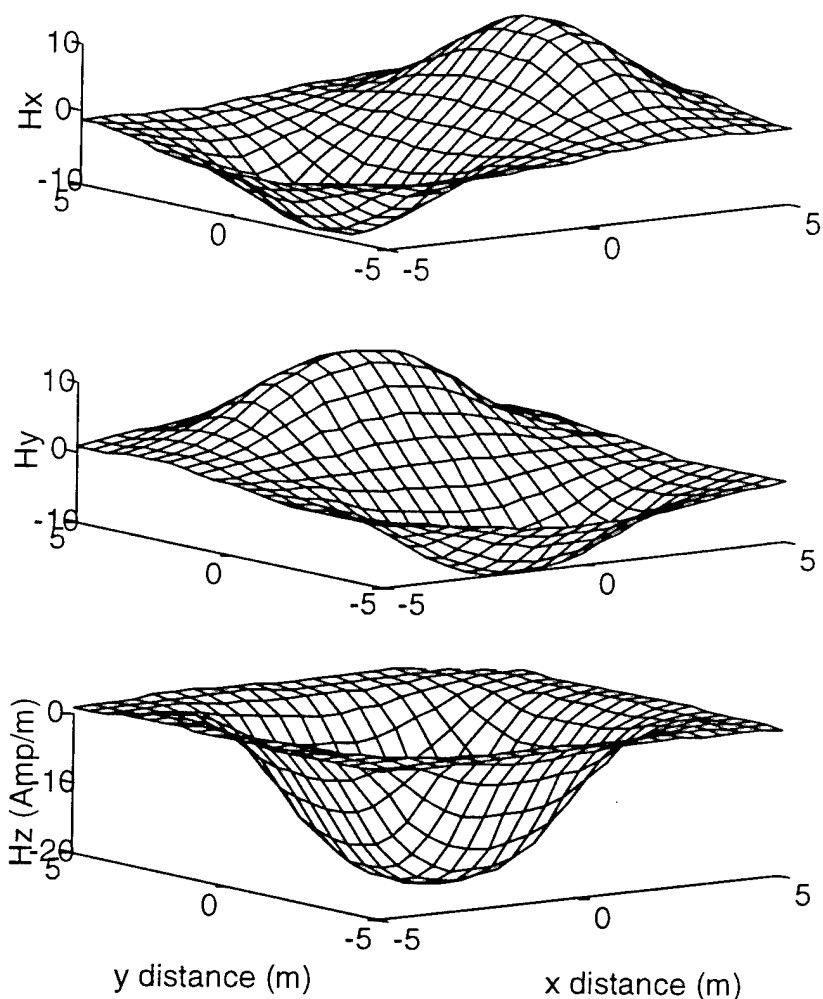
Figure 7: Example of magnetic Field Components (Hx, Hy, Hz) due to a current in a square transmitter loop.

3.1.1.2. Target Response Model

According to Faraday's law of electromagnetic induction, an electromotive force (emf) is associated with changes in magnetic flux through the target conductor. This induces an electric current in the conductor. The response of the conductor to a pulsed emf can be divided into three time regimes: early, late, and intermediate times (Kaufman, 1978). The induced response has different properties in each time stage, with greatest sensitivities to bulk target parameters in the late stage.

At the turn off of the primary field, currents form on the outside of the target conductor in such a way as to preserve the magnetic field just before the turn off (Lenz's law). Due to the skin effect, currents initially are confined to the outermost part of the conductor. During this stage,

the current distribution depends on the primary field and the external shape of the conductor, but is independent of its conductivity.

The surface currents are soon attenuated by resistive losses and begin decaying with time. This induces other currents further inside the conductor. Over time, the distribution of currents changes to include the entire conductor. This diffusion of currents happens in the intermediate time stage. As the diffusion of currents subsides, the spatial distribution of the currents stabilizes, and the currents decay exponentially. This is the late time stage. The time constant of this late stage exponential decay is determined by the size, shape and conductivity of the target.

Kaufman (1978) shows that the induced current response of a confined conductor to a pulsed emf is a combination of many current loops, each of which follows a path with a resistance R and inductance L. The current in a simple RL circuit is computed by solving the equation

$$emf = -\frac{d\Phi}{dt} = L\frac{dI}{dt} + RI \qquad (3.5)$$

where Φ is the magnetic flux through the conductor. The solution for I is

$$I(t) = \frac{\Phi}{L}e^{-t/\tau} \qquad (3.6)$$

with a decay time constant

$$\tau = L/R. \qquad (3.7)$$

The combined current decays as a sum of exponentials with different decay rates, until such time that only the current with the longest time constant dominates the response.

For this PEMI project, a thin conductor circuit loop is used for modeling of the target response. The resistance of the conductor is

$$R = \rho\ell/A \qquad (3.8)$$

where A is the cross sectional area of the conductor, ρ the resistivity of the material and ℓ the length of the loop. The inductance L of the thin conductor loop is

$$L = \mu_0 a[\ln(8a/b) - 1.75] \qquad (3.9)$$

where
      a = radius of the loop
      b = cross sectional radius of the conductor wire (assumed to be circular)
      μ_0 = permeability of free space.

3.1.1.3. Secondary Field Model

The induced current in the target conductor produces a secondary magnetic field. As the current decays, the changing secondary magnetic field can be measured by a receiver coil(s). The secondary magnetic field and receiver voltage are computed in the secondary field model.

The secondary magnetic field due to the induced current in a target with an arbitrary tilt angle θ and orientation φ is computed in two steps. First the magnetic field relative to the target coordinate system is computed, using the computer codes developed for the primary field model. The magnetic field is then translated and rotated to the coordinate system of the receiver. Both the magnetic field vector components and the location coordinates have to be transformed. Tilt and orientation are defined in Figure 8.
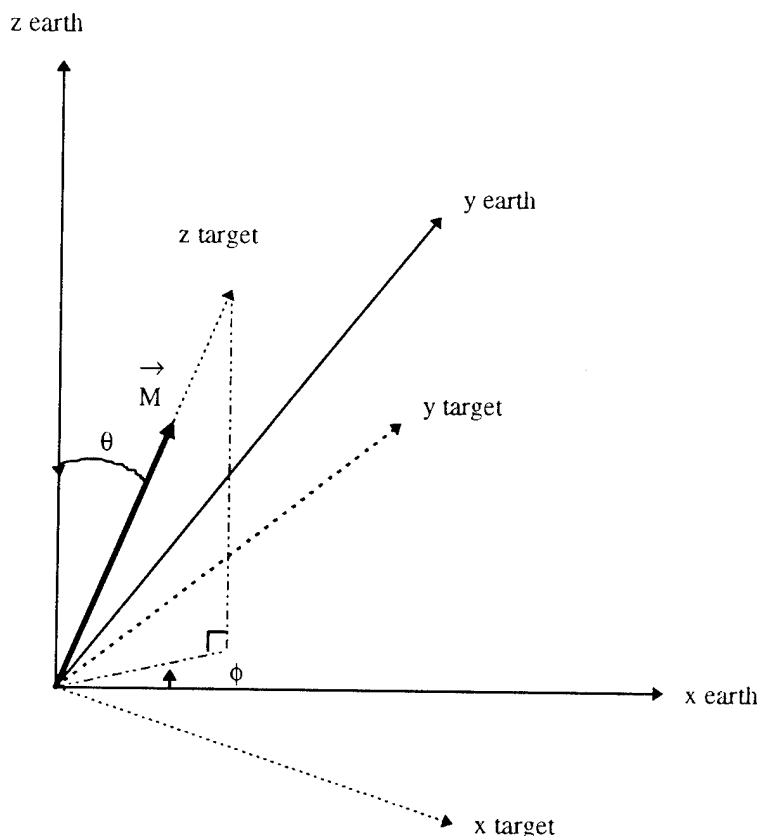
Figure 8: Definition of Coordinate System Used in PEMI Models

A receiver with three orthogonal wire loops is used to measure the emf due to the changing secondary magnetic field from the induced current in the target conductor. With the secondary magnetic field having the same time constant as the induced current, the output of a three-axis receiver loop is

$$V_i = -\frac{\partial \Phi_i}{\partial t} = \frac{\mu}{\tau}(\vec{H} \cdot \vec{A})_i \qquad (3.10)$$

where i=1, 2, 3 represents the x,y,z axes, respectively. Amplifier and signal processing gains for the actual PEMI system used in the field tests are also included in the model.

The secondary field model computes receiver voltage either as a function of time at a specified location or at a specified time at several locations, showing the temporal and spatial responses, respectively. Examples of the response are shown in Figures 9A and 9B. In the examples, a 5x5 m^2 transmitter loop with 14 turns is laid on the ground (z=0). The target is a thin aluminum ring lying flat ($\phi=\theta=0$) at a depth of 2 m directly below the center of the transmitter loop, (i.e., target location (x,y,z) = (0,0,2)). The radius of the ring loop is 23 cm and the cross sectional radius of the wire is 2.6 cm. An anticlockwise pulsed current of 17 A is sent through the transmitter loop. The receiver consists of three perpendicular square loops each with 200 turns, each of which has an enclosed area of 0.25 m^2. The modeled receiver outputs include an amplifier and processing gain of 1000 and 4, respectively.
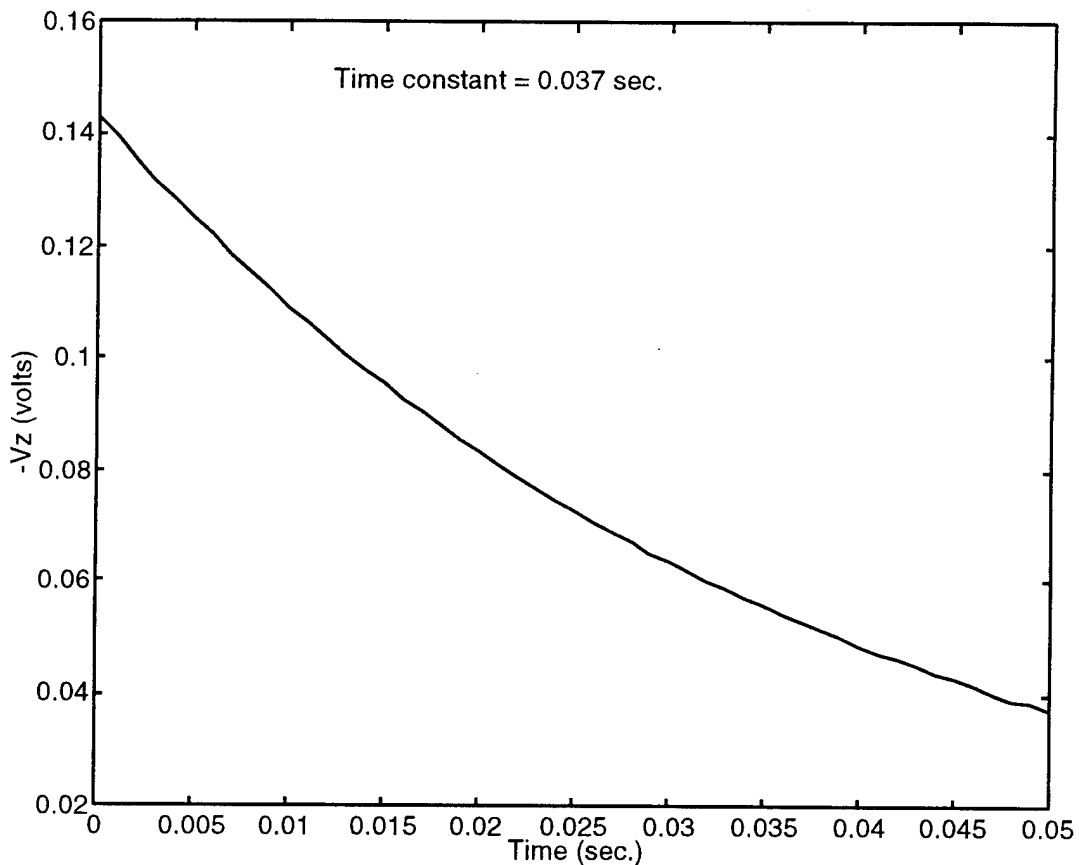
Figure 9A: Modeled Late Time Response of Aluminum Ring
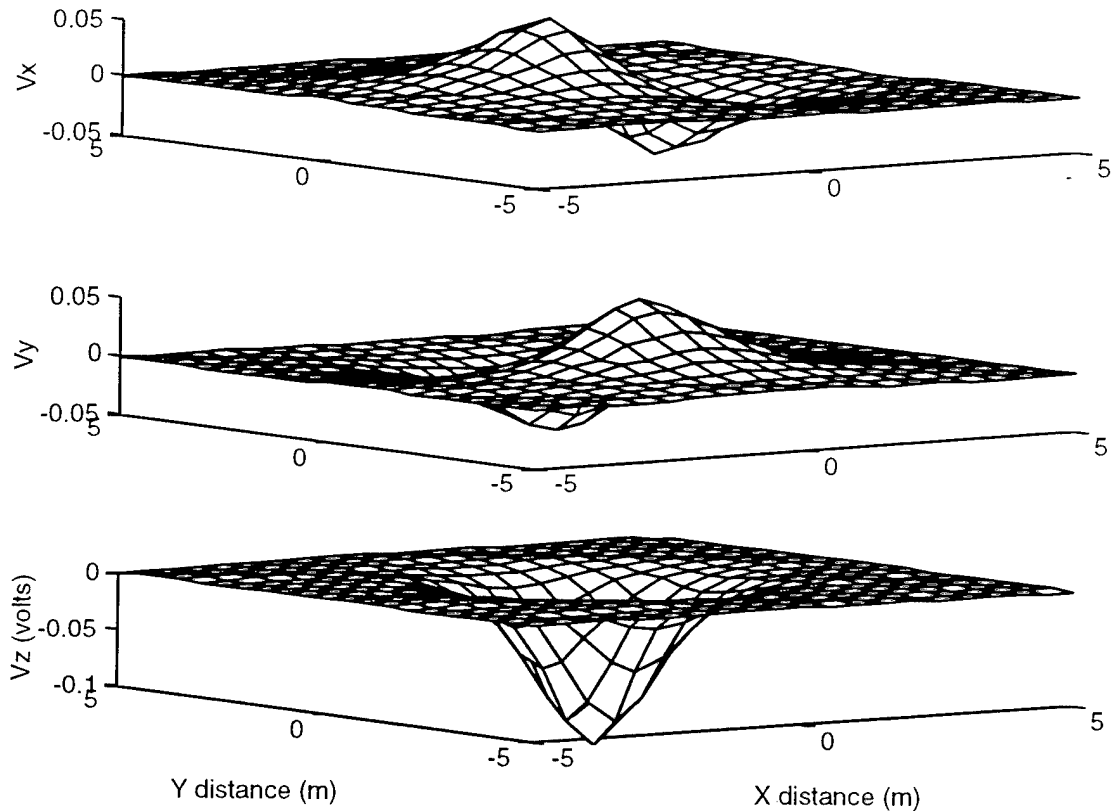
Figure 9B: Spatial Distribution of Amplitude of Late Time Response of Aluminum Ring

Figure 9A shows the modeled late time decay of the induced current in the aluminum ring as measured by the receiver located at the origin. Only the voltage due to the vertical secondary field component is shown since the horizontal secondary magnetic field is zero at the origin. The modeled time constant is 37 msec, computed using Eqns 3.7-3.9.

Figure 9B shows the modeled receiver voltage on a horizontal grid on the ground (z=0). Different spatial distributions are associated with different components of the receiver voltages. These spatial structures of the signal are related to various target parameters and will be utilized to obtain parameter estimates. Details of inversion of the measured data for target parameter estimation is given in Section 3.1.2.

Although a large horizontal grid for receiver voltages is shown in Figure 9B, measurements along only one or two lines are adequate for accurate target parameter estimation once the target is located. Figure 10 shows such a profile taken along the x axis.
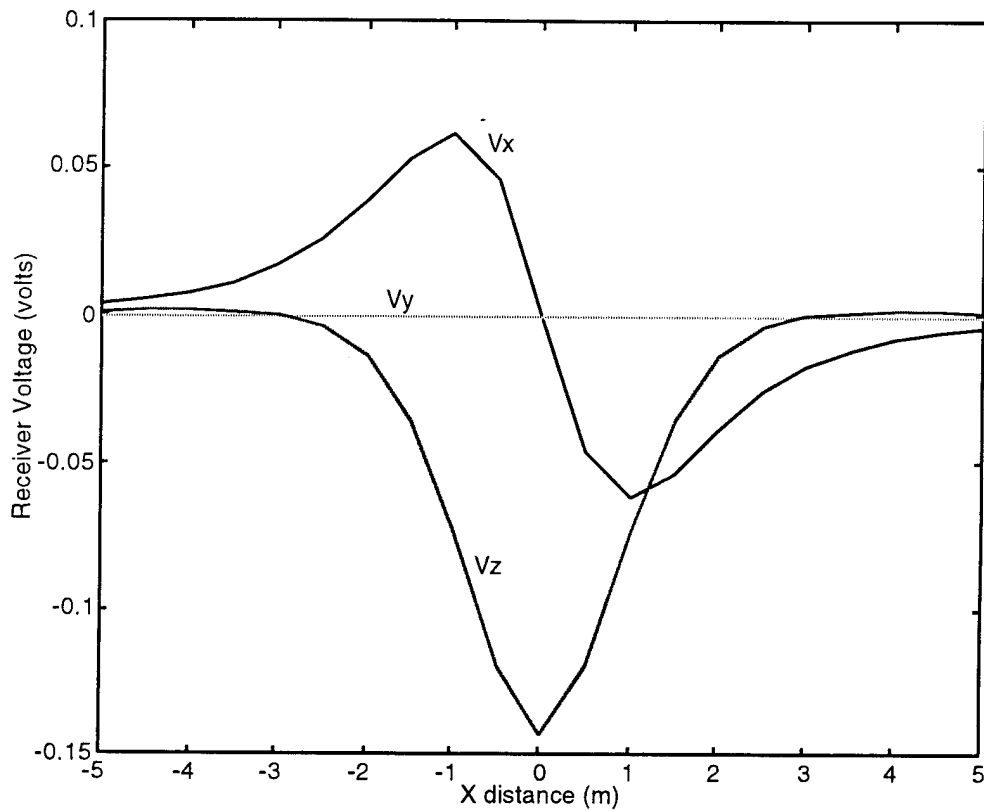
Figure 10: Profile Along X-Axis of Amplitude of Late Time Response of Aluminum Ring

3.1.1.4. Earth Response Model

Since the ground is a conductor of electricity, albeit orders of magnitude more resistant than a UXO, a pulsed current in the transmitter loop also induces currents in the ground. The earth response model is used to compute the ground's response to the pulsed emf and to assess its effect on target response detection.

The physics of the earth response to a pulsed emf is similar to that described earlier for a target conductor. A detailed account can be found in Kaufman and Keller[5]. In essence, currents are induced by the pulsed emf in the transmitter. At the beginning, the maximum current is found directly under the transmitter loop. Over time the induced currents move outward and downward, creating a current ring[6]. The earth's response to a magnetic dipole (Kaufman and Keller, 1983) is implemented. Since the secondary field is symmetric in the horizontal direction, the receiver voltages for the r and z components are modeled.

$$V_r \propto -\frac{\partial B_r(r,t)}{\partial t} = \frac{M\rho}{2\pi r^5} u^4 e^{-\frac{u^2}{4}} \left\{ (1+\frac{u^2}{2})I_0(\frac{u^2}{4}) - (2+\frac{u^2}{2}+\frac{8}{u^2})I_1(\frac{u^2}{4}) \right\}$$

18

$$V_z \propto -\frac{\partial B_z(r,t)}{\partial t} = \frac{-9M\rho}{2\pi r^5}\left\{\varphi(u)-\sqrt{\frac{2}{\pi}}e^{-\frac{u^2}{2}}u(1+\frac{u^3}{3}+\frac{u^4}{9})\right\}$$

(3. 11)

where $u = 2\pi r / \rho$

$$\tau = 2\pi(2\rho t / \mu_0)^{1/2}$$

$$\varphi(u) = \sqrt{\frac{2}{\pi}}\int_0^u e^{-\frac{t^2}{2}}dt$$

I_0, I_1 = Bessel function of zeroth and first order
M = magnetic dipole moment.
ρ = resistivity of the earth
μ_0 = permeability in free space

We are only interested in the late time stage of the earth's response. For late times ($\tau/r > 10$), the above equations can be reduced to

$$V_r = \frac{\mu_0 M}{64\pi}r(\frac{\mu_0}{\rho})^2 t^{-3}$$

(3. 12)

$$V_z = \frac{\mu_0 M}{20}(\frac{\mu_0}{\rho\pi})^{3/2}t^{-5/2}$$

An example of the earth response is shown in Figure 11. Receiver voltage of the earth response for a ground resistivity of 10 ohm-m measured at the location (1,0,0) is shown. Superimposed on it is the target response from the above example. Since the target's time constant is 37 msec, it does not change much over the time span shown. The earth response has a much smaller effective decay time, and drops below the target response after only 1 msec. This example illustrates that in general the earth response to the pulsed emf should not have significant impact on the detection of UXO using the PEMI technique.
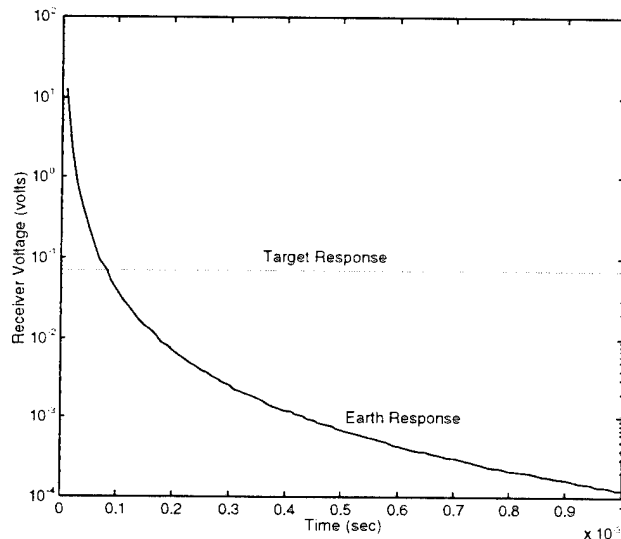
Figure 11: Earth and Target Late Time Response

3.1.2. PEMI Data Inversion

Section 3.1.1 describes PEMI forward modeling which calculates receiver voltages for a given set of transmitter, receiver and conductive ring target parameters. This section describes the PEMI data inversion problem and the estimation of parameters from observed receiver voltages. The formalism of the inversion algorithm used will be described here. Details of the inversion implementation, procedure, and analysis of PEMI data, is given in Section 3.1.3.

In general, the forward problem can be posed as:

$$\text{Field}(x,t) = F\{\text{Source}(x,t), \text{Medium}(x,t)\}.$$

The field observations are related to the source and medium by a forward function operator F, all of which are dependent on location x and time t. The inverse problem is to obtain either;

$$\text{Medium}(x,t) = G\{\text{Field}(x,t), \text{Source}(x,t)\},$$
or $\quad\quad\text{Source}(x,t) = H\{\text{Field}(x,t), \text{Medium}(x,t)\}.$

If the forward function F is known, an inverse solution can be obtained. It can be solved analytically if function F is invertible. However, this is not the case with PEMI and inversion can only be achieved by iteratively exercising the forward model with estimates of the source and medium parameters. Refinement of the estimates are done at each iteration until the best match between the field observations and model results is achieved. This approach is used in the PEMI data inversion.

3.1.2.1. Damped Least Squares Algorithm

In this study, PEMI data inversion uses the Marquardt-Levenberg damped least square algorithm. The formalism of this algorithm is described below.

Let: ND = number of observations or data values
NP = number of target parameters to be estimated
X = 1 x ND vector of coordinates at which observations are made and model data calculated
P = 1 x NP target parameter vector
O(X) = 1 x ND observed data vector at X
M(X,P) = 1 x ND vector of model data computed at X for parameters P.

One starts with an initial guess P^0. The difference between the model data $M(X,P^0)$ and observations O(X) is D = O - M. The objective is to adjust P by ΔP so as to minimize the mean squared error $<D^2>$. The desired change in parameter values ΔP can be estimated by linearizing the forward model and setting

$$D = \Delta P \cdot A \tag{3.13}$$

where ΔP is the perturbed changes in parameters P and A is the NP x ND Jacobian transformation matrix

$$
\begin{bmatrix}
\dfrac{\partial M(x_1, p_1)}{\partial p_1} & \dfrac{\partial M(x_2, p_1)}{\partial p_1} & \cdots & \dfrac{\partial M(x_{ND}, p_1)}{\partial p_1} \\[2ex]
\dfrac{\partial M(x_1, p_2)}{\partial p_2} & \dfrac{\partial M(x_2, p_2)}{\partial p_2} & \cdots & \cdot \\[2ex]
\cdot & \cdot & \cdots & \cdot \\[1ex]
\cdot & \cdot & \cdots & \cdot \\[1ex]
\dfrac{\partial M(x_1, p_{NP})}{\partial p_{NP}} & \cdot & \cdots & \dfrac{\partial M(x_{ND}, p_{NP})}{\partial p_{NP}}
\end{bmatrix}
\qquad (3.14)
$$

It can be shown that the least squares solution for Eqn. 3.13 is

$$\Delta P = DA^T(AA^T)^{-1}. \qquad (3.15)$$

If the forward model is nonlinear and the difference D is large, then ΔP calculated using Eqn. 3.15 may be far from the desired value and could move the least squares solution away from the desired result. Levenberg[7] and Marquardt[8] introduced a damping factor to the least square solution to restrict the size of ΔP, thus the term damped least squares. This is done by replacing AA^T with $(AA^T + \beta I)$ where

β = Marquardt parameter or damping factor, and
I = a NP x NP identity matrix.

The damped least squares solution is then

$$\Delta P = DA^T(AA^T + \beta I)^{-1} \qquad (3.16)$$

3.1.2.2. Damping Factor Determination

A choice for the damping factor β can be made based on the behavior of the mean least square error $<D^2>$ with respect to β. Eqn. 3.16 shows that as $\beta \to 0$, ΔP tends towards the least squared solution, and as $\beta \to \infty$, $\Delta P \to 0$. The expected behavior of $<D^2>$ with respect to β has a minimum corresponding to the optimal choice of β. If we choose the initial $\beta > \beta_{optimal}$, we can exploit the monotonicity of the curve to find the optimal β by iterative search. Optimal β is obtained when $<D_i^2>$ becomes smaller than $<D_{i-1}^2>$.

Adding β to each diagonal element of AA^T shifts all the eigenvalues of the problem by β. If this shift was of the order of the largest eigenvalue, we would expect that a further increase in β would not drastically affect the results. In the PEMI data inversion algorithm, we choose the initial β to be the maximum eigenvalue of AA^T to ensure the initial choice of β is larger than $\beta_{optimal}$.

3.1.3. PEMI Data Processing

The previous two sections described the mathematical models used to represent the physical processes associated with PEMI. The focus of this section is on the detailed implementation of these models within a PEMI processing system. To clarify the concepts of this section selected samples of field data are included as examples. This data should be considered as tutorial in nature. The detailed discussion of the field data and conclusions based upon it may be found in section 4.0.

PEMI data for a single target configuration consists of time series measurements of receiver voltages at locations along the x and/or y profiles, starting from the time of the primary current turn off. The data is processed in two separate data inversion steps to obtain estimates of the target parameters. The first step performs temporal data processing: it uses DLS to fit the measured time series to the model temporal response. This step addresses detection and classification of the target. The second processing step uses the results of the temporal data inversion to examine the spatial distribution of the target response. It addresses localization and depth estimates of the target. Both steps use the Damped Least Squares (DLS) algorithm described in Section 3.1.2 to fit the data with a model.

3.1.3.1. Temporal Response Data Inversion

The time constant τ of the late stage exponential decay of the target response is determined by the size, shape and conductivity of the target. Identification of the target is done by estimating τ from the time series of receiver voltages. Detection of the target is achieved when the signal-to-noise ratio is high enough to provide an accurate estimation of τ.

Figure 12 shows a flow diagram for the temporal response data inversion. At each location, three receiver voltage time series (corresponding to the three receiver axes) were obtained. Each time series may be smoothed by a moving-average pre-processing step to reduce background noise and clutter, if necessary. In the Mukilteo tests it was possible to measure the background "clutter" response in the absence of any targets of interest. It was useful to subtract the clutter response from target data to increase the time over which a good target response was visible. A time window within the time series is chosen to ensure that the data used in the DLS fit is in the late time stage of the response. This is usually done by visual inspection, that is, by looking for a straight line segment in the semi-logarithmic plot. The time series within the selected time window is fit to the PEMI late time response model $Ae^{-t/\tau}$ to obtain A and τ.
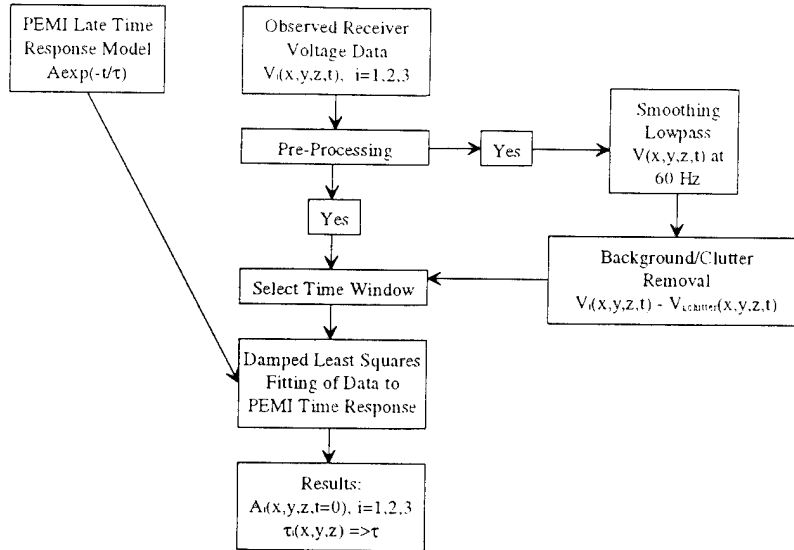
Figure 12: Flow Diagram of Temporal Inversion

An example of a measured receiver voltage time series is shown in Figure 13. The target is a thin aluminum ring (50 cm diameter, 3.5 cm wall thickness, and 5 cm long) located at a depth of 2 m above the origin (i.e. in the air). The measurements were obtained with the receiver located at the origin. Early time response consists of the sum of many exponentially decaying currents, and therefore does not appear as a straight line in this semi-logarithmic plot. Over time, only the current with the longest time constant dominates the response and the single exponential decay should show up as a straight line. This single exponential is clearly identifiable at times longer than 2 msec, even in the presence of background noise beyond 70 msec. A time window between 10 and 70 msec was chosen for the damped least squares fitting. The time constant obtained is 25 msec. It should be pointed out that the signal-to-noise ratio is high enough that even taking the time window to 100 msec does not change the result.
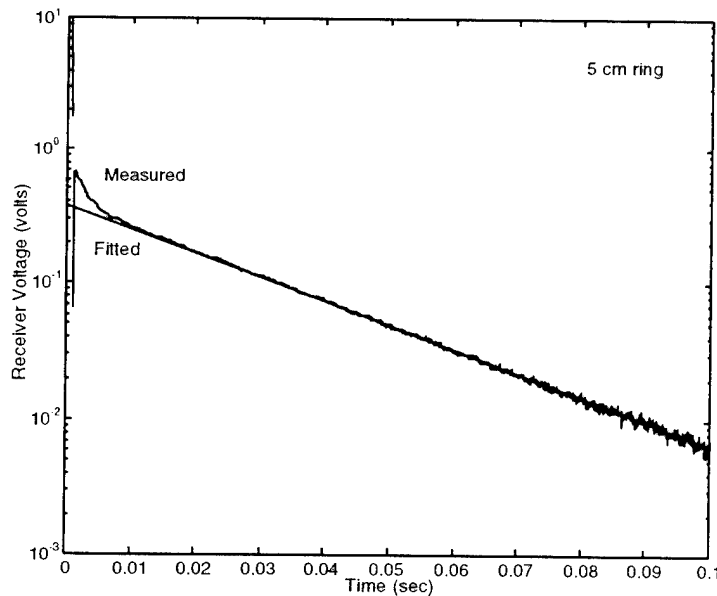
Figure 13: Received Voltage and Exponential Fit for 5 cm Aluminum Ring

However, PEMI target response may fall below the background noise level during the late time stage. This is illustrated in Figure 14 for an 80 mm UXO. In this case, pre-processing by smoothing is required to increase the signal-to-noise before the least squares fitting.

Close examination of the noise shows frequencies of 60 Hz and higher. Although a significant portion of this high frequency noise has been removed during the data acquisition, enough noise remains in the data to obscure the target response at late times. One of the steps in the pre-processing is simply to remove the high frequency noise by lowpass filtering the time series at 60 Hz.
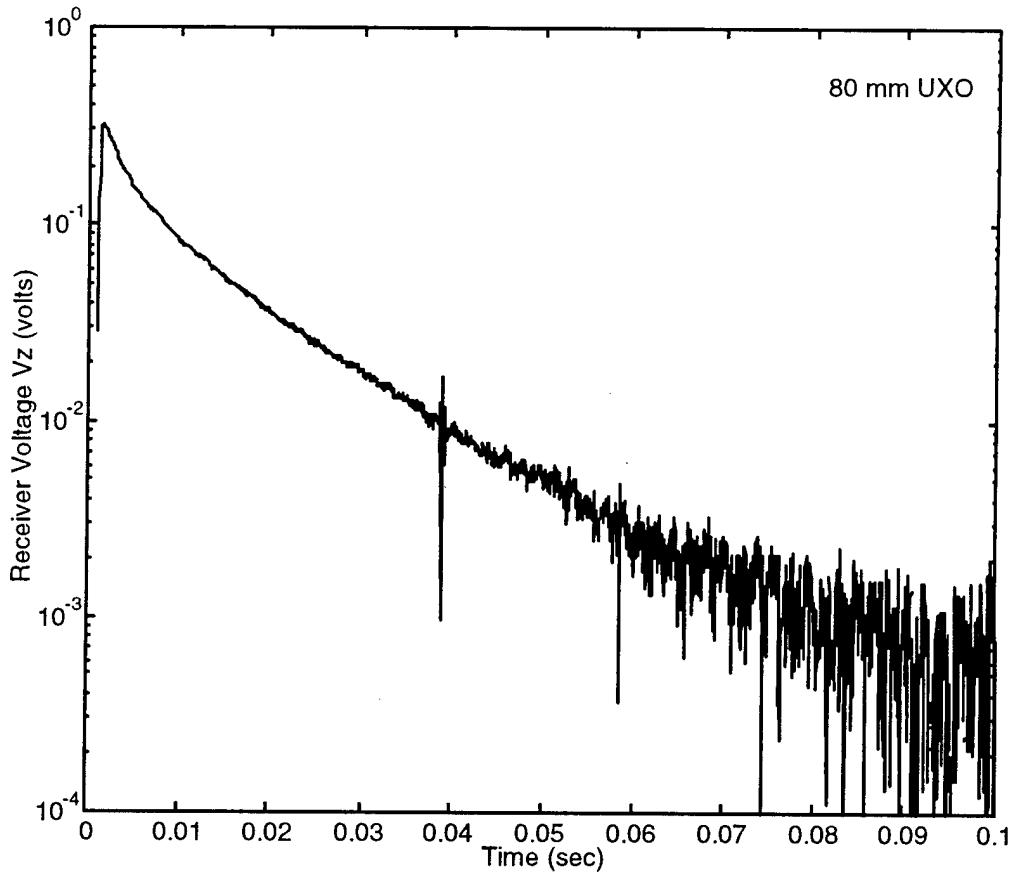
Figure 14: Received Voltage Response for 80 mm UXO Illustrating Noise Limited Operation

Figure 15 shows the lowpassed time series. In this example, even with the removal of the high frequency noise, it is still difficult to determine where the exponential decay is. With the time series still curving, one can argue that the 100 msec series is not long enough to obtain the longest time constant. It turns out that the flattening of the series at long times is due to the presence of background response. Plotted in Figure 15 is the collocated, smoothed receiver voltage obtained during the background survey, performed without any UXO target. It represents the background noise plus any clutter response to the pulsed emf. One can definitely see the similar slopes at late times.
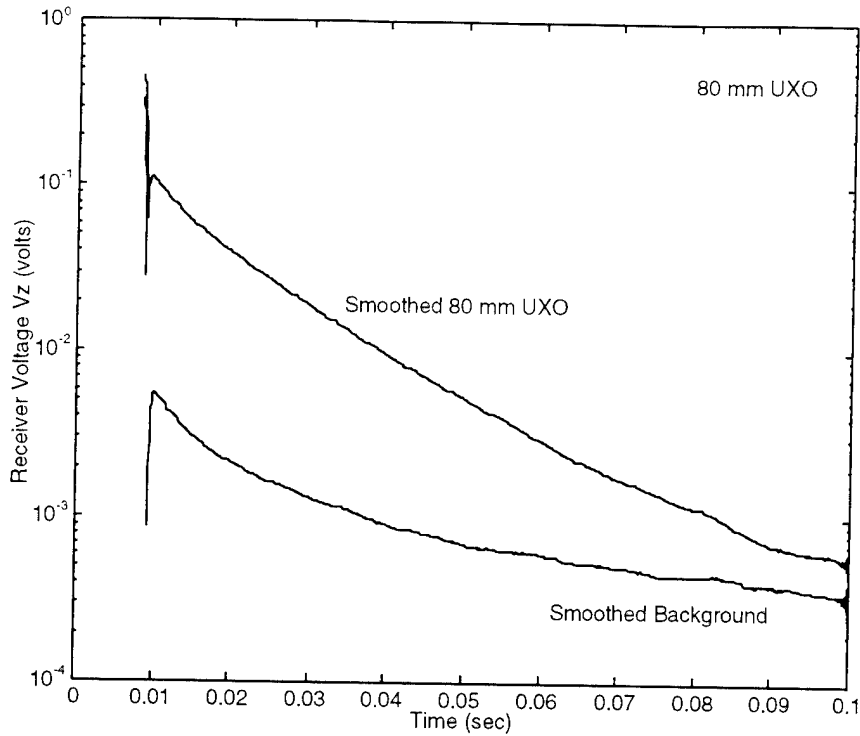
Figure 15: Low Pass Filter Response for 80 mm UXO

The true target response is revealed clearly when the background response is subtracted from the measured target response, as shown in Figure 16. One can now clearly identify the straight line portion of the response. A time window between 30 and 90 msec was chosen for curve fitting. The fitted time constant is 15 ms.
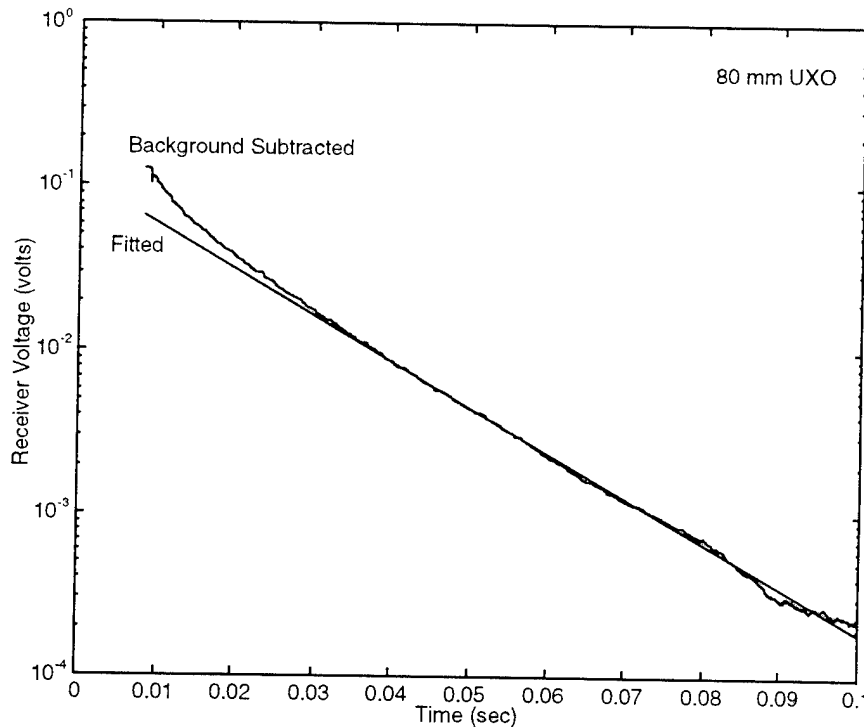
Figure 16: Response for 80 mm UXO with Background Removed

For a given target configuration, a set of $A_i(x,y,z,t=0)$ and $\tau_i(x,y,z)$ for $i=1,2,3$, were obtained from fitting the voltage time series. A_i is the estimated amplitude of the late time target response for each component at location (x,y,z) at time $t=0$. Figure 17 shows the x profile of the fitted A's for the 5 cm aluminum thin ring. It is this spatial distribution that will be utilized to obtain further target parameter estimation.
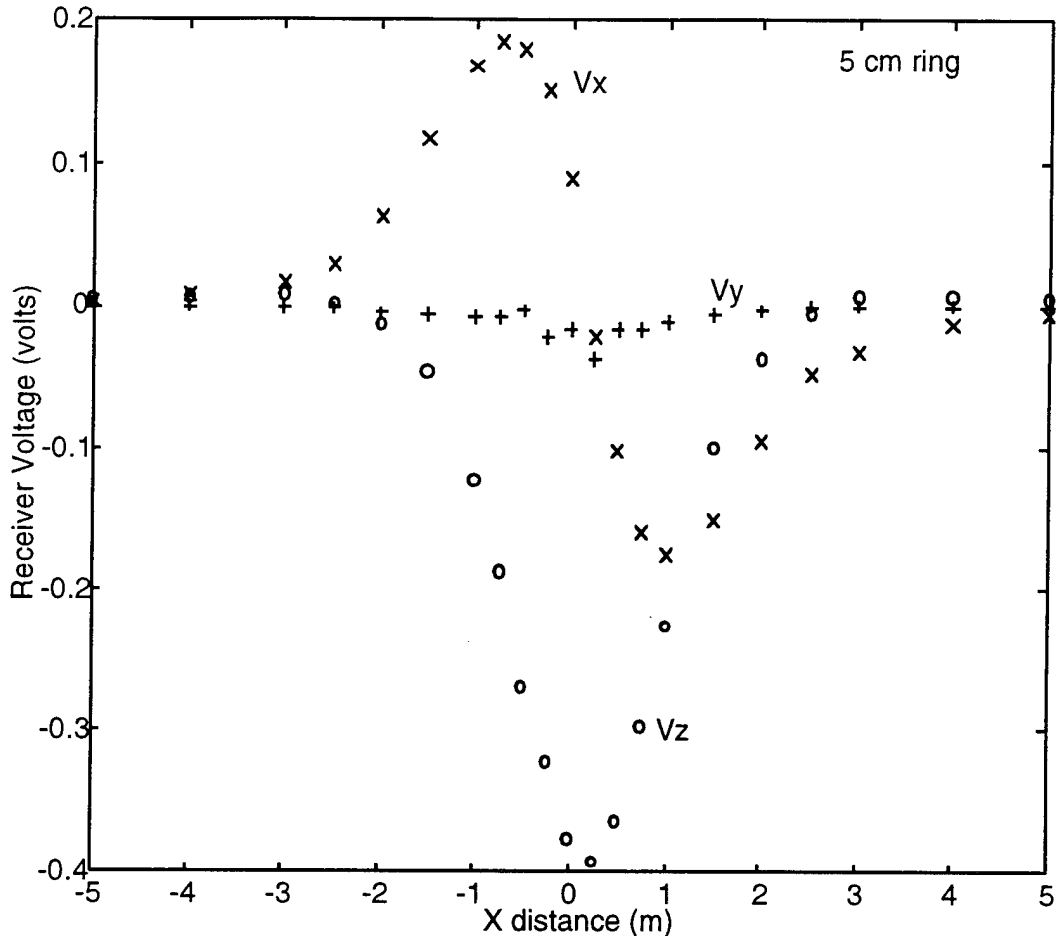
Figure 17: Amplitude of Exponential for 5 cm Aluminum Ring at Various Spatial Samples

A set of $\tau_i(x,y,z)$ is also obtained from the temporal data inversion. In theory, τ is determined by the size, shape and conductivity of the target, and should not vary with location or receiver axis. Variability of the fitted τ's is due to the variation of the signal-to-noise ratio with location and receiver component (i.e. Vx, Vy, or Vz). Only one single τ should be used in the spatial response inversion: the τ obtained from the highest signal-to-noise measurement is used in the Mukilteo tests.

3.1.3.2. Spatial Response Data Inversion

Estimation of the location and orientation of the target is accomplished using the spatial character of the secondary field data, as parameterized by the temporal data inversion. Figure 18 shows the flow diagram of this inversion procedure.
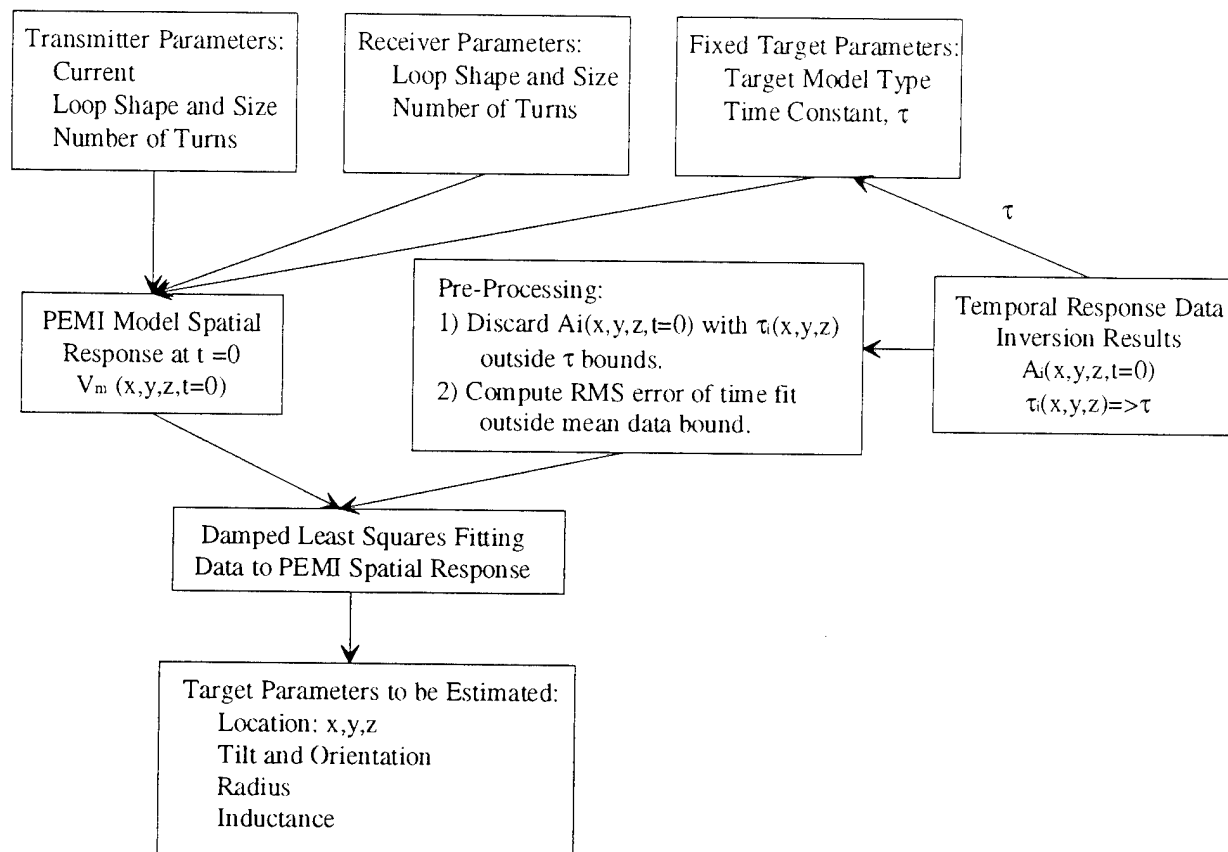
Figure 18: Flow Diagram of Spatial Inversion

Known transmitter parameters, receiver parameters, the time constant obtained from temporal data inversion, and an initial estimate for the target location are used in the PEMI forward models (described in Section 3.1.1.) to compute the expected receiver voltage at various locations, $V_i(x,y,z)$. They are compared with $A_i(x,y,z)$ obtained from the temporal inversion. The target parameters to be estimated are adjusted iteratively, using the damped least squares algorithm described in Section 3.1.2, until a best fit is obtained.

Pre-processing of the temporal data inversion results is needed before being used for the spatial inversion. Only a single τ should be used - chosen to be the one obtained from time series data with the highest signal-to-noise ratio. The fitted receiver voltages, $A_i(x,y,z)$, were screened for unrealistic values: those associated with unrealistic fitted τ and low signal-to-noise ratio were not used in the spatial data inversion.

Figure 19 shows an example of the spatial data inversion. The target is a 5 cm aluminum ring. The symbols represent the observed receiver voltages $A_i(x,y,z)$. Our experience suggests that convergence of the least squares fitting usually occurs after several iterations if initial estimates of target parameters are within a factor of 2 of the true values. Lines in the figure represent the modeled voltages using estimated target parameters from the fitting. In this case, the model results compared favorably with the data: rms deviation between the model and data is 1%.
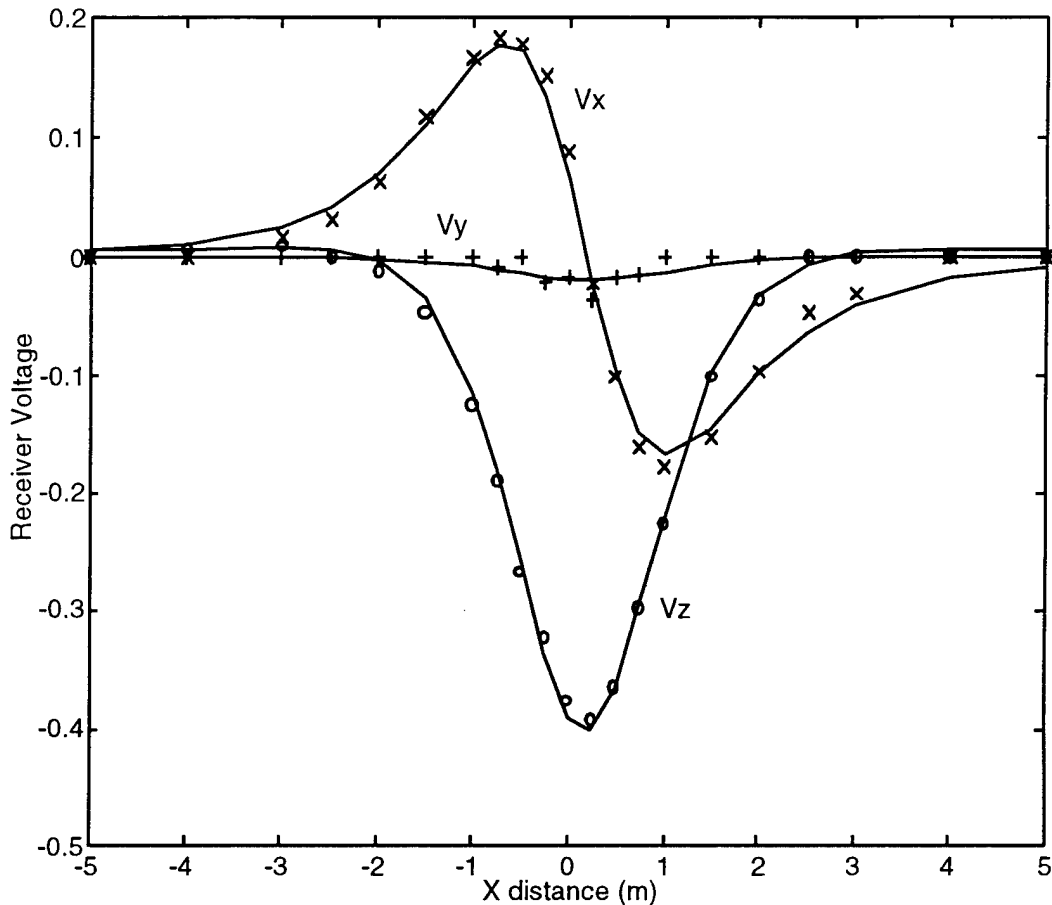
Figure 19: Spatial Inversion Results for 5 cm Ring

3.1.3.3.Background Magnetic Noise Cancellation

The level of background magnetic noise varies considerably with both location and time. Depending on its source the noise falls into one of two broad categories. Firstly, is naturally occurring magnetic noise which is primarily produced by excitation of the earth-ionospheric cavity by lightning strikes. It is estimated that there are on the order of 200 lightning storms going on simultaneously throughout the world. When the storms are close to the sensor, in geographic terms, the noise will be highly impulsive. For distant storms the frequency spectrum of the lightning strike is filtered by the lossy earth-ionosphere cavity, and resulting noise will be more gaussian. The second category is manmade magnetic noise which covers a wide range of generation mechanisms, each of which has a unique spectrum and power

level. A complete study of these sources is far beyond the scope of this study. However, one obvious source of manmade noise which should be mentioned is the grid of power lines and resulting ground currents flowing between all industrial and population centers. This noise is primarily 50 Hz or 60 Hz and all the associated harmonics.

Magnetic noise data collected from four different sources is shown in figure 20 which plots the magnetic noise amplitude spectra across the 1 to 1000 Hz band. This is the range of frequencies over which UXO target responses are expected. The ADS and Filloux data were taken underwater. For the most part magnetic noise enters the ocean through the surface, and because of the skin effect the level of noise decreases with depth. This effect is also frequency dependent because of the increase of attenuation with frequency in sea water. For these reasons, these two data sets should be considered best case examples (i.e. lowest noise power). The APL John Hopkins data was collected in air at the ocean surface. While this data does not have the filtering effects of water, it was collected a long distance from human population centers. The fourth set of data was collected by APL UW and it is believed to have been in the presence of a near-by lightning storm. This conclusion is based on the highly impulsive noise data present in the record, which produces the upward slope with respect to frequency. The critical conclusion to draw from these data sources is that there is a large degree of variability in magnetic noise levels (i.e. the noise amplitude spectrum varies nearly two orders of magnitude at 100 Hz). This indicates that while background noise may be insignificant in one location it may be a dominant corruption mechanism in another. A robust UXO sensor must operate effectively in both locations

In many cases, especially with natural sources, the magnetic noise measured at one point is nearly identical to that measured many meters away. This behavior reflects the high degree of spatial coherence which can be capitalized upon for noise cancellation. This technique usually involves gathering noise data at a point removed from the search sites (10's of meters) simultaneously with gathering the search data. Based on the degree of coherence, a significant amount of the magnetic noise in the search data may be canceled by subtracting a portion of the reference sensor. Proper use of optimal signal processing techniques will ensure that the cancellation only removes that segment of the noise which is coherent, and in situations where the coherence is low it will not corrupt the data.
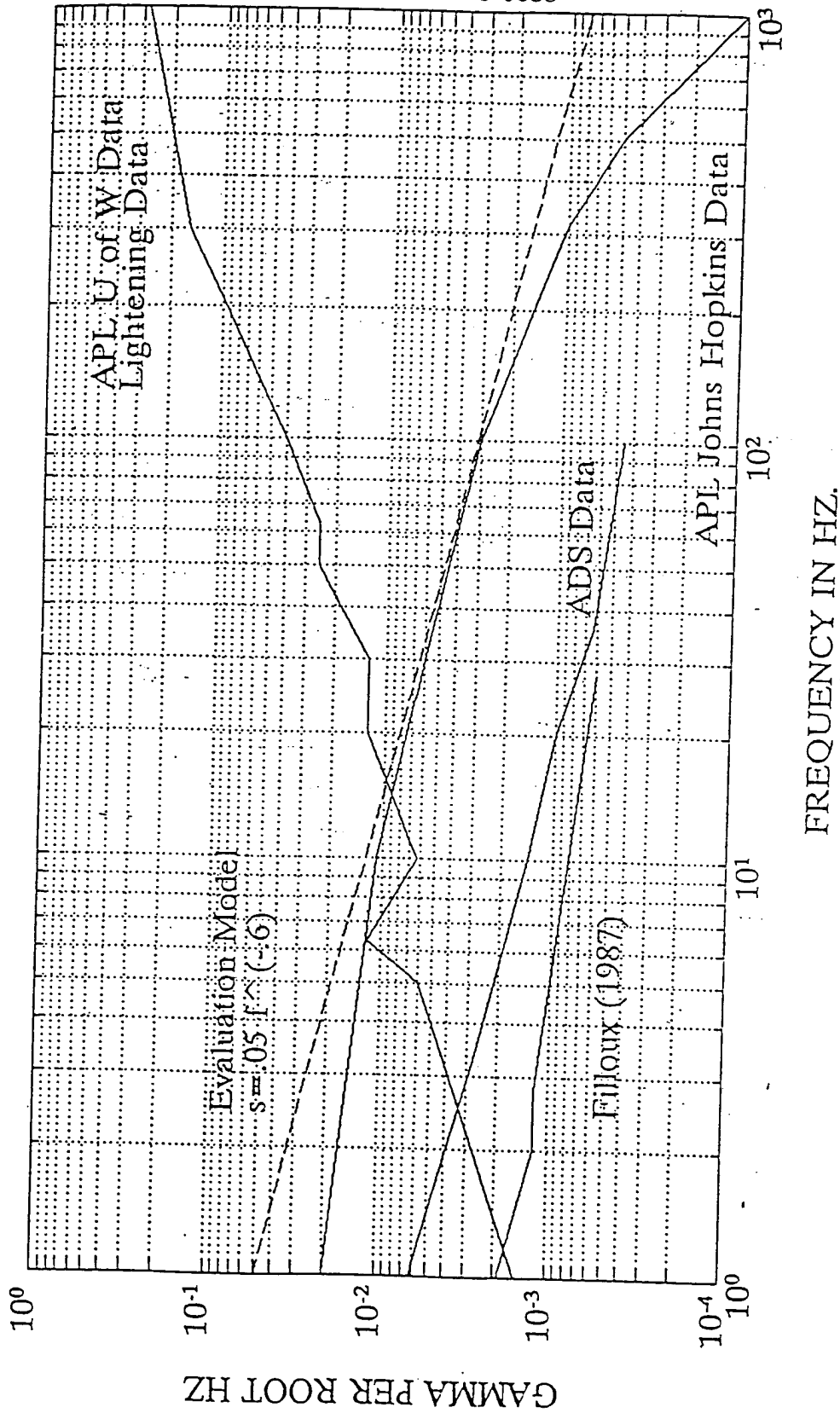
Figure 20: Magnetic Noise Amplitude Spectra for Various Sources

The noise cancellation approach adopted in this study is shown in figure 21, and a detailed derivation may be found in Appendix B. A brief summary is provided here for reference.
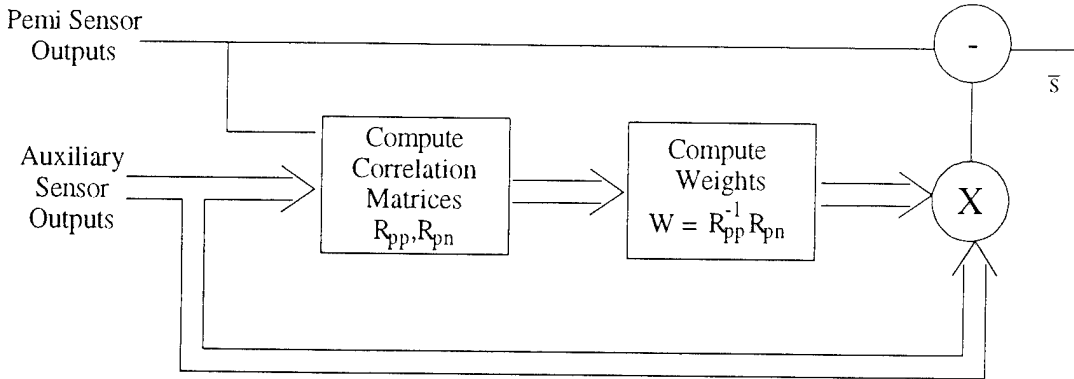
Figure 21: Noise Canceler Block Diagram

The weighting vector W is computed such that when it is multiplied by the auxiliary sensors(s) and subtracted from the PEMI output the error in the estimate is minimized. The noise cancellation equation is summarized below.

$$\bar{s} = r + W^t p$$

$\bar{s} = Noise\ Canceled\ PEMI\ Output$

$r = PEMI\ Sensor\ Measurment$ \hfill (3. 17)

$W = Weighting\ Vector$

$p = Auxiliary\ Sensor(s)\ Output$

Assuming the noise is independent from the signal and is white gaussian, the weighting vector is the product of the inverse of the auxiliary sensor autocorrelation matrix and the PEMI and auxiliary sensor crosscorrelation matrix.

$$W = - R_{pp}^{-1} R_{pn}$$

$R_{pp} = Auxiliary\ Sensor\ Autocorrelation\ Matrix$ \hfill (3. 18)

$R_{pn} = PEMI\ and\ Auxiliary\ Sensor\ Crosscorrelation\ Matrix$

For the case where a single auxiliary sensor is employed, a simplified expression may be written for the degree of expected noise cancellation.

$$\Delta = -10\log_{10}\left[1 - \rho_{pn}^2\right]$$

\hfill (3. 19)

$\rho_{pn} = Correlation\ Coefficient\ of\ PEMI\ and\ Auxiliary\ Sensor$

The noise reduction (Δ) as a function of the correlation coefficient is shown in Table 1.

Table 1: Expected Single Auxiliary Sensor Noise Cancellation

Noise Reduction (dB)	Correlation Coefficient
10	0.95
20	0.995
30	0.9995
40	0.99995
50	0.999995

From this table it is clear that significant noise cancellation (i.e. 20 - 50 dB) requires an extremely high level of spatial coherence. While this level of coherence has been achieved in underwater magnetic detection systems (APL Johns-Hopkins routinely achieves 40 dB noise cancellation), it may be more difficult in UXO applications. This is primarily due to the inclusion of man made magnetic noise which may not exhibit the high degree of coherence required for cancellation. This will be especially true for sites near population centers.

3.2. Proof of Concept Hardware

The PEMI hardware is composed of three principal parts: the PEMI transmitter, the receiver, and the data acquisition computer system. A block diagram of the PEMI hardware is shown in Figure 22. The data processing is done on a separate Macintosh computer, using programs written primarily in MATLAB.
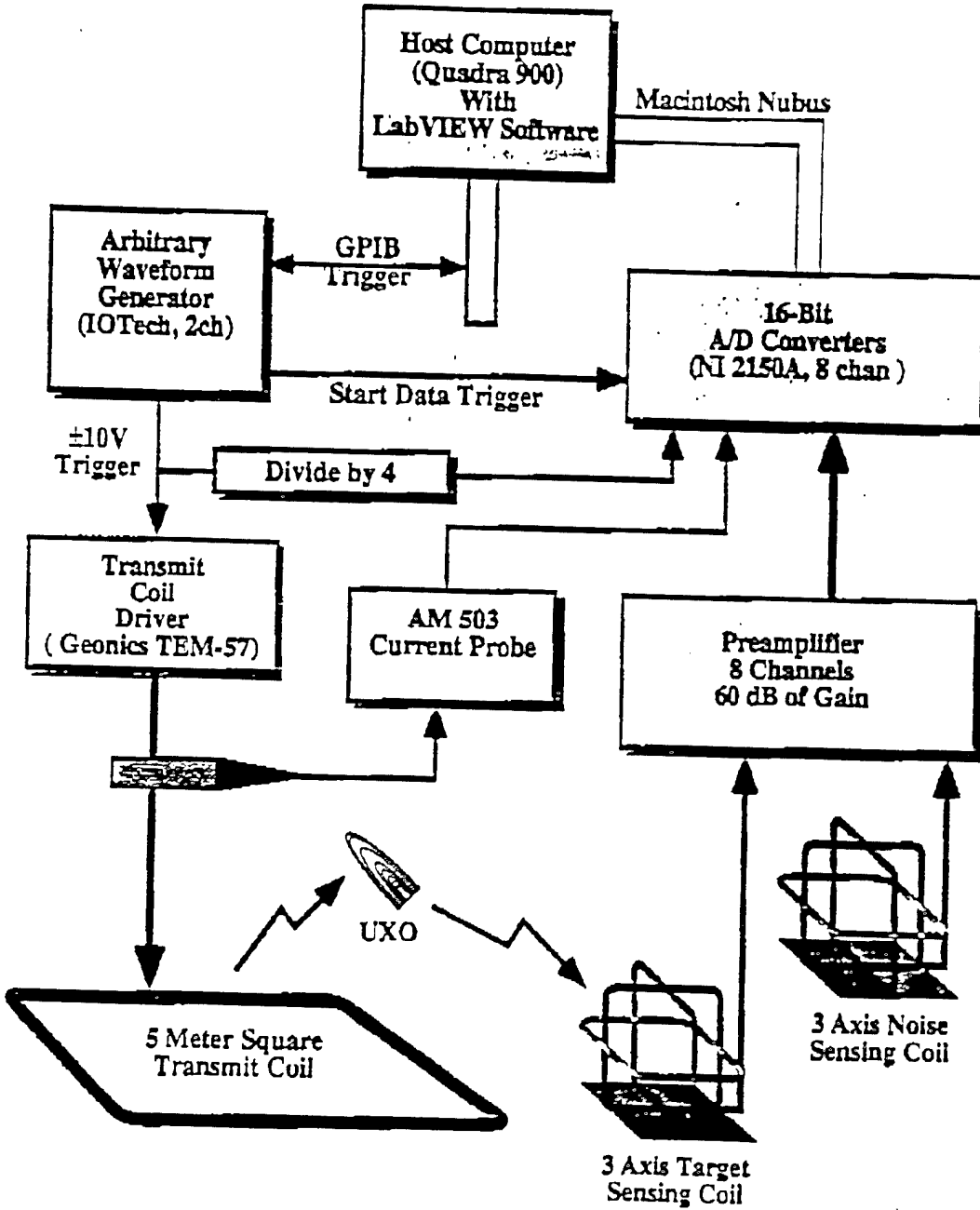
Figure 22: PEMI Proof of Concept Hardware Block Diagram

3.2.1. Data Acquisition System (DAS)

The heart of the DAS is a Mac Quadra 900 computer with National Instruments NB-A2150 analog to digital converter cards, and a GPIB interface card which allows remote control of the receiver amplifiers and the transmitter trigger waveform generator. The system is controlled by a program written in LabVIEW, a graphical instrument control language available from National Instruments. This program controls the entire data acquisition process, including sending out the transmitter triggers, digitizing the amplified receiver voltages, displaying the data upon acquisition, and finally storing the data to disk. A software block diagram is shown in Figure 23.

For the NAVEODTECHDIV demonstration a portable generator is required to provide AC power to the two computers, the transmitter and the various other components of the data acquisition system. A 1 kW portable generator was acquired in Seattle and shipped to the test site with the rest of the PEMI instrumentation. A long power cord (700 ft) was used to help reduce the electromagnetic noise from the unit.

An oscilloscope, a function generator, a power supply, and a frequency counter are included in the list of ancillary laboratory equipment needed for verifying that the system is functioning properly, or to repair it in the event of a failure.

3.2.2. Transmitter

The TEM-57 is a commercially available transmitter, designed for exploration geophysics application in mineral prospecting and hydrology. The transmitter establishes a DC current on the order of 20 Amps in a large loop of wire laying on the ground and then sharply turns off this current to create an electromagnetic pulse. The transmitter is controllable by an external trigger waveform as done in this PEMI system, or by an internal crystal clock. For safety, only 20 volts are supplied to the coil terminals, requiring a low impedance wire loop.

The coil must be designed to have about 1 ohm resistance. In this case, a 5 meter square loop is used, comprised of 14 turns of number 8 copper wire. Standard insulated household wire is well suited to this application and poses no risk to field operators because of the low voltages used.

The IOTech is a programmable waveform generator, used to trigger the transmitter at precise time intervals. Flexible programming of these timing waveforms allows cancellation of specific noise frequencies such as power line noise. The IOTech is controlled by the PEMI LabVIEW program and programmed over the GPIB bus.

Enter Test
Setup Data
&
Target Data

Do for N LOOP

Setup 16-Bit
A/D Converters

Trigger Arbitrary
Waveform
Generator
Over GPIB

Hardware Trigger
A/D Converters
From DAC488

Collect and Average
Data
8 Channels

Find± Pulse Pairs
Process &Exponential
Fit Data

Write Header File

Plot target
data & Fit Data

Write Data File

Plot Drive Current
And X:Y ratio

Write Raw Data
File
for All Channels
If Requested

Plot Raw Data
for All Channels
If Requested
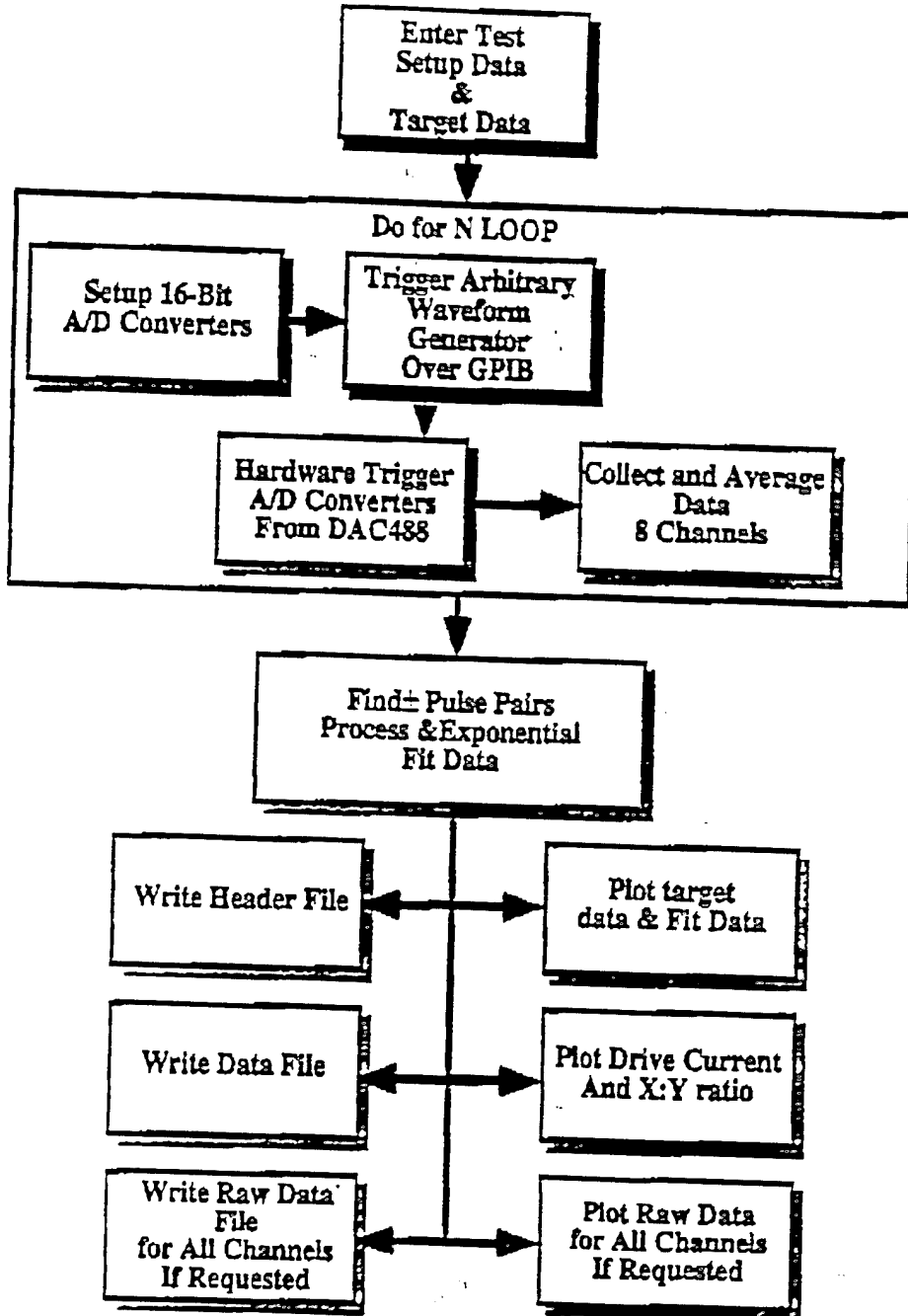
Figure 23: PEMI Data Acquisition Software Block Diagram

3.2.3. Receiver

The original plan was to use receiver coils manufactured by Geonics, but these proved (in the Mukilteo tests) not to be practical for this application. In the Geonics coils each horizontal component sensor is composed of two coils separated by about 60 cm. The signals from the two coils are combined electronically in a preamplification circuit and then sent down the connecting cable. The sensor was designed to measure magnetic fields which vary slowly over the dimensions of the sensor (geophysical prospecting and mapping), but the UXO application requires measuring fields of very small nearby objects. These fields vary significantly over the sensor's dimension and modeling the sensor's response would require precise knowledge of the coil geometries and electronic circuitry. Consequently, two 3-axis sensors using 200 turns of 24 gauge wire wrapped around a square frame 50 cm on a side were built. Three perpendicular concentric coils and a simple terminating circuit make up each sensor. The sensor is mounted on a platform with a bubble level and adjustable legs to make leveling quick and easy. A photograph of both receiver coil assemblies is shown in figure 24.
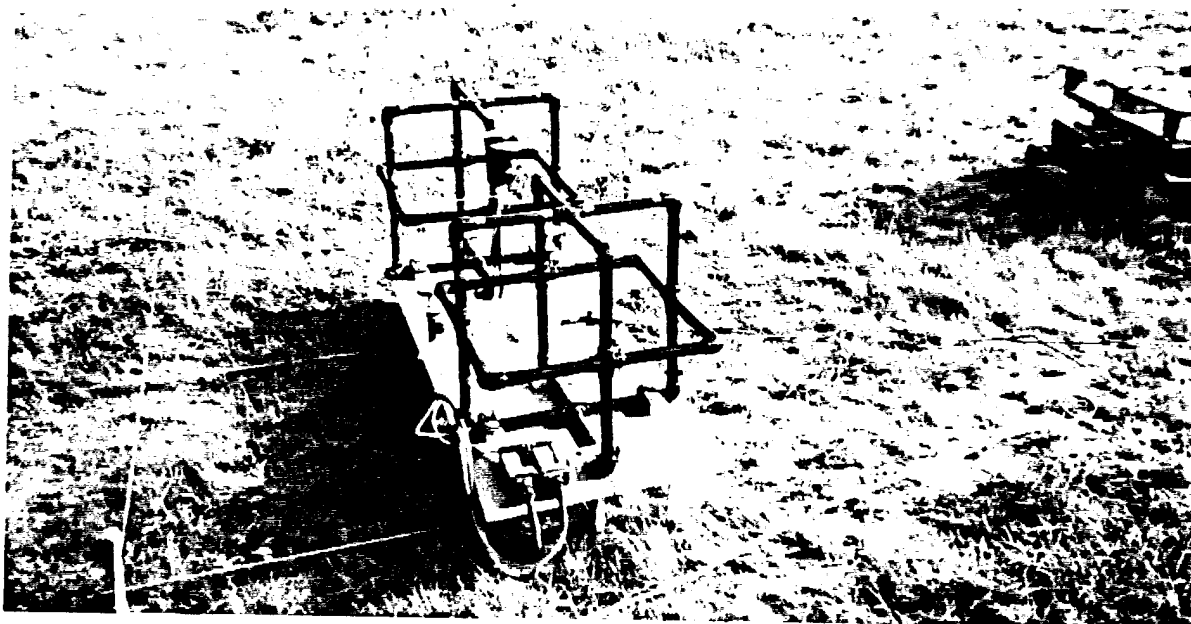
Figure 24: Photograph of PEMI Receiver Assembly

The Precision Filters filter/amplifier is a multi-channel programmable signal conditioning instrument. It is also controlled by the PEMI LabVIEW program, and programmed over the GPIB bus. This unit was not available during the Mukilteo tests, and a simple 8 channel preamplifier was built specifically for those tests. The Precision Filters unit was used for all the NAVEODTECHDIV tests.

3.3. Test Approach

The approach taken for the PEMI test phase was to conduct two series of tests at different locations. The objectives and approaches associated with these tests are summarized in the remainder of Section 3.3. A detailed description of the results and test configurations are provided in Section 4.0.

3.3.1. Mukilteo Test Approach

The first phase of testing was conducted at Alliant Techsystems Facility in Mukilteo Wa. The objective of this phase was verification of operation of the proof-of-concept hardware, validation of the PEMI models, measurement of responses of various UXO, and calibration of the PEMI models for the UXO provided by NAVEODTECHDIV.

To allow for economic gathering of a large number of target cases, the tests were done with the targets in air rather than buried under the ground. This in no way impacts the validity of the results as will be shown in section 4.1.

The operation of proof-of-concept hardware and validation of the PEMI models were primarily done with simple target shapes of uniform material (i.e. Aluminum and Steel Rings). This allowed validation of the primary and secondary field models independent of the uncertainties introduced by the complex shape and construction of UXO. Once the operation of the hardware and form of the PEMI models were confirmed, a series of data sets were taken on actual UXO to determine their response characteristics. The UXO targets also demonstrate the capability of the simple ring loop model employed in PEMI to accurately mimic the response of a complex UXO target.

3.3.2. NAVEODTECHDIV Test Approach

The second phase of testing occurred at the NAVEODTECHDIV magnetometer test range, and was a blind demonstration of PEMI performance. Three grids, 10 X 10 meter square, were selected by NAVEODTECHDIV personnel for the PEMI demonstration. Each site was subject to the same basic approach. First, a magnetometer and coarse PEMI scan were conducted over each area. The results from the sensors were compared, and all possible items of interest were identified. A fine PEMI scan was then conducted over each anomaly for localization and identification. A more detailed description is provided in the EOD Test Plan contained in Appendix D.

3.3.2.1.Augmentation of PEMI with a Magnetometer

Magnetometer technology is quite mature, and is presently the sensor of choice for UXO detection. Modern magnetometers are quite sensitive, but suffer from a poor ability to discriminate between UXO and other metal objects. A classic example of this shortcoming is the search for UXO in a live-fire test range which has a significant amount of shrapnel (after all, 90% of the bombs exploded). In this scenario, the magnetometer will find a significant

amount of the UXO, but will also detect the majority of the shrapnel. Due to the magnetometers poor spatial resolution it is difficult to determine which is which without excavation.

In contrast, PEMI determines a time constant which is inherently related to the size of the object. This piece of information, when combined with the spatial profile of the response, can be effective in separating UXO from other metallic objects. The final result being a substantial decrease in the excavation required.

From this quick discussion it is apparent that PEMI and magnetometry can be complementary sensing technologies. As an informal demonstration of this capability a high sensitivity magnetometer (GEM GSM19 in gradiometer mode, See Appendix B for Spec Sheets) is included in the NAVEODTECHDIV Magnetometer Test Range portion of the field tests. A photograph of the magnetometer in operation is shown in Figure 25. For each test site the magnetometer is scanned over the entire area and combined with the PEMI coarse survey data to determine the location of anomalies. The identified objects of interest are subjected to a PEMI fine survey to determine object size(relative), orientation, and location.

Figure 25: Photograph of Magnetometer used in Conjunction with PEMI

4.   Results and Discussion

4.1.   *Mukilteo Test Site*

The objective of the Mukilteo Tests was verification of operation of the proof-of-concept hardware, validation of the PEMI models, measurement of responses of various UXO, and calibration of the PEMI models for the UXO provided by NAVEODTECHDIV.

4.1.1. Mukilteo Site Physical Description

The Mukilteo Test Site was located in a field behind the Alliant Techsystems facility. The test area was located approximately 300 feet from any buildings to reduce the effect of electromagnetic interference. A simplified schematic of the test area is shown in figure 26A, and a photograph is shown in figure 26B.
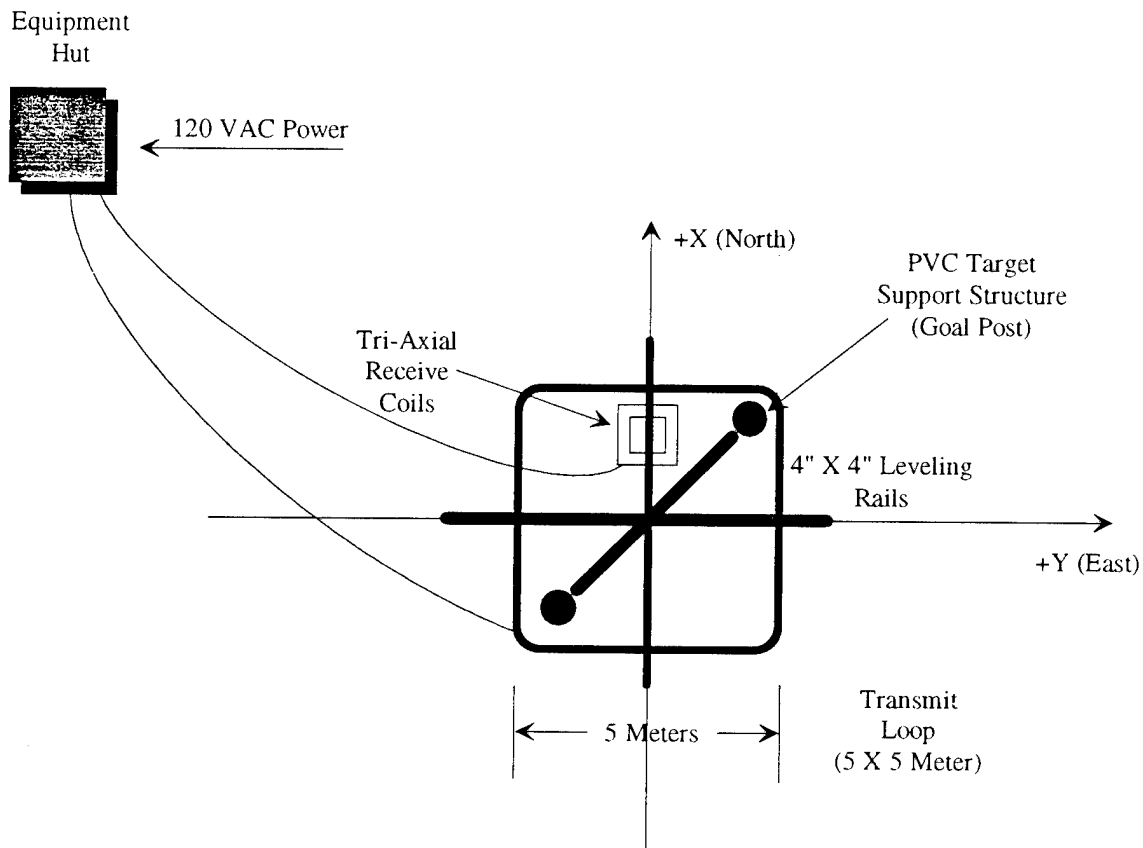
Figure 26A: Mukilteo Test Site Overview
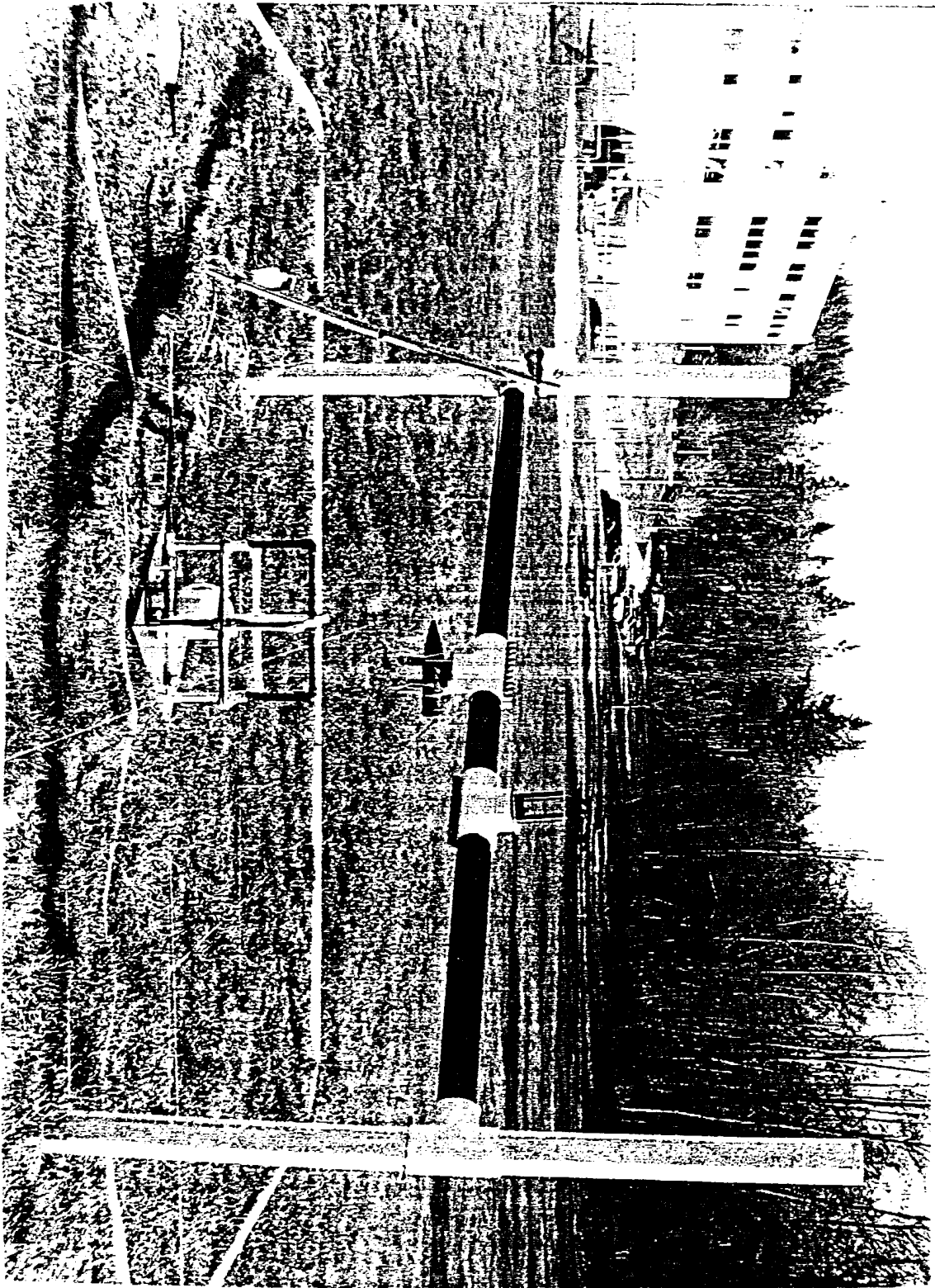
Figure 26B: Mukilteo Test Photograph

A non-conductive hut was constructed for the PEMI data acquisition electronics. The target support structure allowed for various targets to be held in different orientations over the transmit and receive coils. By adjusting the height of the support structure, various target depths were simulated. The receiver coils rested on the 4 inch X 4 inch leveling rails which ran along both the X and Y axes, and allowed the sensor to be mounted on a level surface at a consistent height. The rails were menstruated to 1/2 meter increments for accurate placement of the sensor.

4.1.2. Mukilteo Site Targets

Three types of targets were used at the Mukilteo Test Site: thin aluminum rings, hollow aluminum and steel cylinders, and UXOs (all UXOs used are ferromagnetic). Table 2 summarizes the physical dimensions of the targets. In this report, the measurement in front of a UXO (as in 80 mm UXO) refers to its diameter, and the measurement in front of a ring or a cylinder refers to its length.

Table 2: Summary of targets used in Mukilteo Tests

Targets	Length (cm)	Outer Diameter (cm)
2.5 cm aluminum ring	2.5	46.5
5 cm aluminum ring	5.0	49.9
100 cm aluminum cylinder	100	11.0
100 cm steel cylinder	100	11.0
80 mm UXO	31	8.0
122 mm UXO	53	12.2
155 mm UXO	66	15.5

The fabricated 2.5 and 5 cm aluminum rings are 3.5 cm thick, making them suitable for verification of the PEMI model based on a thin ring target. PEMI measurements for three UXOs: 80, 122 and 155 mm were made. A 133 mm UXO was also available at the Mukilteo Test Site. However, since it was so close in size to the 122 mm no data was collected for it.

4.1.3. Mukilteo Site Data Collected

PEMI data was taken with targets placed at various locations, and at different tilt and orientation angles. Table 3 summarizes the data collected. An x profile indicates data were taken along the x-axis as indicated in figure 26A. Both x and y profiles were taken when they were expected to be different due to the target configuration. Otherwise only one profile was taken.

Table 3: Summary of PEMI data collected in Mukilteo Test

Target	Location x (m)	Location y (m)	Location z (m)	Tilt (deg.)	Orientation (deg.)	Profiles taken
5 cm Al ring	0.2	-0.03	-2.0	0	0	x
	0	-0.05	-1.9	33	0	x,y
	0.9	0.9	-2.0	30	45	x, y
2.5 cm Al ring	-0.1	0.1	-1.4	1	0	x
2.5 & 5 cm Al rings	0.1	0.1	-1.4 (-2.0)	0	0	x
80 mm UXO	0.2	-0.1	-1.9	180	0	x
	0.3	-0.02	-1.9	132	0	x, y
122 mm UXO	0.1	-0.01	-1.3	180	0	x
	-0.04	-0.04	-1.5	135	0	x, y
155 mm UXO	0	-0.02	-1.5	0	0	x
	-0.02	-0.01	-2.0	114	0	x, y
	-0.01	-0.04	-1.4	136	0	x, y
100 cm Al cylinder	0.04	2.5	-1.6	90	90	y
	0	2.5	-1.0	90	90	y
100 cm Steel cylinder	0.03	2.5	-1.7	90	90	y
	0.04	2.4	-1.1	90	90	y
122 mm UXO	0.04	2.6	-1.7	90	90	y
	0.04	2.6	-1.0	90	90	y

In most cases, a single target was used in each profile measurement. In one single case both the 2.5 and 5 cm aluminum rings were used at the same time. They have the same horizontal (x,y) locations but separated in depth by 0.8 m. The purpose of this case was to obtain data to examine target response coupling.

For the 90° tilt cases, the long target (122 mm UXO, steel and aluminum cylinders) was put horizontally. PEMI data were collected with the target located at two different depths. The transmitter was moved such that one side of the loop was directly underneath the target to produce maximum magnetic flux through the target. The purpose was to collect PEMI data to examine possible excitation of different modes by the primary pulsed electromagnetic field and to study the representation of cylindrical targets by a thin ring target response model.

Ambient electromagnetic noise data were obtained using two receivers separated from 1 to 5 m. This data set was to be used for the noise cancellation and is discussed in section 4.1.9.

A survey of the PEMI background along the x and y axes was also done by sending a pulsed current through the transmitter loop in the absence of any known target. The data thus obtained contained clutter response (if any) to the pulsed emf. Clutter can then be subtracted from the PEMI target data collected at the same location.

4.1.4. Test Target Model Validation Results

Two thin aluminum rings were used to verify the PEMI models. PEMI response data for each ring was obtained and their time constants estimated from the observed data using the temporal data inversion procedure in Section 3.1.3. Their time constants were also computed analytically using equation. 3.7 - 3.9 for thin rings.

It is known that there is significant variability in the resistivity of commercially available aluminum. Two values of resistivity were used in the computation of the resistance R of the aluminum ring: the textbook value of 2.83×10^{-8} ohm-m, and a measured value of 8.49×10^{-8} ohm-m. The one measurement of Aluminum ring material has resistivity three times larger than the textbook value. Both resistivity values were used in the analytical time constant. Table 4 shows the results. The observed τ lies within the range computed analytically using known resistivity variability of the ring material.

Table 4 Comparison of Time Constants.

Target Ring	Observed τ	Analytical τ ($\rho = 2.83 \times 10^{-8}$ ohm-m)	Analytical τ ($\rho = 8.49 \times 10^{-8}$ ohm-m)
5 cm Al ring	25 msec	37 msec	12 msec
2.5 cm Al ring	9 msec	17 msec	6 msec

Target parameters obtained from data inversion for the 2.5 and 5 cm aluminum rings compare favorably with their true values, verifying the validity of the PEMI forward models and data inversion algorithm. The comparisons are summarized in Table 5. Due to the high signal-to-noise ratio in these cases, background clutter removal is not necessary in the cases shown. It should be pointed out that for small target tilt angles receiver voltage is insensitive to target orientation. Therefore the fitted orientation of 67^{0} for the 2.5 ring shown in Table 5 is not meaningful and does not imply poor estimation for that target parameter.

Table 5: Comparison between true and fitted thin ring target parameters

Target		5 cm Ring	5 cm Ring	5 cm Ring	2.5 cm Ring
x (m)	True	0.2	0	0.9	-0.1
	Fitted	0.2	0	0.9	-0.1
y (m)	True	-0.03	-0.05	0.9	0.1
	Fitted	-0.1	0	0.9	-0.1
z (m)	True	-2.0	-1.9	-2.0	-1.4
	Fitted	-2.2	-1.9	-2.0	-1.4
Tilt (deg.)	True	0	33	30	1
	Fitted	10	33	27	9
Orientation	True	0	0	45	0
(deg.)	Fitted	1	4	40	67
Radius (cm)	True	23	23	23	21
	Fitted	24	24	24	23

4.1.5. Test Target Response Coupling Results

When two nearly adjacent conductors are subjected to a pulsed emf, induced currents in one could induce additional currents in the other. Since electromagnetic coupling between the two targets is assumed to be negligible in the PEMI forward models, it is important to assess the validity of this assumption and how well two adjacent targets can be identified.

To examine these issues, PEMI data was taken with the 2.5 and 5 cm rings present at the same time. They were placed at the same x, y locations but separated in depth: the 2.5 cm ring closer to the plane of the receiver and transmitter by 0.8 m

Figure 27A shows the time series of the measured PEMI response of each target separately when only one is present. The late stage responses are clearly discernible from the straight lines in the semi-logarithmic plot. Due to its closer proximity to the transmitter, the 2.5 cm ring has a stronger PEMI response, but due to its short time constant, it quickly decays to below the signal level of the 5 cm ring response.

Also shown in figure 27A is the sum of the two PEMI responses. It would be the measured PEMI response when the two targets are present and assuming there is negligible electromagnetic coupling between the two targets. Figure 27B shows the actual measured PEMI data when the two targets are present. Except for the high frequency noise at late times, there is no visual difference between the two curves, indicating there is minimum target response coupling for the 0.8 m separation.
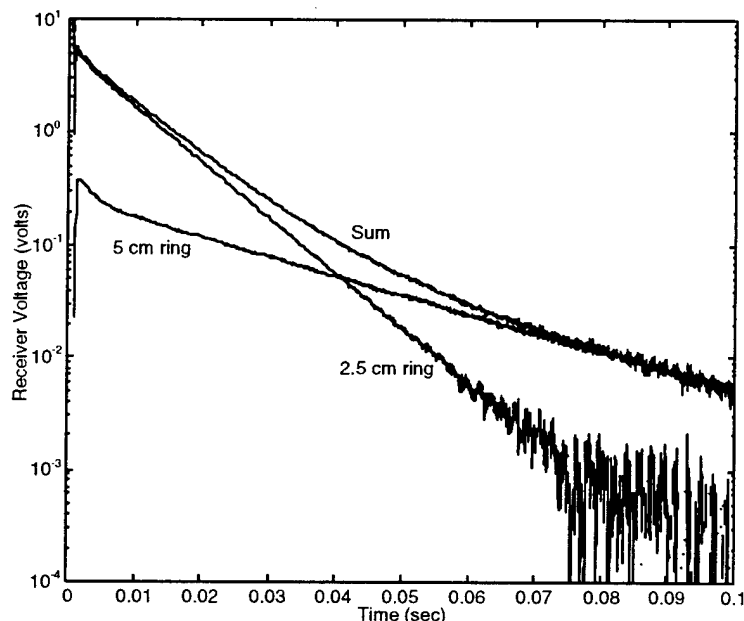
Figure 27A: Response of 5 & 2.5 cm Rings (Taken Separately), and the Arithmetic Sum of the Responses
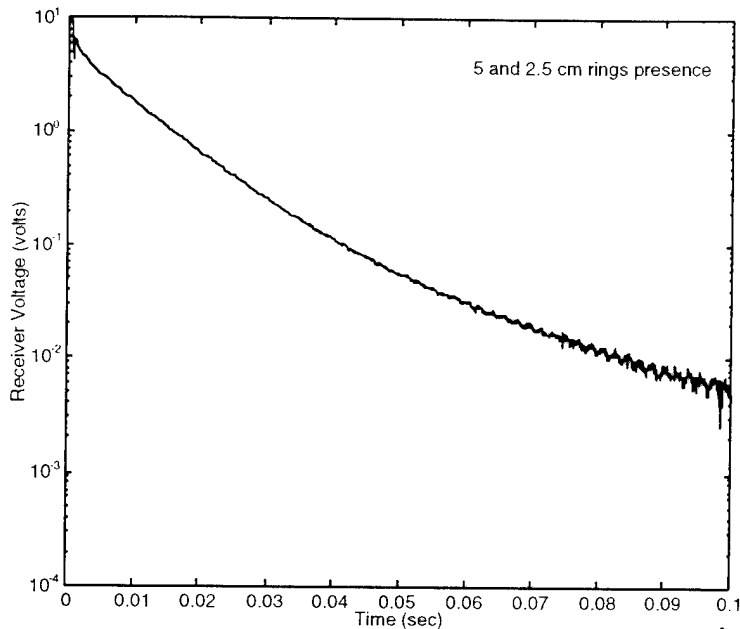
Figure 27B: Response of 5 & 2.5 cm Rings When in Close Proximity

Temporal data inversion was performed with the measured time series response when both targets were present. Separate time windows were chosen for the temporal data inversion: 1-2 msec and 7-10 msec for the shorter and longer time constants, respectively. Again the results were used for the spatial data inversion. Table 6 summarizes the target parameters estimated. Despite the difficulty of estimating time windows for the inversion, the results are only slightly worse than the cases when only a single target is present. This suggests that at separation of about 1 m or more target response coupling is minimum and separate identification and localization of targets is possible under such situations.

Table 6: Target parameters obtained from responses of co-existing targets

Target		5 cm Ring	2.5 cm Ring
x (m)	True	-0.04	-0.1
	Fitted	-0.1	-0.1
y (m)	True	0.04	0.1
	Fitted	0	-0.1
z (m)	True	-2.2	-1.4
	Fitted	-2.0	-1.4
Tilt (deg.)	True	1	1
	Fitted	-5	6
Orientation (deg.)	True	0	0
	Fitted	14	37
Radius (cm)	True	24	23
	Fitted	21	22

4.1.6. UXO Target Results

Three UXOs (80, 122 and 155 mm) were subjected to a pulsed emf and their response measured. In general, the signal-to-noise ratio for the UXOs are not as high as the 2.5 and 5 cm rings. Pre-processing of time series responses, smoothing, and removal of background noise/clutter were needed prior to temporal data inversion.

Figure 28 shows the time series of measured PEMI response for the 80, 122 and 155 mm UXOs after smoothing and background noise removal. The three series were all obtained with the target located at the center of the transmitter and the receiver at the origin. They represent the highest signal-to-noise ratio PEMI data for each of the UXO and are most useful to obtain time constant estimates. Response from 122 and 155 mm UXOs are very similar and much stronger than that of the 80 mm target.
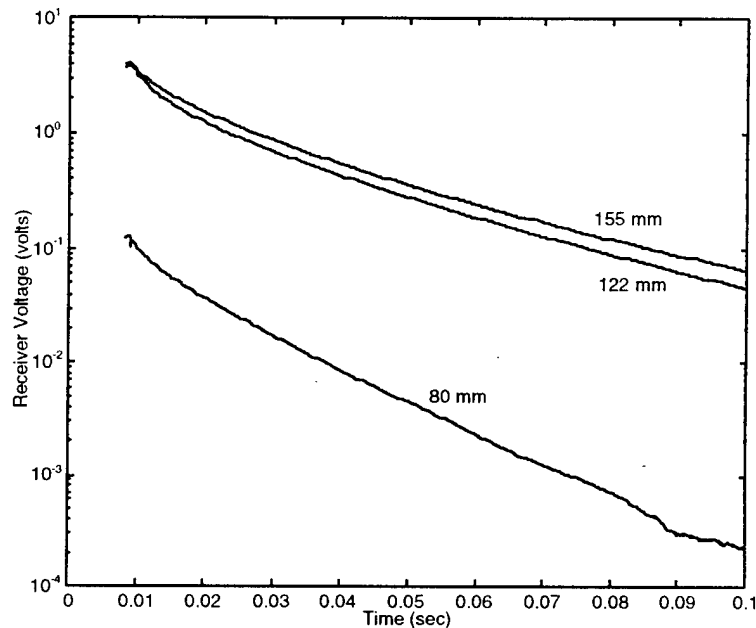
Figure 28: Temporal Response of 80, 122, and 155 mm UXO

Table 7 lists the time constants obtained by fitting these time series. These decay constants characterize each type of object; unfortunately, not all UXOs will have a distinctly different time constant. The 122 mm and the 155 mm shells have characteristic time constants that are very close in value. It is not clear from this result whether the two shells examined are typical and representative of their class, or if they are outliers. Nevertheless, distinguishing these two objects by time constant alone does not seem possible. On the other hand, there is a clear difference between the time constants of the 80 mm shell and the larger UXO.

Table 7 Time constants for UXOs

UXO	80 mm	122 mm	155 mm
Time Constants (msec)	15	29	30

The thin ring model assumes that the magnetic permeability of the ring and of the surrounding medium is that of free space. The inductance of the ring is only dependent on the radius of the ring. The UXO however are often composed of ferromagnetic material and a significant part of the inductance of the secondary current path is due to the large magnetic permeability in the object; the UXO can have a large time constant in spite of its small diameter. The thin ring model accounts for all these effects by adjusting the radius of the ring. The radius is also used in determining the amount of flux initially passing through the ring at time of turn off. Thus the fitted amplitudes of the response enter into the spatial inversion in a complicated way, and the resulting radius of the ring model that best fits a UXO response represents an *effective* radius that should be interpreted as a parametric representation of several attributes of the UXO that affect the amplitude and time constant of the response, including the shell thickness, its length, and the conductivity and permeability of its materials.

Figure 29 shows the spatial PEMI data (from temporal data inversion) and the fitted results for the 122 mm UXO. Because of the non-zero tilt in this case, the x and y profiles were expected to be different and therefore both were measured.

Figure 29: Fitted and Actual 122 mm UXO Spatial Response (X & Y Profiles)

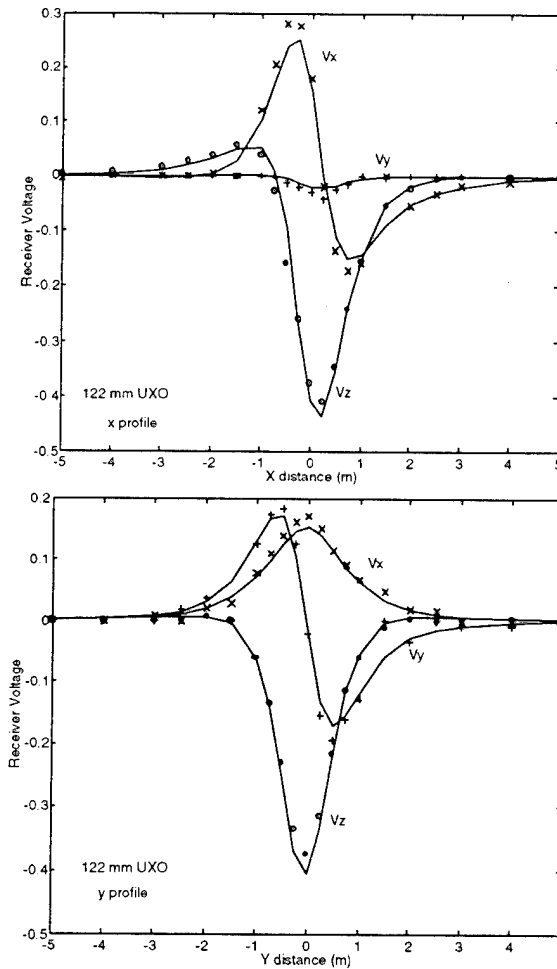Table 8 shows the true and fitted target parameters for all the UXO data measured. Most of the estimated target parameters compare favorably with their actual values. The worst cases

are the depth estimates for the 155 mm UXO; the largest error there is 0.4 m compared with other depth error estimates of less than 0.1 m. This large error could be due to the error of representing a 66 cm long cylinder by a thin ring in the target response model. It could also be due to errors in the time constant estimates.

Other target parameters, such as inductance and radius of thin ring, are also obtained from the spatial inversion. Since the UXO is represented by a thin ring model in the spatial data inversion, it is unclear how these values are related to the actual UXO which is cylindrical, and therefore are not listed in Table 8.

Table 8 Comparison between true and fitted UXO target parameters.

UXO		80 mm	80 mm	122 mm	122 mm	155 mm	155 mm	155 mm
x (m)	True	0.2	0.3	0.1	-0.04	0	-0.02	-0.01
	Fitted	0.2	0.1	0.1	-0.01	-0.04	0.02	0.1
y (m)	True	-0.1	-0.02	-0.01	-0.04	-0.02	-0.01	-0.04
	Fitted	-0.3	0	-0.1	-0.06	-0.05	-0.05	-0.05
z (m)	True	-1.9	-1.9	-1.3	-1.5	-1.5	-2.0	-1.4
	Fitted	-1.9	-1.7	-1.3	-1.6	-1.8	-2.4	-1.8
Tilt (deg.)	True	180	132	180	135	0	114	136
	Fitted	174	140	176	139	0	118	143
Orientation (deg.)	True	0	0	0	0	0	0	0
	Fitted	-38	10	73	-3	45	3	5

4.1.7. Horizontal UXO Target Response Results

PEMI data were collected with a long target (122 mm UXO, steel and aluminum cylinders) lying horizontally (90 deg tilt) at two different depths. The transmitter was moved such that one side of the loop was directly underneath the target to produce maximum magnetic flux through the targets. The purpose was to collect PEMI data to examine possible excitation of different modes by the primary field, and to study the representation of cylindrical targets by a thin ring target response model.

Figure 30 shows the results of the measured and fitted PEMI data for the horizontal 122 mm UXO at two different depths. As expected, the width of the response is narrower with the target closer to the receiver. The fitted time constants are 25 msec for both depths, suggesting that similar modes were excited in the two cases. PEMI data for the steel and aluminum cylinders reveal similar behavior.
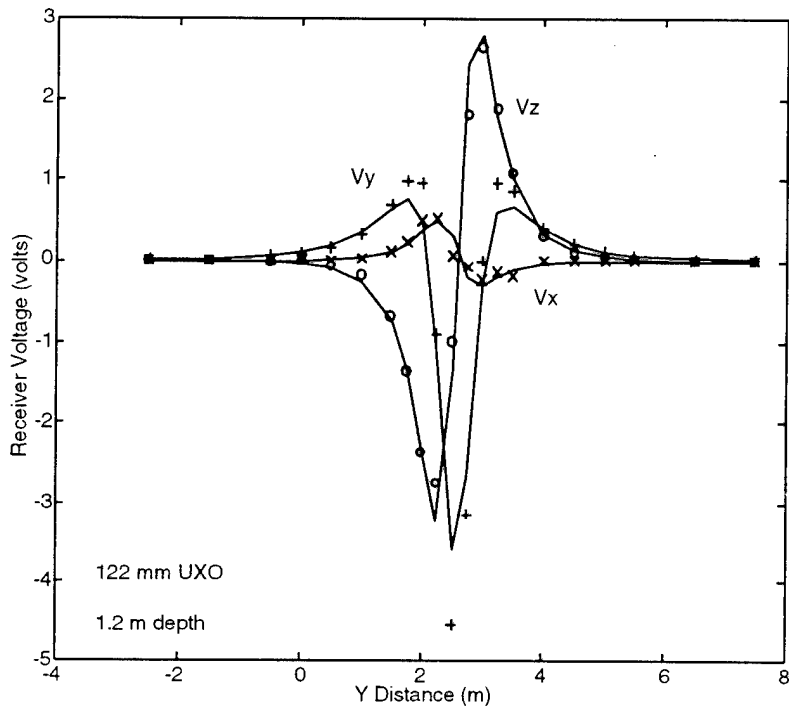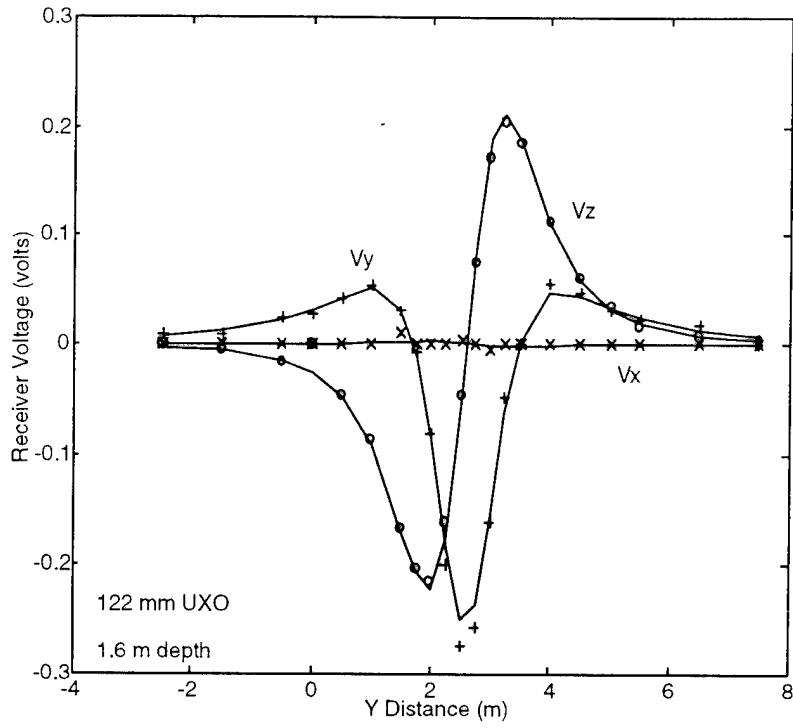
Figure 30: 120 mm UXO Spatial Response at Two Different Depths

Table 9 summarizes the target parameter estimates for the data collected. Fitted target parameters compare favorably with actual values, with the exception of the tilt angles for the 100 cm aluminum cylinder. It is not clear what caused the large discrepancies in this case.

Table 9: Comparison between true and fitted target parameters with horizontal targets.

Target		122 mm UXO	122 mm UXO	100 cm Aluminum	100 cm Aluminum	100 cm Steel	100 cm Steel
x (m)	True	0.04	0.04	0.04	0	0.03	0.04
	Fitted	0.01	0.1	0.07	0.1	0.05	0.1
y (m)	True	2.6	2.6	2.5	2.5	2.5	2.4
	Fitted	2.6	2.6	2.4	2.4	2.5	2.5
z (m)	True	-1.7	-1.0	-1.6	-1.0	-1.7	-1.1
	Fitted	-1.8	-1.2	-1.7	-1.2	-1.8	-1.3
Tilt (deg.)	True	90	90	90	90	90	90
	Fitted	89	88	45	61	89	87
Orientation (deg.)	True	90	90	90	90	90	90
	Fitted	90	92	87	90	91	92
Inductance (H)		7.5E-7	8.0E-7	7.4E-7	7.3E-7	7.4E-7	7.3E-7
Radius (m)		0.22	0.24	0.16	0.19	0.31	0.37
Time constant (msec)		25	25	7.5	7.4	21	21

4.1.8. Comparison of In-Air and In-Ground UXO Response

The conductivity contrast between typical soils and the metals used in UXOs is very large (4 to 8 orders of magnitude).   Consequently, the earth response (and also any coupling between the earth response and UXO response) is expected to be negligible (see section 3.1.1.4). Nevertheless, experimental confirmation of that result is presented here.

An 80 mm shell was buried inside two holes drilled into the ground at the Mukilteo test site. One hole was essentially vertical and the other was dipping at about 35 degrees from vertical. In each case, the sensor platform with both PEMI sensors on it (in the configuration used in the EOD magnetometer range tests) was profiled over the buried shell. The data was processed in the ways described in Section 3.1, and the final results of the inversion are presented in Table 10. The signal to noise level was very good, as was the quality of the model fit, as shown in figure 31. The host earth had no measurable effect on the results; the errors in mechanically estimating the actual position and orientation of the shell were of the same order as the difference between results of the PEMI inversion and the positions of the shell measured by mechanical means.
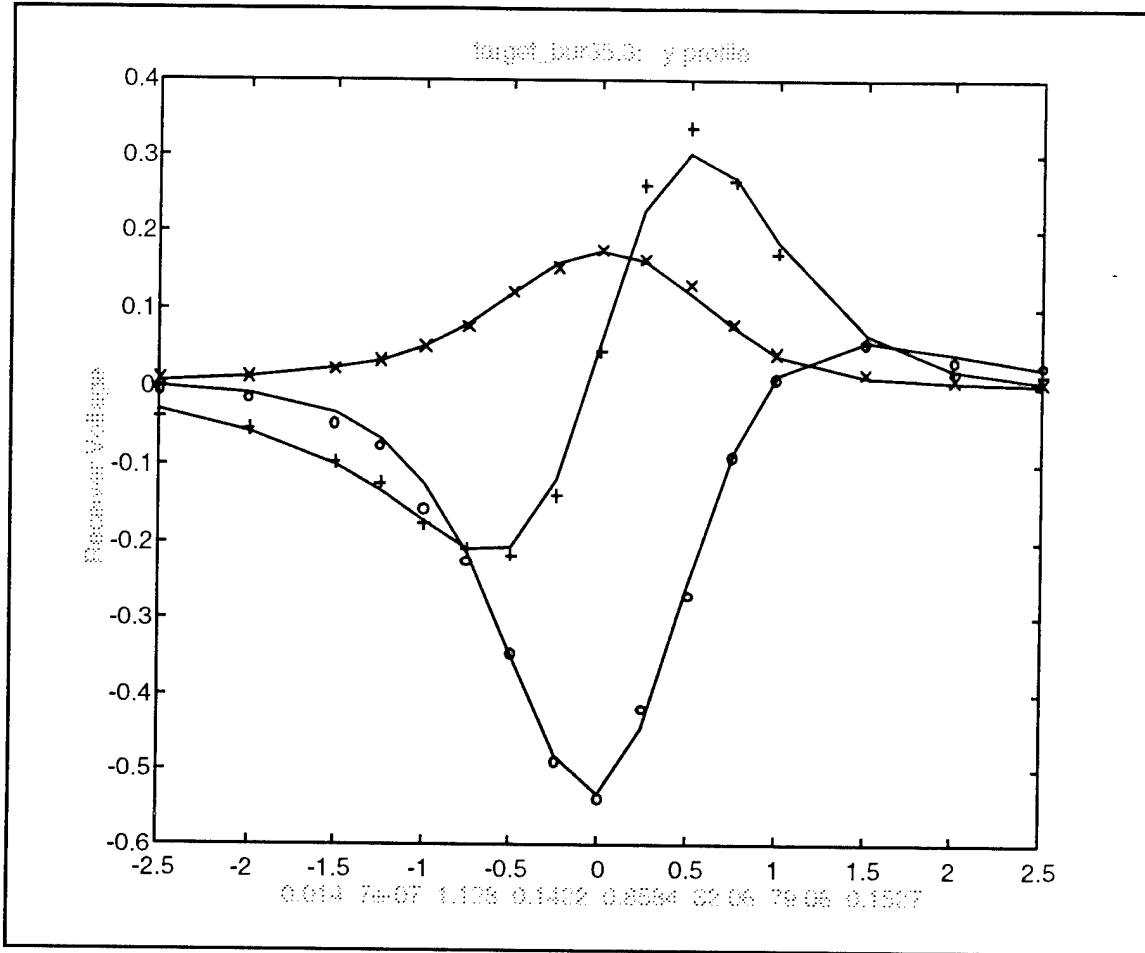
Figure 31: Fitted data from one profile of the 80 mm shell (35 degree tilt)

Table : Results of the buried 80 mm shell tests. Errors are within bounds of mechanical measurement uncertainty of knowing exact shell position and orientation.

Table 10: Results of the buried 80 mm shell tests.

Target		80 mm (0 deg)	80 mm (35 deg)
x (m)	True	0.0	1.05
	Fitted	0.10	1.19
y (m)	True	-2.5	-1.90
	Fitted	-2.72	-2.36
z (m)	True	1.1	0.7
	Fitted	0.99	0.85
Tilt (deg.)	True	0	35
	Fitted	9.5	34.6
Orientation	True	-	90
(deg.)	Fitted	-	68

4.1.9. Noise Cancellation Results

Data was collected at the Mukilteo site to evaluate the feasibility of noise cancellation and to determine the necessity of including it in the next phase of testing. A series of data sets were taken to characterize the background noise during which the transmit coil was not active. Two identical 3 axis PEMI receive coils were placed in the test area and multiple data records gathered for various separation distances. Based on this data optimal weights were computed for each configuration, and the actual degree of noise cancellation determined.

Figure 32 shows a representative set of data collected during this phase. In both plots the reference coil response has been displaced vertically to allow for easy comparison. Both the X and Z axis response show obvious correlation between the two receiver responses. However, there is also a visually apparent degree of noncorrelation, especially at the higher frequencies.

This page is intentionally left blank
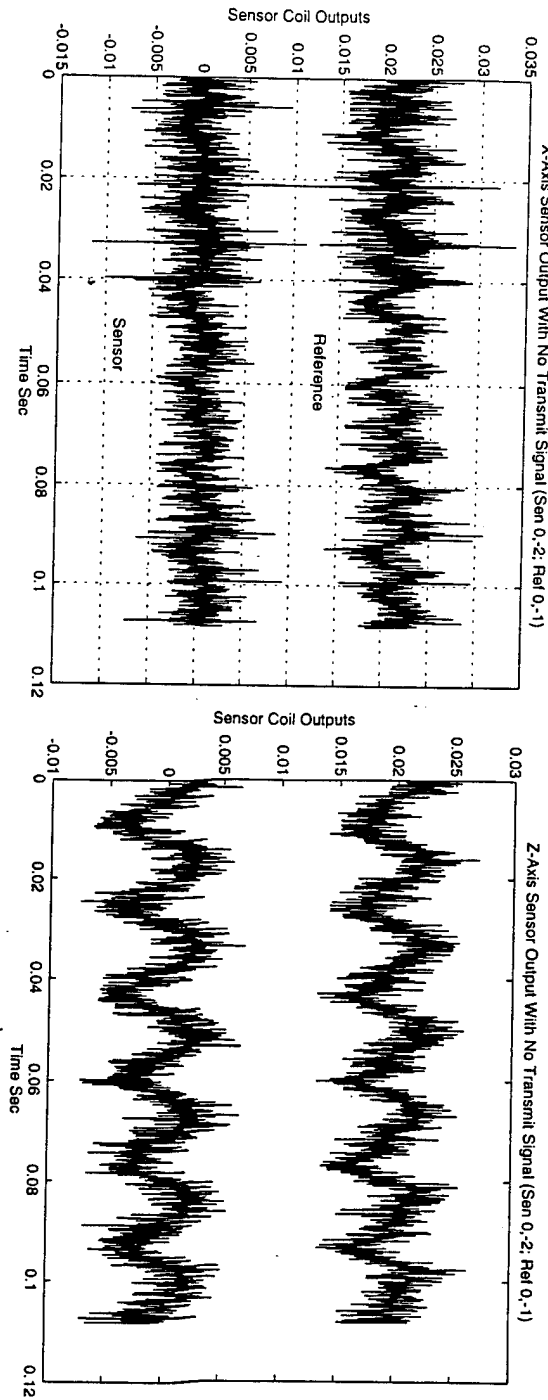
Figure 32: Example Sensor Coil Outputs in Background Magnetic Noise

The actual degree of noise cancellation, as a function of sensor separation, is shown for all three sensor coils axis in figure 33. The best result is an improvement of 7 dB on the Z-axis, but there are also cases where the improvement is less than 3 dB. While these results show that noise cancellation does improve performance, we did not approach the level of cancellation demonstrated in underwater applications.
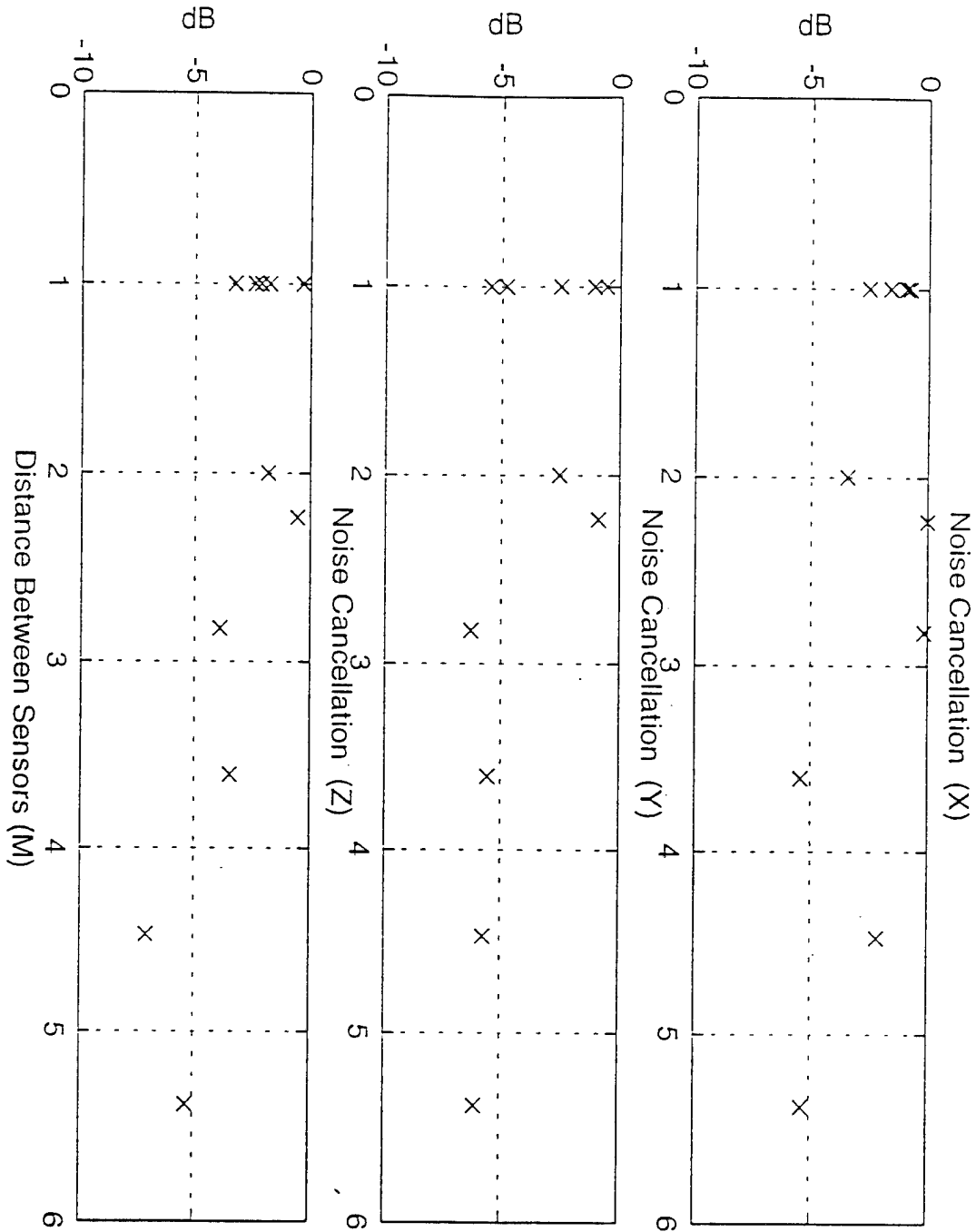
Figure 33: Measured Noise Cancellation Gain at Mukilteo Test Site

The power spectrum of the noise output is shown in Figure 34. In the top plot the spectrum of the PEMI sensor clearly shows a strong concentration of energy near 60 Hz and its harmonics. Based on previous data, and a little common sense, it is logical to assume this energy is from man made sources. The bottom plot shows the spectrum after noise cancellation. For frequencies below 200 Hz approximately 6 dB of noise cancellation is achieved. The majority of the noise power is contained in this frequency regime, so the total noise cancellation in this case is about 6 dB. About 10 dB reduction of the narrow band tonals between 400 and 1000 Hz is shown. In the high frequency regime (i.e. above 1000 Hz), noise cancellation produced little change in the noise floor. However, since the majority of these signals are out of the frequency band of UXO target signatures this should not pose a significant problem.
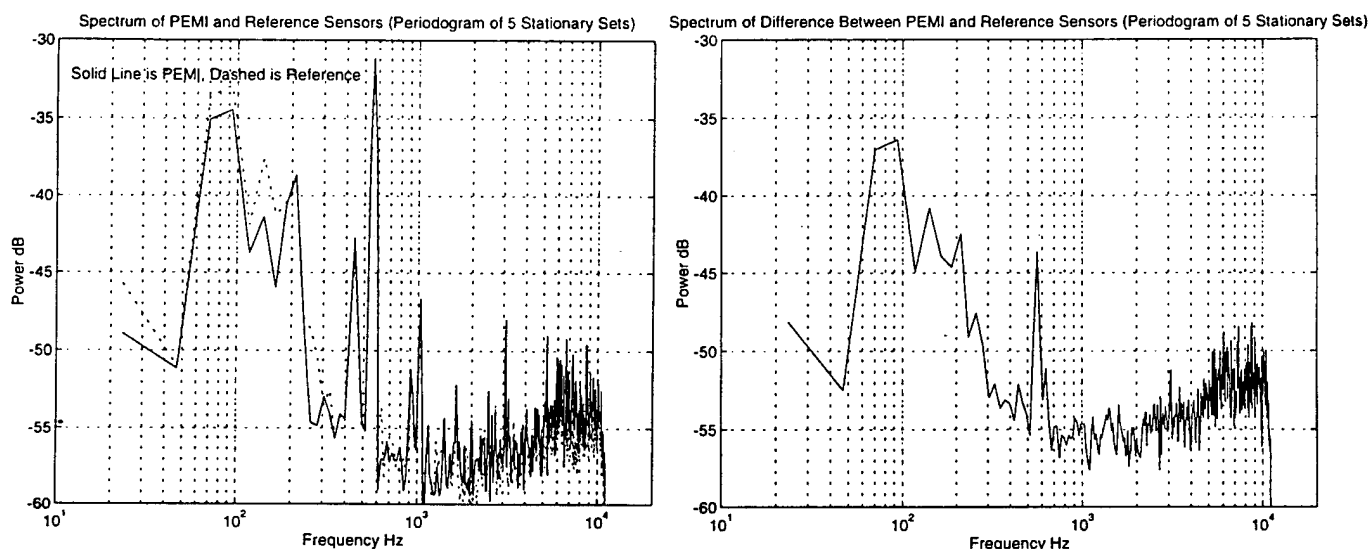
Figure 34: Power Spectrum of PEMI Before and After Noise Cancellation at the Mukilteo Site

The primary conclusion reached from examining this set of data is that the magnetic background noise at the Mukilteo site is dominated by man-made noise sources for which the spatial coherence is not as high as for natural phenomena. It is not known whether this noise is produced by the PEMI test equipment or is general background noise from the local population centers. While PEMI performance is improved by noise cancellation in this environment (3 - 6 dB), it is not as effective as has been demonstrated in other fields of magnetic sensing.

4.2. NAVEODTECHDIV Magnetometer Test Range

The NAEODTECHDIV test site, known as the "magnetometer test range", is a plot of land on the base in which several specimens of inert ordnance were buried some 15 years ago. These inert UXO serve as realistic targets for testing various methods of detection and classification. Three sites were selected and marked by EOD prior to the arrival of the PEMI field crew. The purpose of the test was to examine the performance of the testbed PEMI system developed during this contract. No information regarding the specific locations or types of ordnance in the selected sites was available to the contractor, though the general class of ordnance expected in the sites ranges from 60 mm shells to 2000 lbs bombs. Other objects, conductive or ferromagnetic, may also be present.

4.2.1. Site Overview

The sites were approximately level, and covered with low cut grass and other vegetation. The sites were approximately square, 10 meters on a side, and were located relatively close to each other. Precise survey tie-ins were done at the end of the test week to connect the survey grids to the magnetometer range reference point (a nail head in the center of a tree stump about 35 meters southwest of the three sites). This was done in order to express the locations of any targets discovered during the survey in terms of the magnetometer test range coordinates as well as with respect to the local grid for each site. A scale map of the survey sites is presented in figure 35.

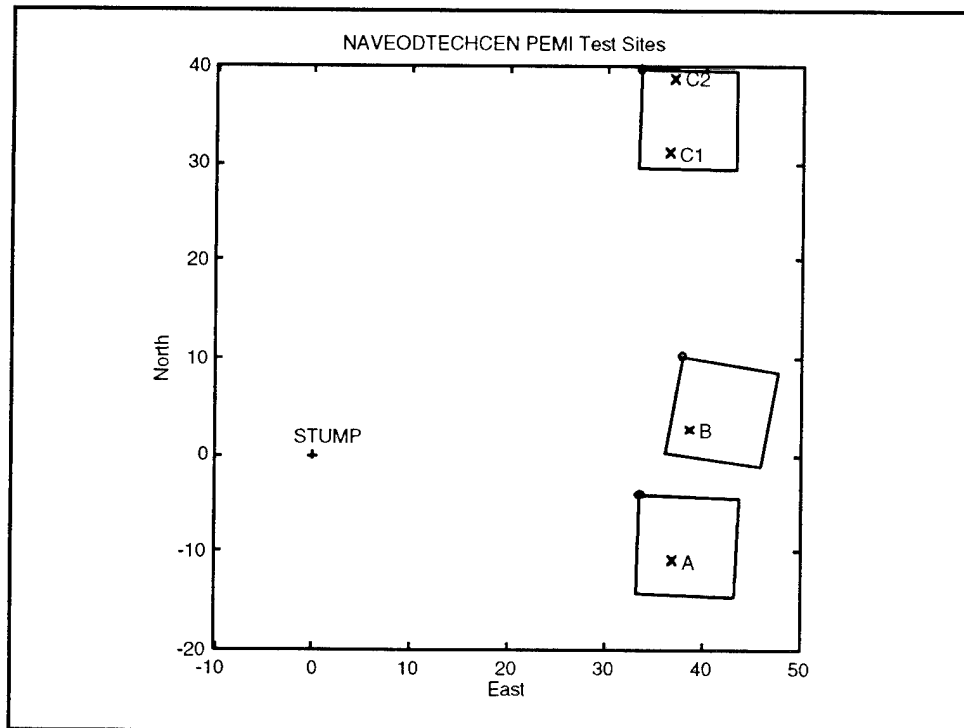Figure 35 Test site map.

Table 11 Site locations of targets located with the detailed PEMI profiles, expressed in mag range coordinates, that is, referenced to the nail head in the middle of the "stump". The bearings are in degrees with respect to magnetic North, and distances are in meters. Depths are positive downwards, and are referenced to the grade of the nail head. Rectangular coordinates for each target, in terms of the distance along magnetic North and East directions, are also given.

Table 11: Inversion Results for the Target in Site A.

Target	Bearing (deg)	Range (m)	Depth (m)	North (m)	East (m)
A	106.3	38.5	0.89	-10.8	37.0
B	86.0	38.7	0.16	2.71	38.6
C1	49.6	47.9	0.54	31.1	36.5
C2	43.6	53.6	0.65	38.8	36.9

Each of the sites was gridded and marked by stakes and string on a 1 meter interval as described in the test plan (Appendix C). The local origin was taken in the "lower left hand corner", or the NW corner of each grid, with a right-handed coordinate system taken so that the x-axis was increasing approximately towards the East, the y-axis increasing to the South, and the z-axis increasing downwards indicating depth in positive numbers. The local origin was marked by a grade stake, the height of which was used as the local depth z=0. This reference origin (0,0), and the three other grid corners (10,0), (10,10), and (0,10) were tied in to the magnetometer range coordinate system. All survey results will be reported in local coordinates first, with a table indicating the magnetometer range coordinates for each target at the end of Section 4.2 and in the report summary.

The test procedure for each site is described in detail in the test plan (See Appendix D). In summary, the approach was to lay out the grid and the 5x5 meter transmitter loop in the center of the grid (5,5), and to prepare the PEMI sensors which, in addition to the pair of electrical sensors and cables, also included a water level. The level consisted of a reservoir attached to the PEMI platform out from which a water filled tube was extended to a meter stick fixed to a vertical post. The level in the reservoir was assumed to be fixed with respect to the PEMI sensor and was the same as the level on the meter stick, thus allowing a simple reading of the sensors' elevation.

The PEMI sensor platform was a flat board on which were mounted two identical 3-axis coils. These two sensors were parallel to each other and separated by one meter, making measurements on the one meter grid twice as fast as would be possible using a single sensor. At each station, the PEMI platform was visually positioned in the (x,y) plane using the grid strings to within approximately 5 cm and about 5 degrees. The platform was leveled using a three point support system and perpendicular bubble levels. The vertical position of the sensors was known to within a centimeter. Each station took about two minutes to measure, including moving and leveling the platform, reading and recording the level, and taking the data. Under ideal conditions, with a grid in place, a "coarse" survey was done in about 2 to 3 hours.

Each site was first surveyed by making measurements at every string intersection, that is over the entire site on a one meter grid. This coarse survey was intended to be used as a guide for locating finer grids over targets of interest, but equipment problems prevented processing of

the PEMI data while in the field. Instead, the results of the magnetometer survey directed the acquisition of detailed PEMI data. Results of the coarse PEMI survey are presented and discussed for each site in the following sections.

Once targets of interest were identified and approximately located using the magnetometer data, a pair of perpendicular profiles centered over the expected target location was surveyed using a 50 cm spacing between stations. The stations between string intersections were not precisely marked. The PEMI sensor platform was located by visually centering the sensors between strings. This procedure was not deemed to have increased the uncertainty in the data significantly.

4.2.1.1.Field Notes, Modifications, and Procedural Changes

The signal to noise in the data was constantly monitored by examining the data acquisition display of the time series. Several targets presented a very weak response using the 5x5 meter transmitter loop. The most straightforward way of reducing noise is to increase the number of PEMI pulses over which the time series are averaged. Commonly, 20 pulses were used, but up to 200 pulses were "stacked" in some instances. Lowering noise by increasing averaging time reaches practical limits rather quickly because improvement goes as the square root of the number of pulses at best, while the acquisition time increases linearly. In order to improve the signal to noise level as much as possible, the transmitter loop was occasionally folded over in such a way as to quadruple the number of turns while simultaneously reducing the area of the loop by a factor of 16 (reduced side length 1.25 meters). This configuration is referred to as the 1.25 meter or small transmitter loop. The small loop effectively concentrates the available magnetic energy in a smaller area to emphasize responses from very nearby conductors.

The principal problem encountered during the EOD site field work was caused by power supply problems with the data acquisition Macintosh computer. The Mac Quadra has a sophisticated power supply which senses the voltage and frequency of the line and only allows the computer to turn on if the power quality falls within certain limits. The generator apparently did not provide the proper power once at Indian Head, though the entire system was tested in Mukilteo before shipping and performed without difficulty. Though a replacement system was mailed out from Seattle in a day, it suffered from the same flaw. Fortunately, the data acquisition hardware and software was successfully ported to a different platform intended as the data processing computer, the Power Macintosh 7100. This machine uses a completely different CPU than the Quadra and we were very fortunate to be able to recompile everything and get running again within a day. The acquisition computer then ran without fail for the remainder of the field work, though the other machines were never reliable enough to make much progress with processing the PEMI data in the field.

Due to power system induced computer failures, an analysis computer was not reliably available for operation in the field and the coarse PEMI survey data could not be processed to the degree required for reliable target detection. Consequently, the magnetometer data was the main data source used for determination of the location of sites for the PEMI fine surveys.

4.2.2. Site A

Site A was the first one gridded and surveyed. Of all three sites, the ground in A was the most level and clear of vegetation. The magnetometer survey located one distinct anomaly which resulted in our choice of cross profiles centered on station (x=4,y=7). The PEMI coarse survey corroborates this result, as the target was relatively easy to find. The transmitter loop used in the detailed survey was centered at (5,6), that is, just moved over by a meter from its previous location so as not to have its edge right over the target. Near the transmitter wire, the field is strong and has a complicated shape; thus, precise knowledge of the wire geometry would be necessary to provide good agreement between model and data.

4.2.2.1.Magnetometer Results

The results of the magnetometer scan of Site A, which were taken on Tuesday July 25th, are shown in Figure 36. All magnetometer data shown in this report were taken with uniform spatial sampling of 1/2 meter. From this figure it is clear that a strong target is located at about (x=7,y=4). This is the strongest (50 nT/m) target in any of the three test sites.
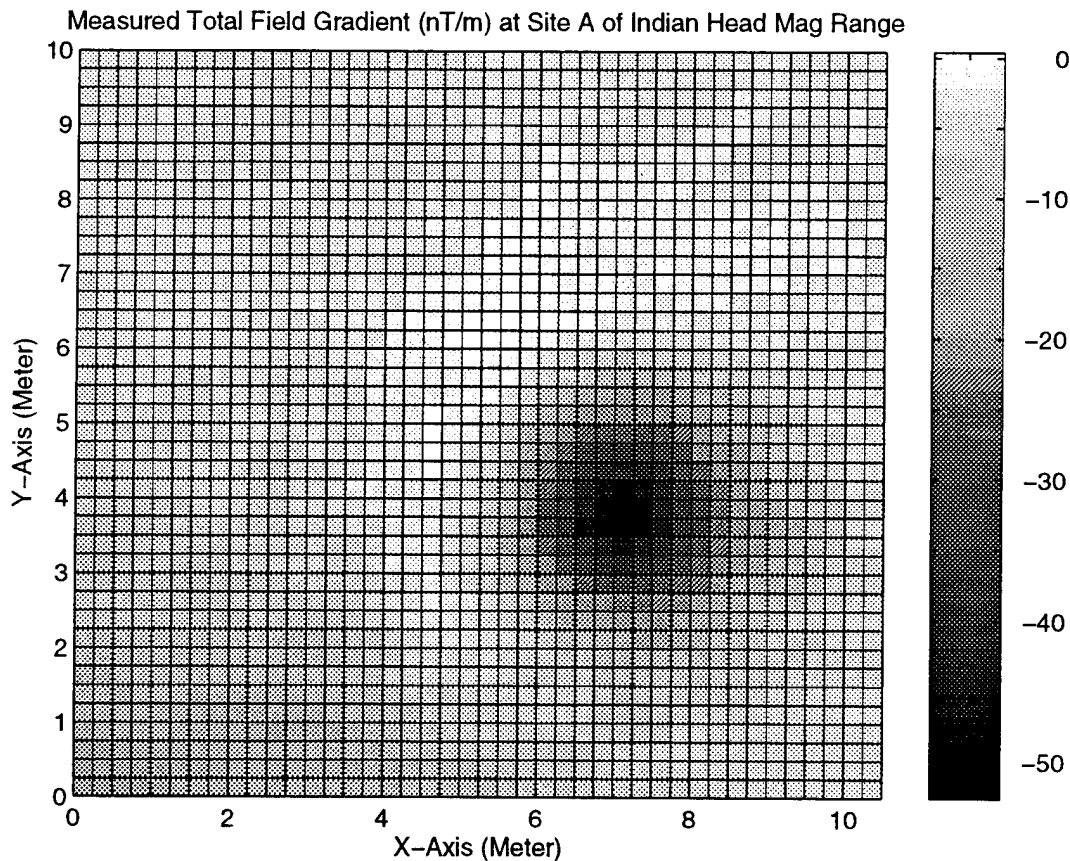
Figure 36: Magnetometer (Gradiometer Mode) Scan of Area A

4.2.2.2.Coarse PEMI Survey Results

The PEMI survey of site A was not processed in any detail in the field, however it is useful to see how such data compares with the magnetometer data which took a similar amount of time to collect.

The first step in processing the data after having sorted the data files from each of the two sensors into a convenient order is to fit a decaying exponential function to the time series, over a reasonable time window. In this case, knowing that most ordnance will have a time constant of at least 10 ms, a preliminary data window was chosen between 10 and 50 ms. The result of this fit is to obtain, at each station and for each field component, an amplitude and a decay time constant. The amplitudes for each component are plotted as a function of position in figure 37. (Also plotted are the sensor elevations, to within an arbitrary mean level.)

Figure 37 Site A: Results of PEMI Coarse Survey.

While the anomaly near (4,7) appears clearly over many stations, a few other "spikes" appear as well. It turns out that such clutter in the data can be easily filtered out in this case, because the time constants associated with the spikes are too short to be of interest. Setting a mask filter which rejects any data outside the desired bounds for time constants, here selected to be

between 8 and 30 ms, and rescaling the data to fully emphasize what is left after filtering produces the plots in figure 38. The spikes are gone, and the full extent of the target response is visible. Because this site contains a relatively easy target to find, it is a convenient one to illustrate the data processing steps and their effects.
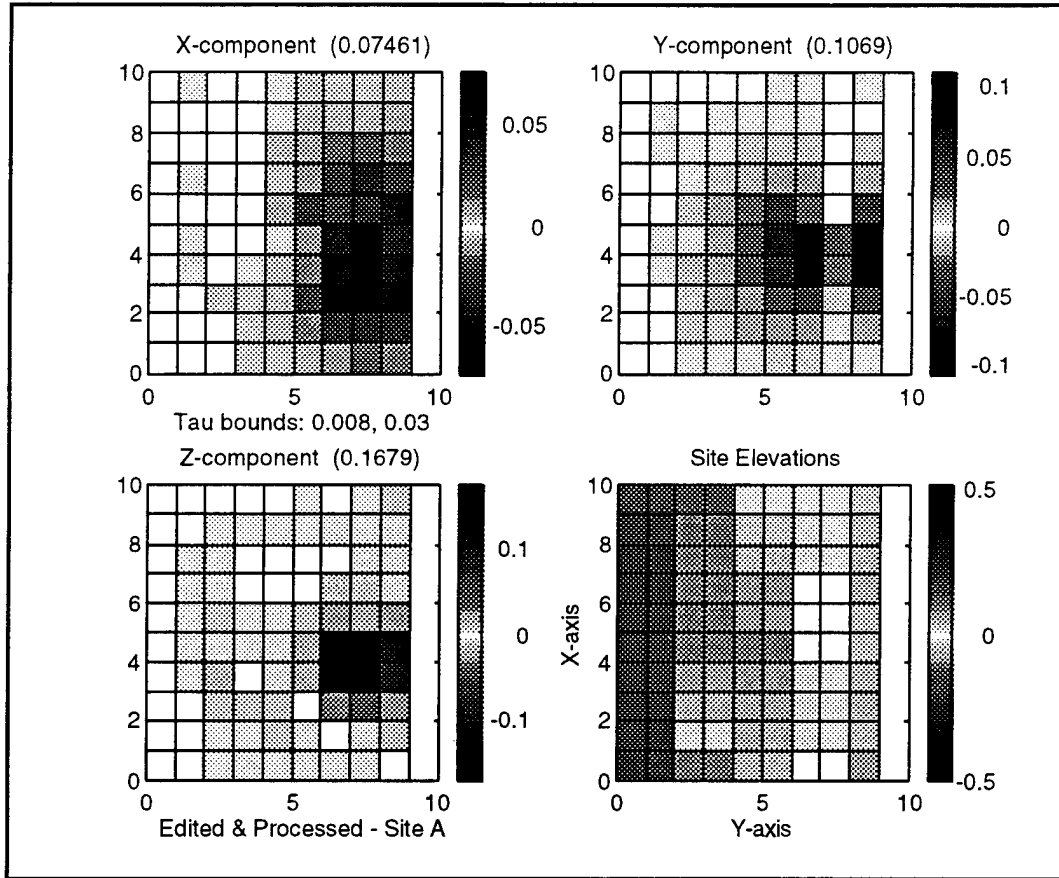

Figure 38 Site A Coarse Survey Results (Amplitudes filtered by inclusion only of time constant between 8 & 30ms)

4.2.2.3. PEMI Fine Survey Results

The fine survey was carried out by moving the sensor platform over two perpendicular profiles, which actually gave rise to three data profiles because of the way the two sensors were used. The orientation of the coils (and their position on the platform) was maintained throughout the survey so that sensor #2 was always at ($x2=x1$, $y2=y1+1$). Consequently, x-profiles taken along a line of constant y lead to a pair of data profiles, while a y-profile allowed the data acquisition to proceed twice as fast by leapfrogging stations. A pair of crossed profiles gives a lot of information about the (x,y) location of the target, though in some cases two parallel profiles may be sufficient to obtain a good estimate of target position in the direction transverse to the profiles.

As in the coarse survey, the time series at each station (50 cm spacing) is fit using DLS inversion to obtain an amplitude and a decay time constant. The "best estimate" time constant for the target is obtained by weighted average from the profile data, that is by weighting each

time constant by the amplitude of the fit at that station. In this case, the target has a time constant of 18.6 ms.

A plot of the data and the best fit thin-ring model obtained by spatial DLS inversion is presented for all three components in Figure 39, for one of the profiles only. The inversion processing is done for all profiles simultaneously, but for clarity the results for only one are plotted. As in previous plots, the symbols used for each component are x='x', y='+', and z='o'. Results of the inversion are given in table 12.

Table 12: Inversion Results for the Target in Site A.

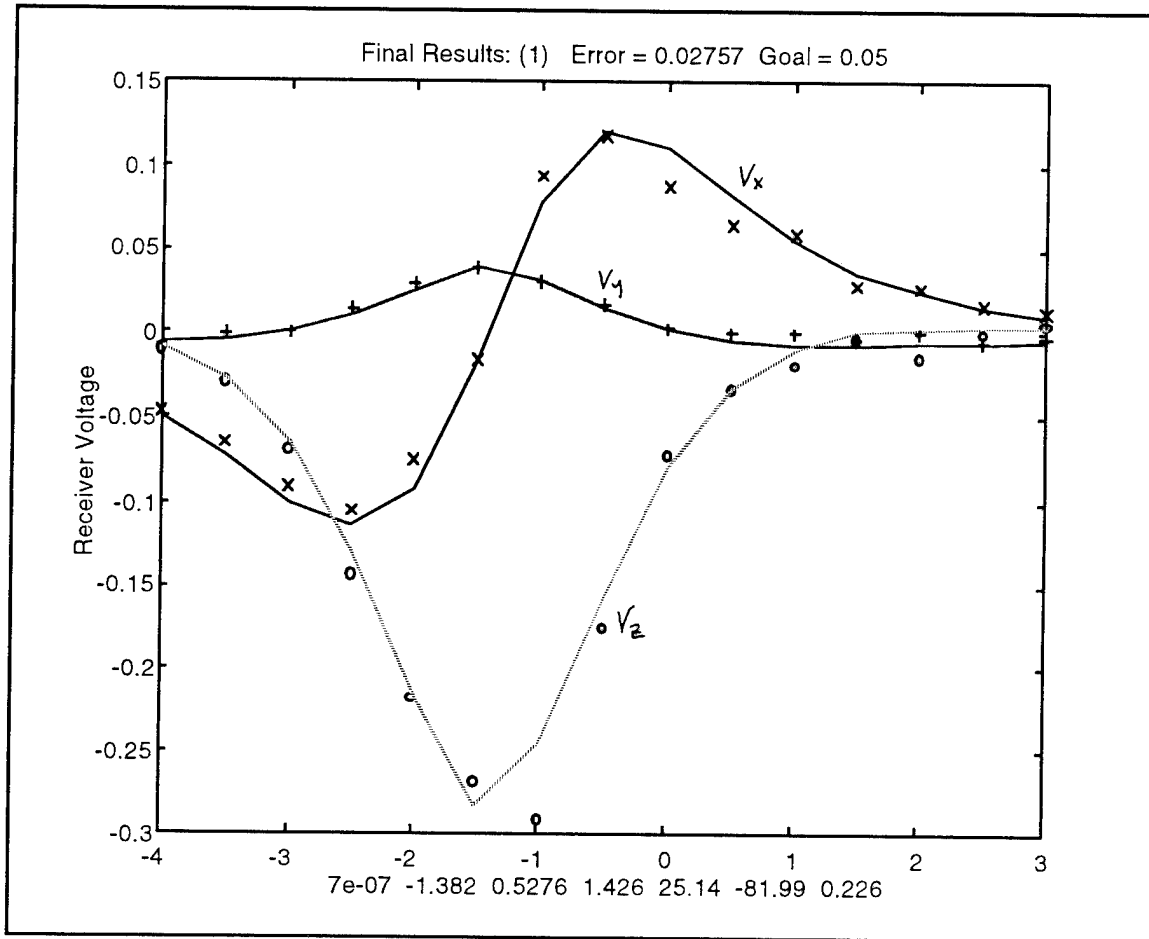| Spatial Parameters		Target Parameters	
Relative Mean Squared Error	0.0276 m	Target Tilt angle	25.1 Deg
Target X-position	3.62 m	Target Bearing	-82.0 Deg
Target Y-position	6.53 m	Target Effective Radius	0.226 m
Target Z-position	1.43 m	Target Effective Inductance	7E-7

Figure 39: Amplitude data from profile Y=7 and the associated "best fit" PEMI ring model result.

4.2.3. Site B

Site B presented more of a challenge, in that there were no large targets detected. Consequently, the site survey plots appear noisier. The magnetometer survey indicated a possible target near the West edge of the grid, and a detailed PEMI x-profile was measured over x=[0,3], for y=7 (sensor #1) and y=8 (sensor #2). A conductor was confirmed to exist near the center of the small 1.25 meter transmitter coil which was placed at (2, 7.5) for the detailed survey. The estimated time constant of this conductor is 21 ms.

4.2.3.1.Magnetometer Results

The magnetometer results for site B, which were taken on Wednesday July 26, are shown in figure 40. The top plot is the initial scan of the area, and shows a possible target near (8,1). However, during this run the truck which housed the PEMI electronics and data acquisition equipment was parked about 100 feet away from the lower right corner of the site, and its response is masking the target. The lower plot shows a scan of the lower quadrant of the site taken on Thursday July 27 when the truck was at another site. A weak target (6 nT/m) can be seen at about (7.7,2).
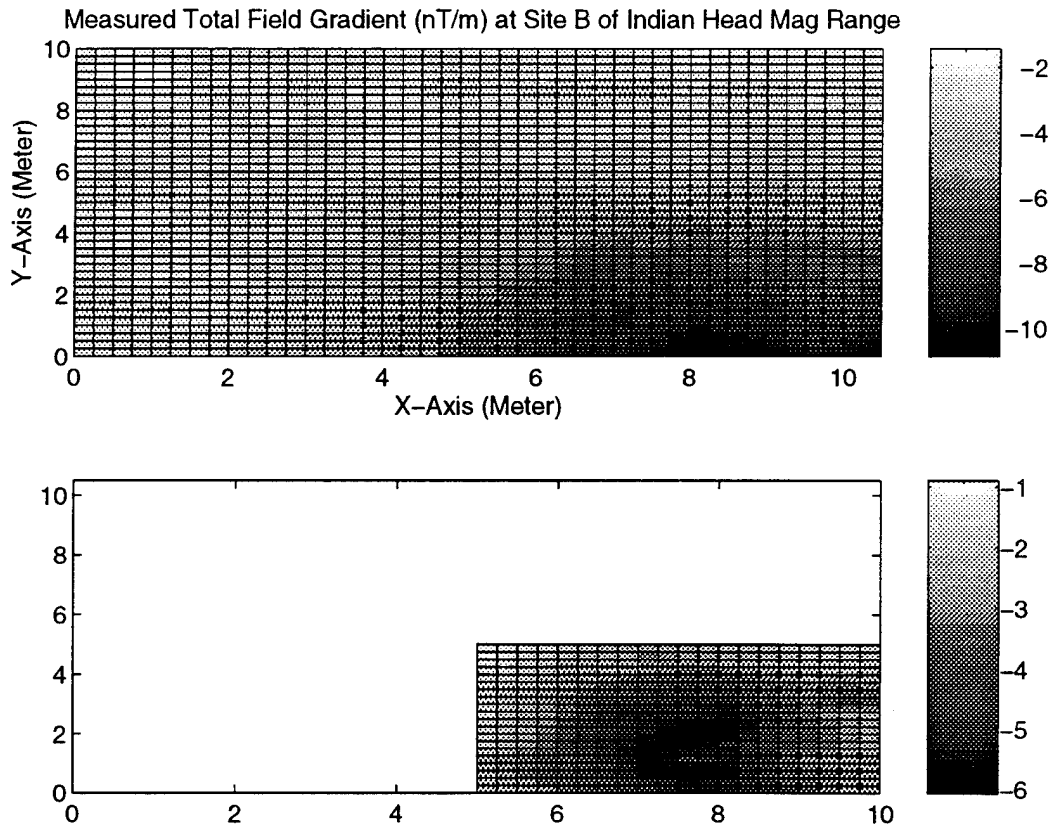

Figure 40: Magnetometer (Gradiometer Mode) Scan of Site B

4.2.3.2.PEMI Coarse Survey Results

Results for the PEMI coarse survey are presented in two figures. First, the amplitudes from the DLS processed time series data is plotted for all stations in Figure 41A. In this case, it is also helpful to screen out points which do not correspond to reasonable decay time constants. The masking of all amplitudes which were not associated with 5ms < tau < 22ms results in the plots of Figure 41B. While the area surveyed in detail near (2,7) does appear of interest, another area near (7,5) also seems to have stronger than background responses. However, since the processing of the data was not possible due to computer malfunction only the area indicated by the magnetometer data was finely surveyed by the PEMI method.
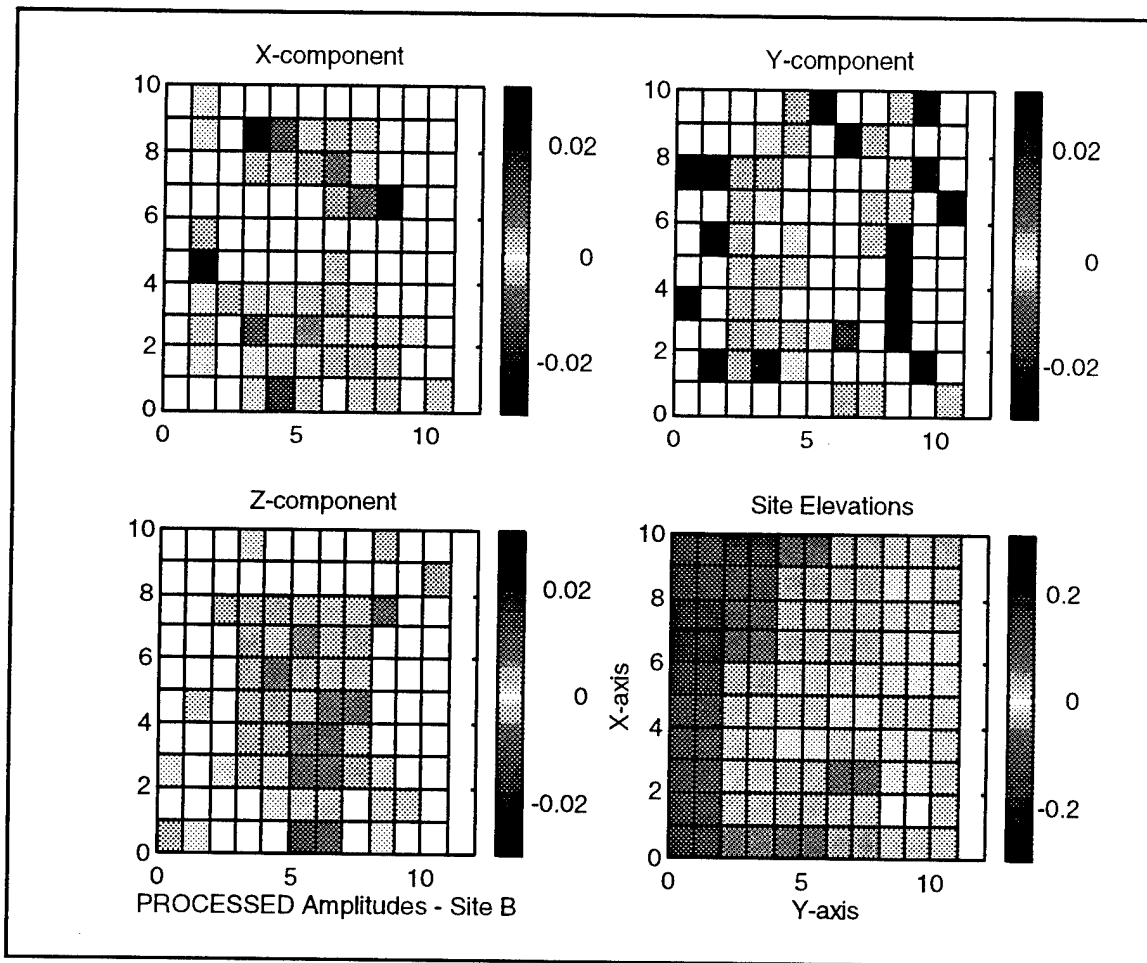

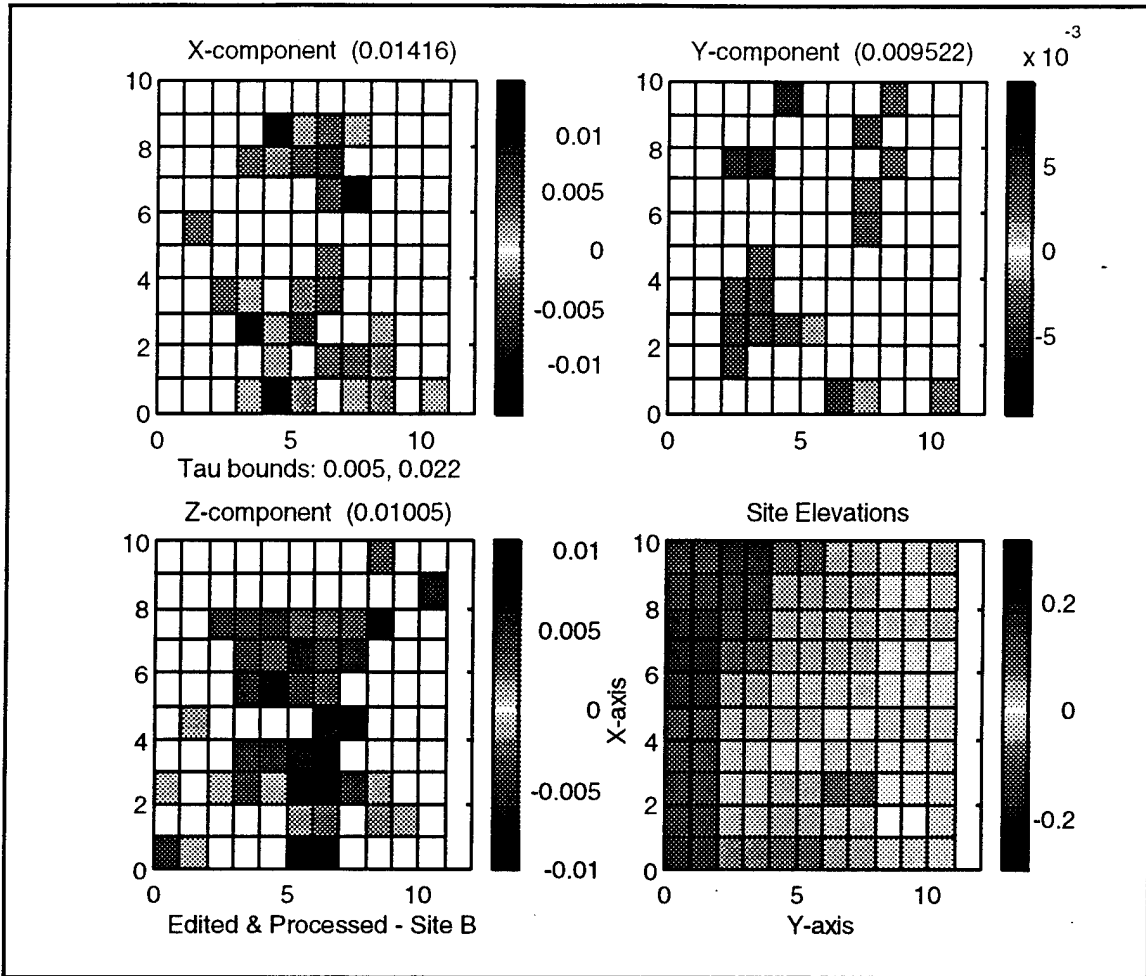Figure 41A Site B Coarse Survey Results

Figure 41B Site B Coarse Survey Results (Amplitudes filtered by inclusion only of time constant between 5 & 22ms)

4.2.3.3.PEMI Fine Survey Results

The area in the vicinity of (2,7) was subjected to a PEMI fine survey. An illustration of the model fit to the data is given in Figure 42, for the best fit parameters from fitting just the y=7 profile. The 1.25 meter transmitter loop was centered at (2,7.5), and x coordinates in the plot are given with respect to the transmitter loop center position. Finally, the spatial DLS inversion of the two sensor profiles taken together yields the target parameters given on the same page.
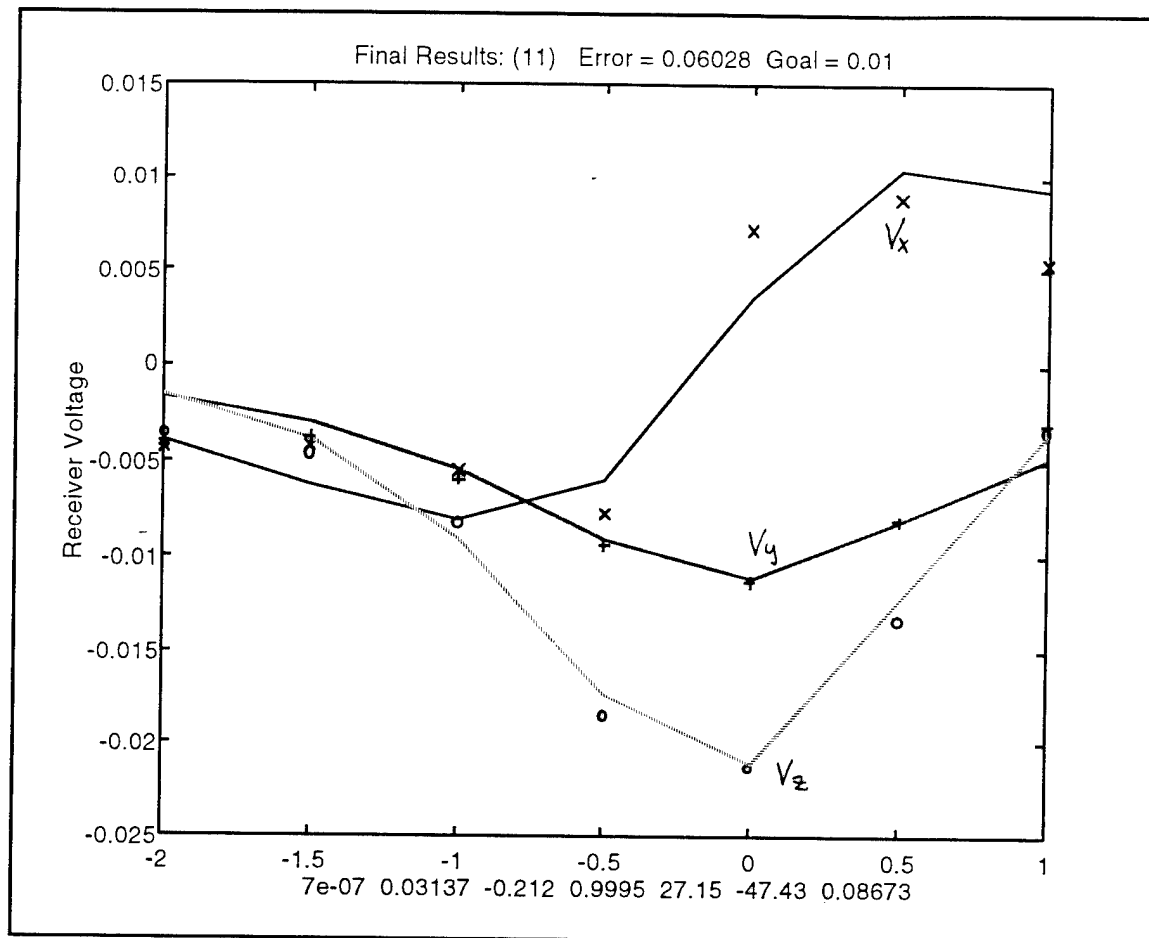
Figure 43 Site B - Thin ring model fit to the data from the x-profile taken at y=7.

Results of the inversion by DLS of data from both profiles y=7 and y=8 simultaneously are given in table 13:

Table 13: Inversion results for the target in Site B.

Spatial Parameters		Target Parameters	
Relative Mean Squared Error	0.067 m	Target Tilt angle	29.6 Deg
Target X-position	2.06 m	Target Bearing	-45.8 Deg
Target Y-position	7.26 m	Target Effective Radius	0.09 m
Target Z-position	1.01 m	Target Effective Inductance	7E-7

4.2.4. Site C

Site C was the last one surveyed, and had the most elevation change and roughness across the area. Both the magnetometer and PEMI methods indicate a distinct anomaly near (3,9); this target is named C1. The PEMI survey finds that target C1 has a decay time constant of about 8 ms. A few other minor regions of higher than background response also appear. One

of these is a target (C2) located by the magnetometer and also seen in the preliminary PEMI survey. Located near (3,1) this conductor C2 is found to have a rather short time constant of approximately 4 ms.

4.2.4.1.Magnetometer Results

The magnetometer results for site C, which were taken on Thursday July 27, are shown in figure 44. This is the most complex target area. A strong target (16.5 nT/m above the background) is located near (9,3.75), and based on the dipole response appears to be at an angle. A weak target (8 nT/m above the background) is located at (1,4), and a very weak target (2.6 nT/m above the background) is at (4,1). A final target which appears to be off the edge of the defined grid can be seen in the upper right corner (8,10).

Measured Total Field Gradient (nT/m) at Site C of Indian Head Mag Range
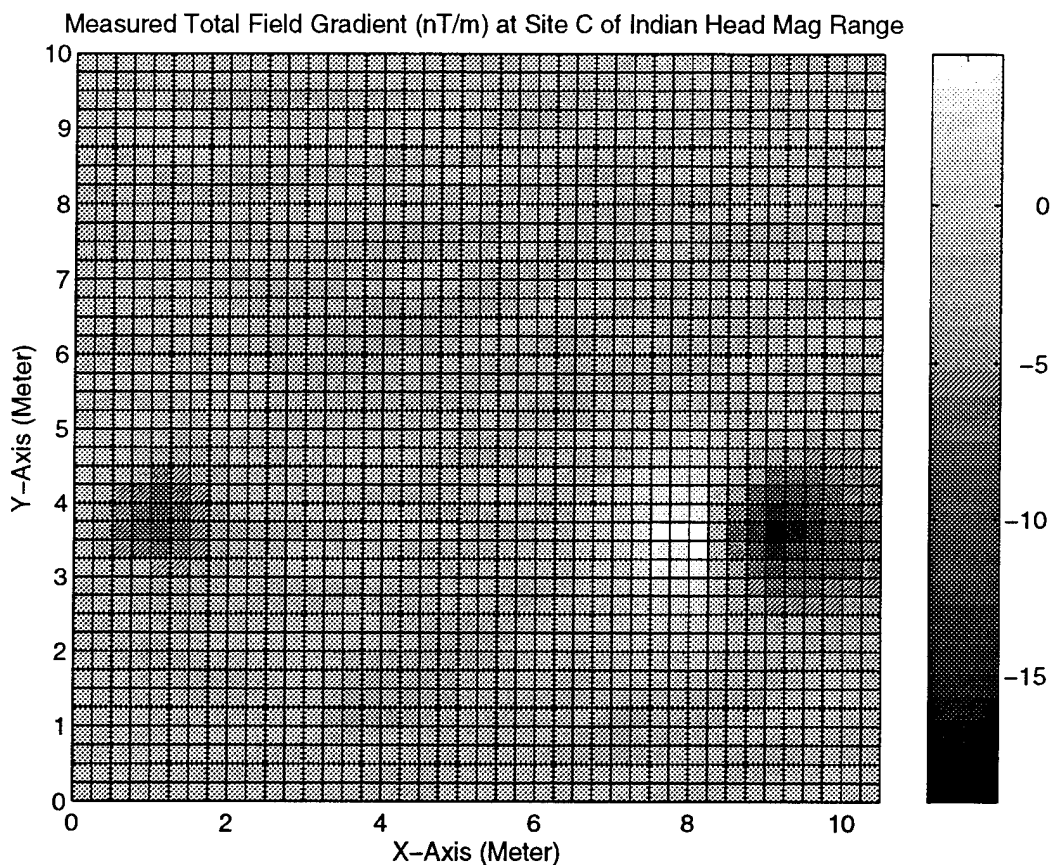
Figure 44: Magnetometer (Gradiometer Mode) Scan of Site C

4.2.4.2.PEMI Coarse Survey Results

The DLS fitted amplitudes for site C are presented in Figure 45A. Though the plot appears noisy, a target near (3,9) definitely stands out as an anomaly expressed over several stations (target C1). A typical window for acceptable time constants between 5 and 30 ms was used to filter out extraneous amplitudes to produce the plot in Figure 45B. Target C1 is clearly visible in the Z-component data; X- and Y-components indicate other targets as well. From the

detailed survey described below, it is known that target C2 is located near (3,1), and has a time constant of about 4 ms.
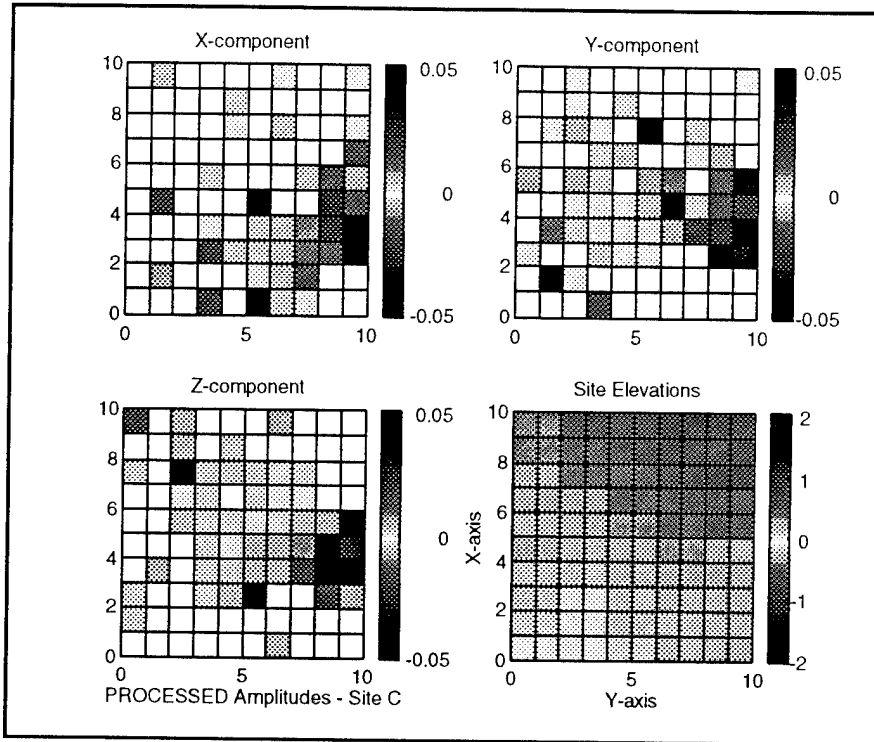

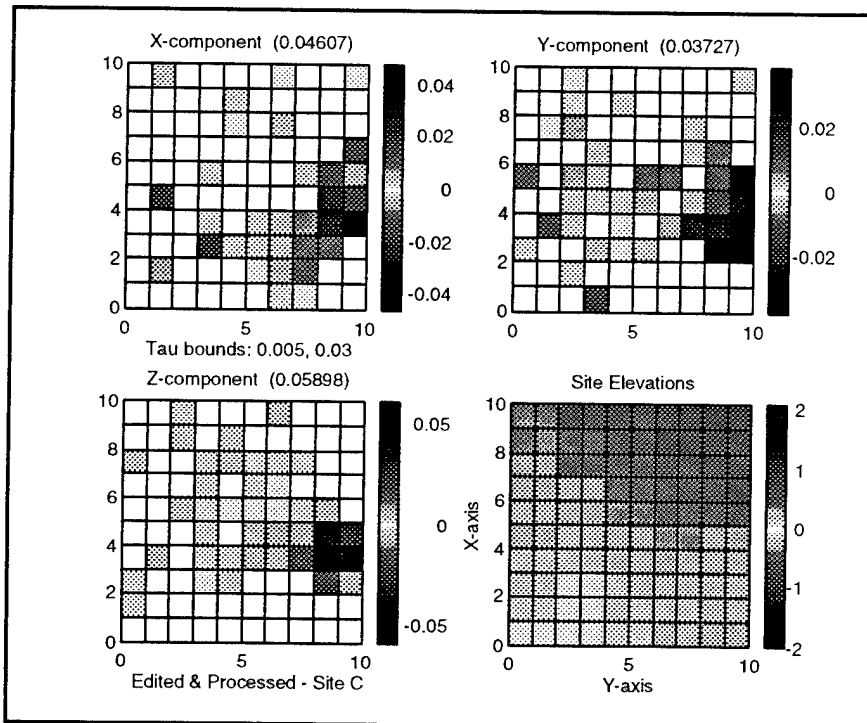*Figure 45A Site C - PEMI Coarse Survey Results.*

Figure 45B Site C Coarse Survey Results (Amplitudes filtered by inclusion only of time constant between 5 & 30 ms).

4.2.4.3. PEMI Fine Survey Results

Target C1 was surveyed with perpendicular profiles y=8, y=9, and x=3.5. For maximum signal to noise ratio, the small (1.25 meter) transmitter loop configuration was used, with the loop centered at (3.5,9). The amplitude weighted average estimate for the time constant is 8.1 ms. Figure 46 which illustrates the quality of the fit to one of the profiles (y=9). The inversion is not affected by the outlying z-component data point at (-3.5, -.55) because it corresponds to a time constant outside a 30% interval around the average time constant of the target. The spatial field model fit results for the inversion of all three data profiles are given in table 14. Results for the fit to all three profiles are a little different than the results for one profile alone. Using all three profiles provides the best estimate of target location and orientation.
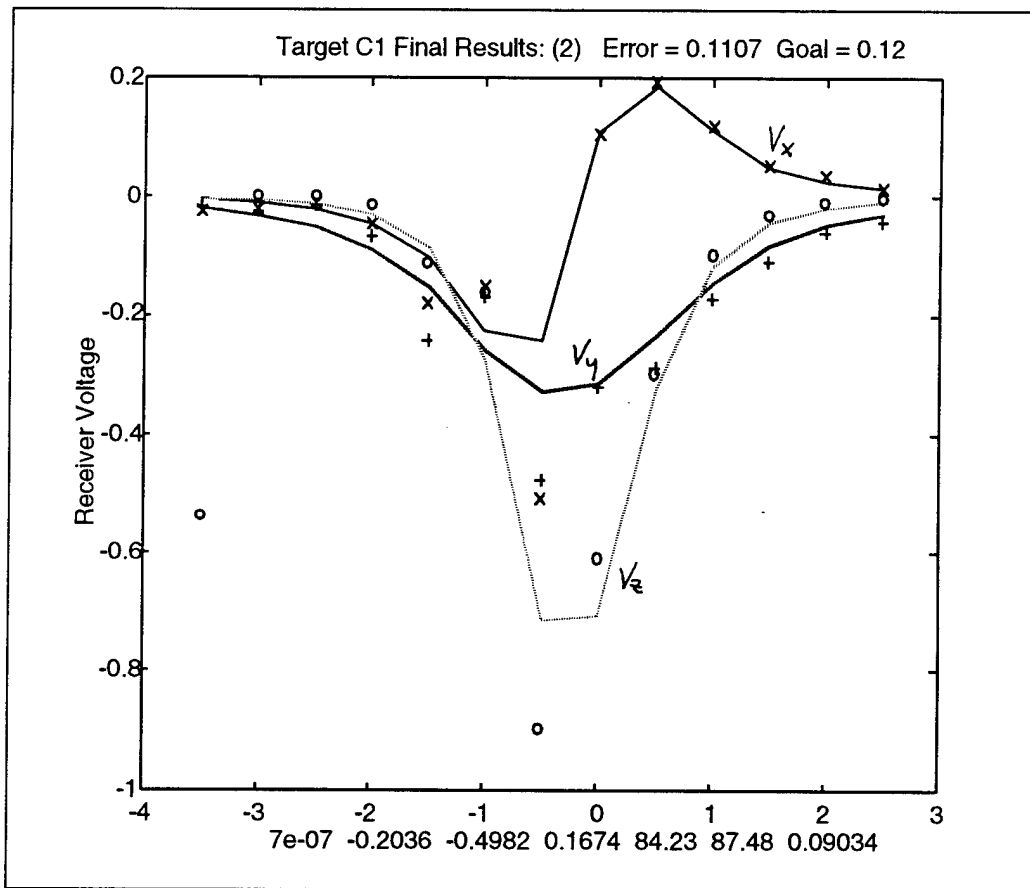
Figure 46 Profile data for target C1, from the profile y=9.

Table 14: Inversion Results for Target C1.

Spatial Parameters		Target Parameters	
Relative Mean Squared Error		Target Tilt angle	84.1 Deg
Target X-position	3.3 m	Target Bearing	89 Deg
Target Y-position	8.5 m	Target Effective Radius	0.097 m
Target Z-position	0.21 m	Target Effective Inductance	7E-7

Target C2 was surveyed with perpendicular profiles y=0, y=1, and x=3.5. For maximum signal to noise ratio, the small (1.25 meter) transmitter loop configuration was used, with the loop centered at (3.5,0.5). The amplitude weighted average estimate for the time constant is 3.8 ms. The spatial field model fit results for the inversion of all three data profiles are given below Figure 47 which illustrates the quality of the fit to one of the profiles (y=0). Results are tabulated in Table 15.
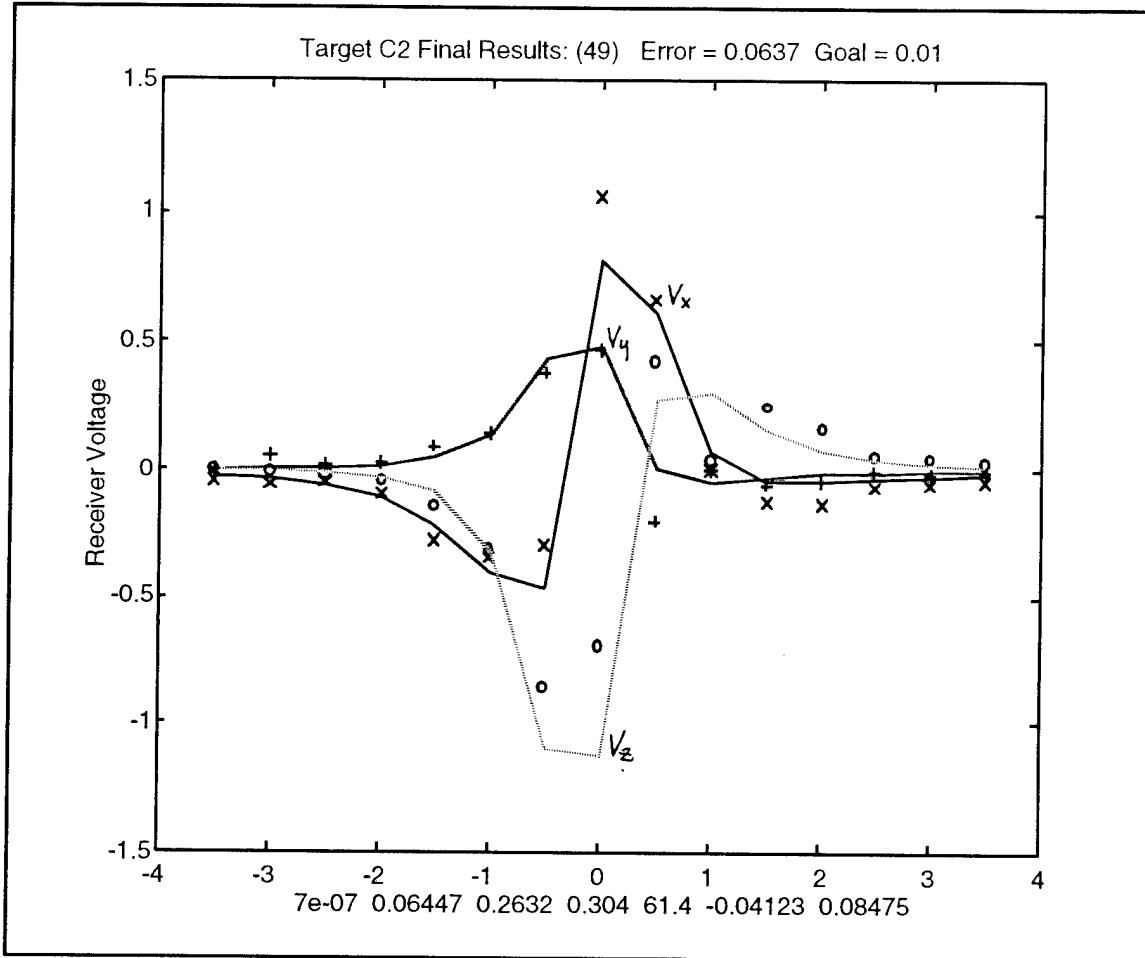
Figure 47 Profile data for target C2.

Table 15: Inversion Results for Target C2.

Spatial Parameters		Target Parameters	
Relative Mean Squared Error		Target Tilt angle	55.8 Deg
Target X-position	3.60 m	Target Bearing	-0.1 Deg
Target Y-position	0.76 m	Target Effective Radius	0.09 m
Target Z-position	0.32 m	Target Effective Inductance	7E-7

4.2.4.4.Noise Cancellation Results

Data was collected at Site C on Thursday, July 27th to evaluate noise cancellation performance at the NAVEODTECHDIV magnetometer test range. This data was collected in a similar manner to that at the Mukilteo test site. The original sample rate of the data was 24 kHz from which the data was filtered to a 1 kHz bandwidth and decimated to a 6 kHz sample rate. This preprocessing allowed for noise and computation reduction while still being compatible with the expected range of UXO time constants (3 - 30 msec). This data set contained impulse noise indicative of a near by lightning storm as well as ~60 Hz harmonic noise.

Figure 48 shows an illustrative example from the noise cancellation data collected at Site C. This data shows highly correlated impulsive noise on both sensors as well as back ground broadband noise. From the third plot it is clear that the majority of the impulsive noise can be canceled, and a reduction in the level of background noise is also achieved.
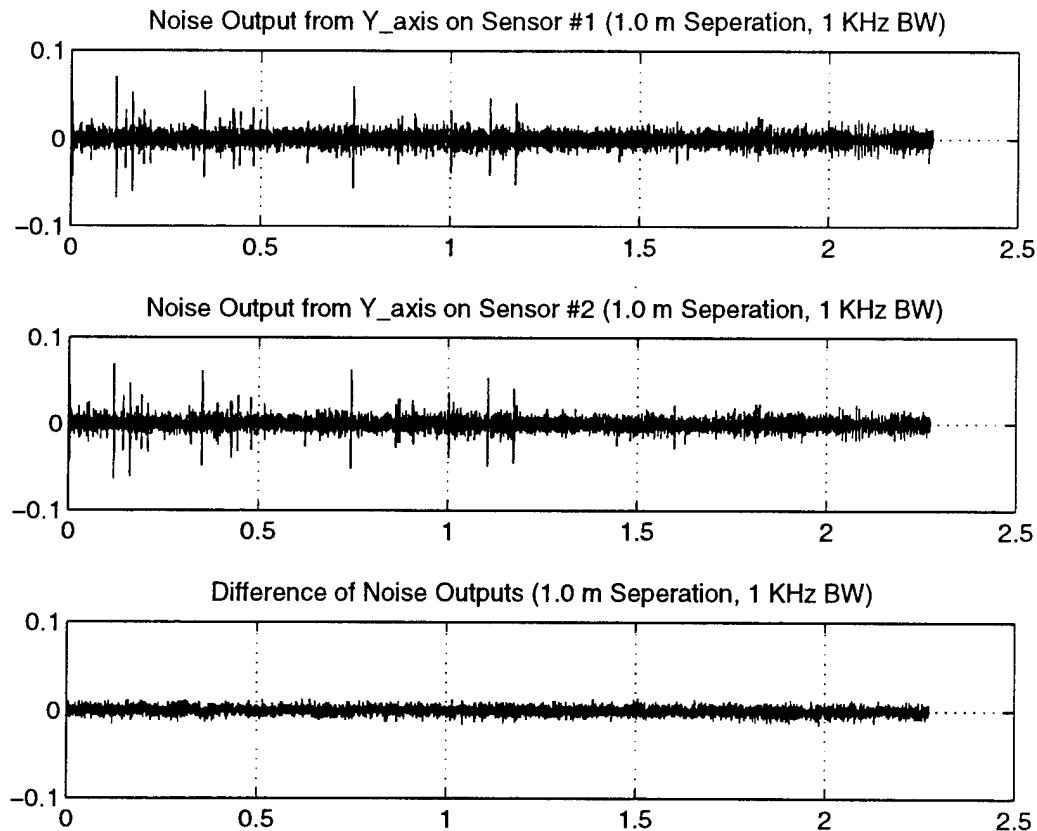
Figure 48: Example of Noise Cancellation From Site C (Y-Axis)

The power spectrum for the same data set is shown in figure 49. The noise on Sensor #1 still shows strong 60 Hz and harmonic content, but the background at high frequencies (500 - 1000 Hz) is much higher than in Mukilteo. This high frequency energy is from the lightning induced impulsive noise. Examination of the lower plot shows that subtraction of the reference sensor is most effective in the elimination of the high frequency noise (6 - 9 dB reduction). The attenuation of 60 Hz and harmonic components is smaller (0 - 3 dB reduction).

Power Spectrum of Sensor #1 Y–Axis (1.0 Meter Seperation)

3 Hz Resolution

Power Spectrum of Difference of Y–Axis Sensors (1.0 Meter Seperation)

Frequency Hz
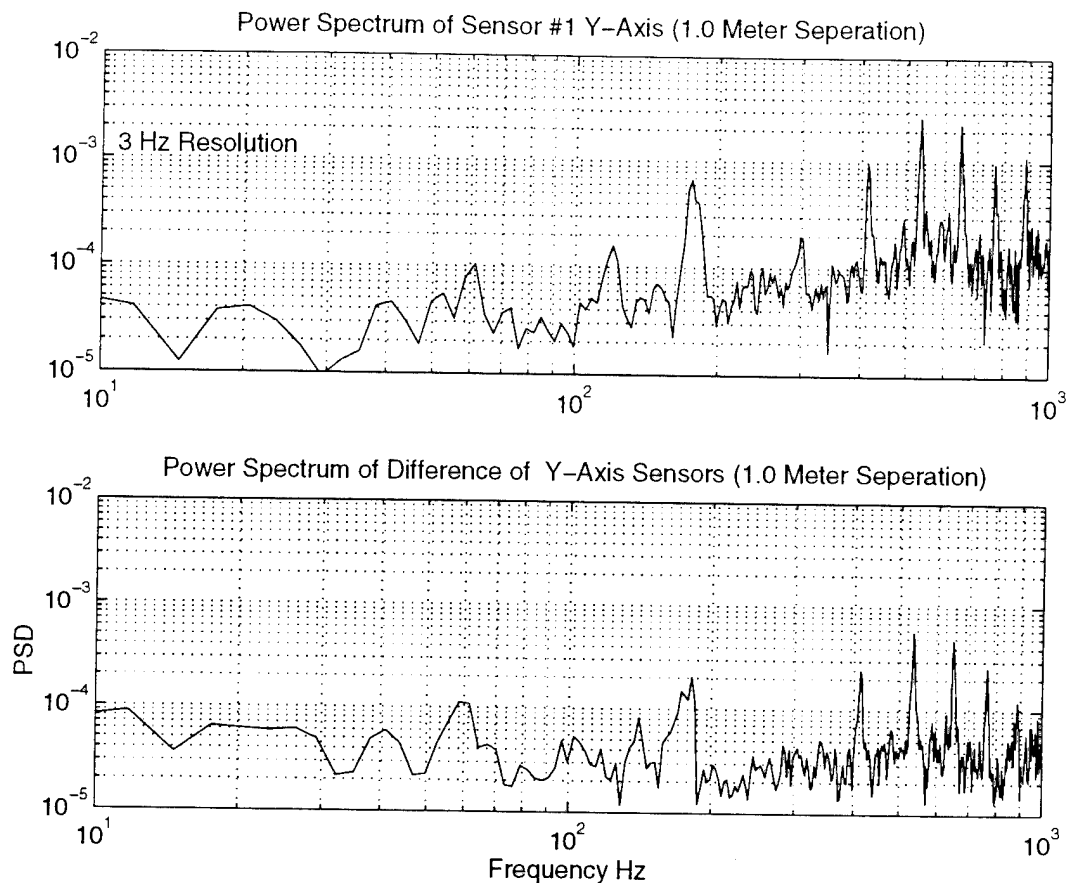
Figure 49: Power Spectrum of Noise and Sensor Difference at Site C (Y-Axis)

The measured noise cancellation improvement as a function of sensor separation is shown in figure 50. Overall, the benefit of noise cancellation is approximately 1 -2 dB better than achieved in Mukilteo, primarily due to the presence of the impulse noise from lightning. However, manmade noise still dominates in terms of total power, and the modest spatial correlation of this noise limits the effectiveness of cancellation techniques.
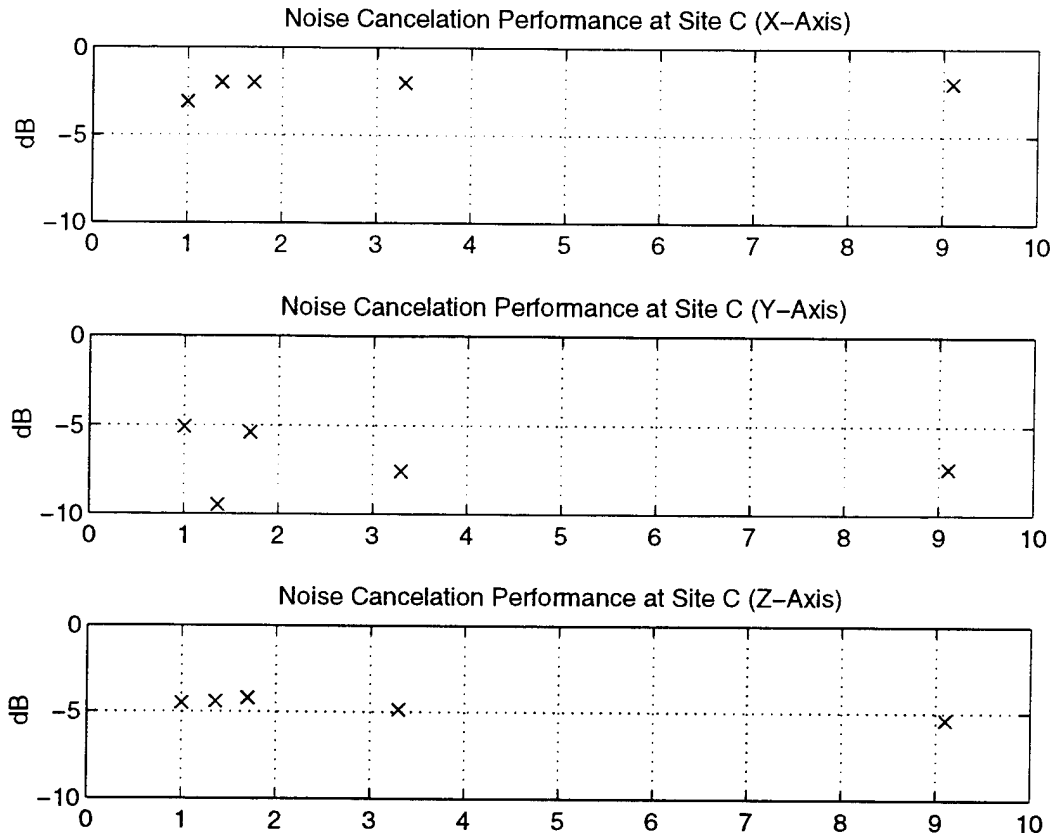
Figure 50: Noise Cancellation Performance at Site C

A final example of noise cancellation is shown in figure 51. In this case noise cancellation has been applied during actual operation of the PEMI sensor. Previously presented data has been for the noise only case, in this figure both signal and noise are present. This is representative of an operational system. Sensor #1 and the transmit coil (1.25 meter configuration) are located directly over the target at (4,9). The reference sensor is 9.4 meters away at (1.36, 0). The first trace shows the Y-Axis PEMI response with 20 frames averaged together. The second plot shows the same 20 traces with noise cancellation applied prior to averaging. Noise cancellation clearly reduces the signal variation between 0.013 and 0.025 seconds which may lead to a better time constant estimate.

Figure 51: Noise Cancellation With Target at Site C

5.   Conclusions

The objective of this program has been to evaluate the PEMI method in the context of the UXO detection and classification problem. The program included several phases of modeling, hardware development, field work,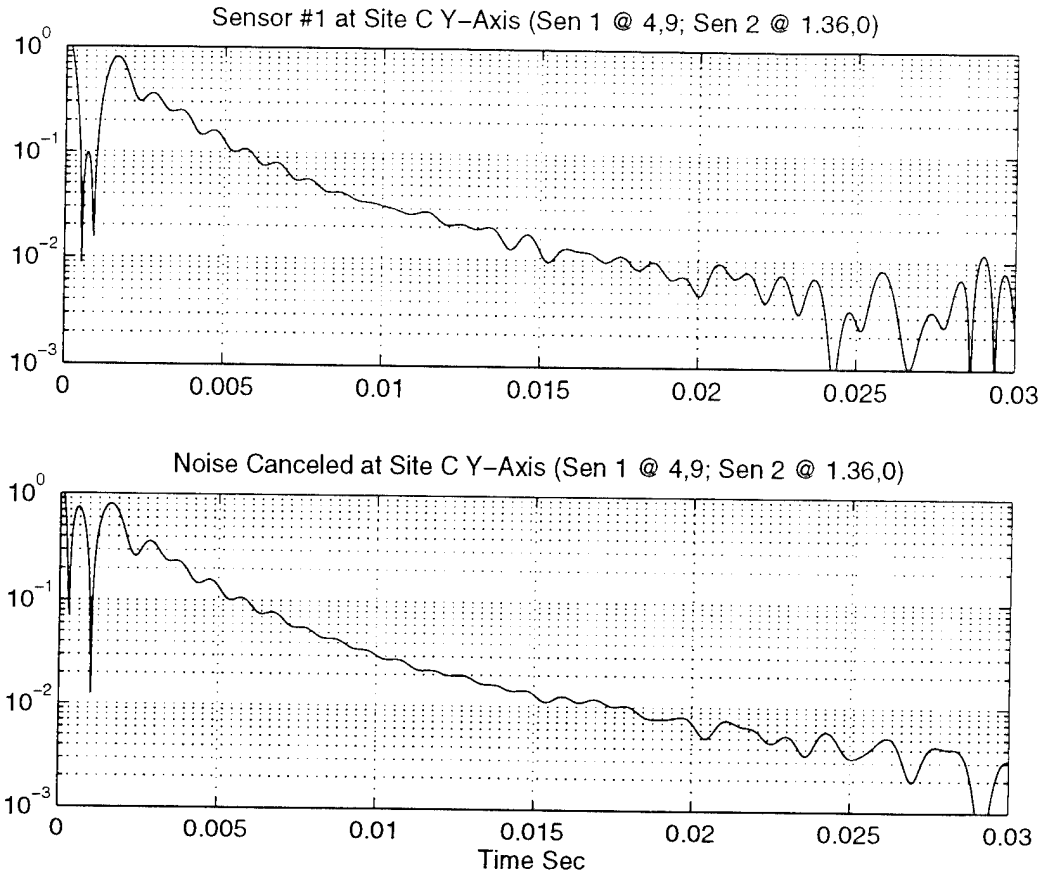 and data processing. In general, the results of the program indicate that PEMI is a very promising method for UXO remediation, particularly regarding target classification.

The PEMI method is an active electromagnetic technique and requires a transmitter system, a receiver system, a positioning system, and signal processing to interpret the data. The method works by setting up a primary magnetic field and then abruptly shutting it off, thereby creating an electromagnetic pulse which induces currents in nearby conductors. The currents decay due to resistive losses, creating a secondary magnetic field which can be detected above the surface of the earth. The rate of decay of the secondary magnetic field contains information about the size and conductivity and magnetic permeability of the object, and can be used as a classification tool. The PEMI system operates at very low frequencies compared to radar, and thus does not detect changes in the earth's composition. However, the decay time constant is very useful in determining the size of a metallic object. The spatial character of the secondary field can be used to locate the target. This program has successfully applied this method to characterize UXO targets and to test electromagnetic models describing PEMI responses of simple shapes.

Several PEMI models have been developed as part of this program. The primary field model computes the excitation magnetic field given specific transmitter loop geometry. In this program all transmitters were implemented as multi-turn, ground-laid wire loops. The configuration served the purpose of the test, but fieldable systems could be far more portable. The primary field model (in conjunction with other models) can be used to design a different system configuration, including 3-axis transmitters.

The target response model and secondary field model are used to compute the received signal from the currents induced in a target whose location and size are known. In this program, UXO were modeled as a thin conductive ring. The data indicate that such a simple model is useful in parameterizing UXO responses for classification, though it is still too elementary to describe the response in full. Intermediate time responses may be even more helpful at classifying targets, and are also significantly stronger than the late time response. Furthermore, UXO have long aspect ratios and some (though apparently not much) information is lost when trying to parameterize real UXO with simple thin rings.

Data interpretation was performed by fitting a thin ring model response to measured data. Finding an optimal fit using the Damped Least Squares (DLS) algorithm was very effective and efficient in both temporal and spatial processing steps. It seems straightforward to implement such processing in a fieldable system. Accurate sensor position information is needed however, because of the highly localized target response.

A PEMI hardware system was configured to make basic measurements of responses from several real UXO. The system included a commercially available transmitter, designed for use

in geophysical applications. The commercial receiving coils that were supplied with the transmitter were not suitable for the UXO application since the scale of the problems is very different. UXO responses vary over distances which are very short compared to most geophysical features of interest. Therefore, two sets of 3-axis coils and receiver amplifiers were built for this program. The data was collected using an 8-channel Macintosh based data acquisition system. The data acquisition software was specifically designed for this program to permit in-field monitoring of data quality.

The data acquisition system developed for this test was flexible but was consequently rather complex to use. The constraint of using off-the-shelf equipment proved to be unfortunate in regard to the receiver coils because of the additional cost associated with testing the units, and then designing and building custom coils when the commercial ones were found to be unsuitable. The transmitter driver worked, but was not optimized for the problem either. The commercial system was designed to measure responses with more rapid decays (broader band) and was somewhat overdesigned for our application.

Noise reduction by simple signal processing proved adequate in the UXO context. A noise cancellation scheme using multiple receivers was studied and tested as part of this program. The analysis indicates that extremely high coherence between the noise measured by the UXO sensor and the noise detection sensor is required to achieve significant gains in signal to noise ratio. In this program, only 3 to 7 dB improvement was realized. Further enhancements in signal processing are no doubt possible, and implementing them as early as possible in the data collection stream is advisable. The best monitor of data quality is a signal that has been processed to give results that are easily interpreted by an operator.

The PEMI models were first validated in tests held in Mukilteo by comparing them with PEMI data from several aluminum and steel ring test targets. The models proved robust and sufficiently accurate to proceed with the UXO characterization. In particular, a brief study of coupling between two ring targets indicates that superposition of individually modeled responses is valid even when the rings are only 0.8 meter apart.

Three different UXO (80mm, 122mm, and 155mm shells) were used as targets and characterized using the thin ring model parameterization. The time constants for the UXO are 14ms, 29ms, and 30ms, respectively. The two large shells have very similar time constants and are not readily differentiable using time constant information alone. Spatial responses led to good determination of position and orientation: the tests indicate typical accuracy of better than 10 cm in depth, 5 cm in horizontal location, 5 degrees in tilt with respect to the vertical, and about 10 degrees in bearing.

A blind test was held on the "magnetometer test range" at the NAVEODTECHDIV base, in which three, 10 by 10 meter, sites were surveyed by magnetometer and PEMI sensors. Targets were detected and located in each site using both methods. The magnetometer proves to be an effective broad range survey tool. It is a mature field instrument. The preliminary survey of each site by the PEMI instrument was somewhat cumbersome, but reflects the experimental nature of the configuration. In particular, moving the transmitter coil was not very convenient, and leveling the receiver platform was a slow process. Both of these limitations could be greatly improved in a field system prototype development. On the other hand, very precise estimates of target location (and of course, of the time constants) were obtained from the detailed PEMI survey lines.

The results of the program confirm that the PEMI method is likely to be very useful in UXO remediation and has provided modeling tools that will make designing a fieldable prototype device possible. The successful application of PEMI to the UXO problem would nevertheless greatly benefit from further development and adaptation of the method, including enhancements to the signal processing, expansion of the UXO response database, as well as the development of specialized hardware.

This page is intentionally left blank

6. Recommendations

The initial evaluation of the PEMI method in the context of the UXO detection and classification problem is very encouraging. However, the program was very short, and each phase of the program could be extended and continued.

The thin ring model, though simple, does not include more than one time constant for the UXO. In particular, it cannot model the response of the UXO when the primary field lines are in the plane of the model ring. A simple extension of the ring model would be to include a second ring perpendicular to the first, with possibly a different time constant. One could also imagine trying two rings aligned with the same axis but separated by some distance to help simulate the long aspect of the UXOs. Furthermore, including a shorter time constant would open up more of the signal to interpretation, in a time window where the signal is strong.

In this study, three UXO shapes were examined in detail. It would seem necessary to obtain a better statistical sample of the types that were studied, and to broaden the scope of the library in order to better understand how different the responses of various UXO can be. It is still not possible to accurately estimate UXO time constants given their dimensions, though a good first approximation can be made by extrapolating from the three UXO shapes that were examined. A simple model could be developed to estimate the response of a new shape.

The data processing can be improved at many levels. Fitting a more complicated target model will require fine tuning the inversion scheme. Reducing the noise from power lines can still be improved, as can the noise from random sources by rejecting outliers before they bias the average. Providing the operator with a better data display will help speed up data acquisition.

Finally, designing a prototype instrument specifically for the UXO application would result in far better data acquisition performance and would also tune the sensitivity of the PEMI method to the types of UXO targets that are of interest. The models in hand would permit the design of a prototype instrument. Other configurations such as gradiometer arrays could also be evaluated and may have advantages for the PEMI method much as they do for the magnetometer. A battery operated unit would be far lower noise than one relying on a generator like the system used in this program.

The results of the program confirm that the PEMI method is likely to be very useful in UXO remediation and has provided and validated modeling tools that will make designing a fieldable prototype device possible. The successful application of PEMI to the UXO problem would nevertheless greatly benefit from further development and adaptation of the method, including enhancements to the signal processing, expansion of the UXO response database, as well as the development of specialized hardware.

7. Appendix A: Noise Cancellation and Analysis

Memorandum

Alliant Techsystems Inc.
6500 Harbour Heights Parkway
Mukilteo, WA 98275-4844

Date: June 15, 1994

From: W. P. Harthill

Subject: Noise Cancellation for PEMI

Organization: MS

HED: WA34

To: J. Bamert 4E13-WA34
J. Calhoun 4D17-WA34
R. McGough 4E06-WA34
D. Hutchins 4E13-WA34
J. Gaevert 4E13-WA34

MS: 4E13

Telephone: (206)-356-3085

References: *ATK Internal Technical Memos:*

"SNR Predictions For PEMI", W.P. Harthill Dated February 28, 94
"PEMI Performance Revisited", W.P. Harthill Dated June 9, 94

The analysis presented in the reference memos shows that the ambient magnetic noise expected is sufficiently large to render analysis of the PEMI signals impossible without other measures. For magnetic induction sensors it is common to incorporate noise cancellation which appears to work well in a great number of cases. This work was performed to determine the salient problems and the sensitive PEMI system design areas.

The analysis indicates that it is highly likely that the required noise cancellation of from 40 to 50 dB is realizable perhaps with only one auxiliary sensor located approximately 150 meters from the PEMI sensor. This conclusion is based upon an assumed isotropic magnetic noise distribution.

Figure 1 shows a block diagram for the signal processing operations in the canceler. The correlation matrices are small and the bandwidth less than or equal to 1 KHz. Thus, the signal processing load is low.

W. P. Harthill

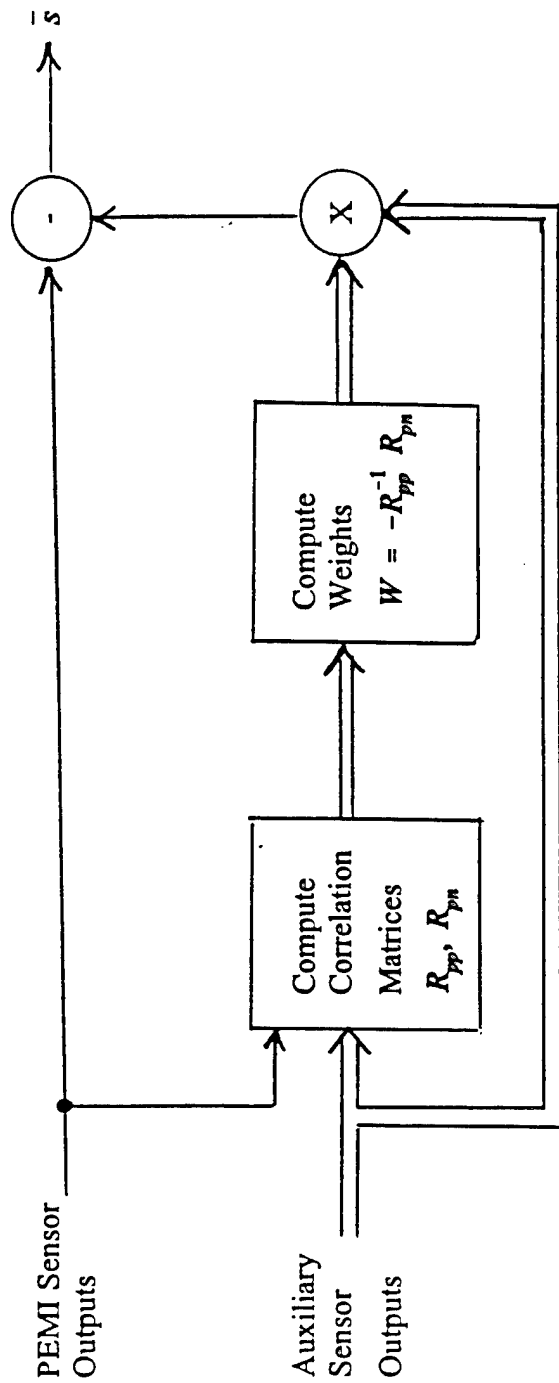**Figure 1**
Noise Canceler Block Diagram

PEMI Sensor
Outputs

Auxiliary
Sensor
Outputs

Compute
Correlation
Matrices
R_{pp}, R_{pn}

Compute
Weights
$W = -R_{pp}^{-1} R_{pn}$

$\bar{s}$

Analysis Of A PEMI Noise Canceler

The purpose of this analysis is to gain some understanding of the ability to cancel, and thereby reduce, the noise level seen by PEMI. The previous results presented in the reference memos indicate that from 40 to 50 dB of noise cancellation will be required to allow analysis of the pulse echo exponentials. In this memo a set of assumptions will be made to assess the feasibility of this degree of cancellation. As a second calibration point Julie Gaevert indicates that her contact, Dan Dubble at APL Johns Hopkins, states that they (APL) regularly achieve 40 dB of cancellation.

In this analysis we shall assume that our sensor suite includes the PEMI sensor with which a steady state magnetic field is established and then allowed to collapse suddenly after which the PEMI receiver analyzes the vestigial magnetic fields due to conducting objects in the proximity of the PEMI sensor (0 - 10 meters). It is during this time that the ambient magnetic background field interferes with the PEMI detection process.

It is common knowledge that the ambient magnetic field of the earth is highly correlated from one location to another (up to several hundred meters) at low frequencies (less than 1000 Hz). This is not surprising because the wavelength at 1000 Hz is 300,000 meters in air.

The correlation of noise between the PEMI sensor and a set of auxiliary sensors located out of PEMI range (perhaps 100 -300 meters separation) allows separate measurements of the ambient field that can be weighted and subtracted from the PEMI receiver output to reduce the effective noise level.

This analysis is started by assuming that the PEMI sensor observes the signal r and that p represents a set of observations made by n auxiliary sensors. It is assumed that the auxiliary sensors are sufficiently removed from the PEMI sensor that they are not affected by the PEMI signal. For this case we have:

$$r = s + n_o$$

$$p = \begin{pmatrix} n_1 \\ n_2 \\ n_3 \\ | \\ | \\ n_N \end{pmatrix} \qquad (1)$$

where: s is the signal and is not correlated with the noise and
      p is correlated with n_o

The problem is formulated as an estimation problem where we estimate s by forming:
where w is a weight vector to be determined by minimizing the error:

$$\bar{s} = r + w^t p \tag{2}$$

$$\Gamma = E[(\bar{s} - s)^2] \tag{3}$$

with respect to w. This is done by noting:

$$\Gamma = E[(r + w^t p - s)(r + w^t p - s)^t]$$

$$\Gamma = E[(n_o + w^t p)(n_o + w^t p)^t]$$

$$\Gamma = E[n_o n_o^t + w^t p n_o^t + n_o p^t w + w^t p p^t w] \tag{4}$$

$$\Gamma = R_{nn} + w^t R_{pn} + R_{pn}^t W + w^t R_{pp} w$$

Gamma in Equation 4 is minimized with respect to w when w is:

$$w = -R_{pp}^{-1} R_{pn} \tag{5}$$

When this weight is used in the error Γ:

$$\Gamma_{min} = R_{nn} - R_{pn}^t R_{pp}^{-1} R_{pn} \tag{6}$$

Where R_{pn} is the correlation vector between the PEMI observation and the auxiliary sensor observations and R_{pp} is the correlation matrix for the auxiliary observations. Note that the errorΓ without the noise cancellation process is simply R_{nn} and that the error is in reality simply the additive noise to s in the observed process r. With the noise cancellation process the error or effective observation noise, is reduced by the second term in Equation 6. It is useful for this analysis to define the reduction in noise level as a ratio in dB of the noise level before the application of cancellation to that after.

$$\Delta = 10 \log_{10}\left[\frac{R_{nn}}{\Gamma_{min}}\right]$$

$$\Delta = -10\log_{10}\left[1 - \frac{R_{pn}^t R_{pp}^{-1} R_{pn}}{R_{nn}}\right] \tag{7}$$

We will next examine the implications of the result in Equation 7.

One Auxiliary Sensor Case

When there is only one auxiliary sensor n=1 and we may write Equation 7 as:

$$\Delta = -10\log_{10}\left[1 - \frac{R_{pn}^2}{R_{pp} R_{nn}}\right] \qquad (8)$$

The last ratio in Equation 8 is recognized as the square of the correlation coefficient between the PEMI sensor and the auxiliary sensor so that:

$$\Delta = -10\log_{10}\left[1 - \rho_{pn}^2\right] \qquad (9)$$

For the single auxiliary sensor this equation tells us that the correlation coefficient must be at least that value given in the table below to achieve the SNR reduction shown.

SNR Reduction dB	Correlation Coefficient
10	0.95
20	0.995
30	0.9995
40	0.99995
50	0.999995

Table 1
Required Correlation Between PEMI and Auxiliary Sensors

This level of correlation seems high but before we reject it let us consider a first cut correlation model for ambient magnetic noise.

We don't have a magnetic noise model that is recognized as most appropriate. Therefore we shall take a first cut using the isotropic model used in acoustics for the same situation. For a single frequency the noise power spectral density for isotropic noise is simply sin(Kd)/Kd where K is the wave number and d is the sensor separation. When the noise is broadband and white it is appropriate to integrate over all frequency to obtain the broadband correlation:

$$P_{broadband} = \frac{1}{B}\int_0^B \frac{\sin(Kd)}{Kd}df$$

$$= \frac{Si\left(\frac{2\pi Bd}{c}\right)}{\left(\frac{2\pi Bd}{c}\right)}$$

(10)

where: Si() is the sine integral. A good approximation to the sine integral of x over x is given by:

$$\frac{Si(x)}{x} \approx 1 - 0.0555555\, x^2$$

(11)

for x less than .01. Figure 2 shows the error in the approximation. As an example, if we choose c, the speed of propagation in the mixture of earth and air at 1×10^8 meters per second, the bandwidth at B=1000 Hz, and the separation d = 100 meters the argument of the Si(x)/x function in Equation 10 becomes .0063. When the approximation for Si(x)/x is used a correlation coefficient for the 1 auxiliary sensor case becomes: ρ = 0.9999978. Therefore, it may be realistic to expect noise field correlations sufficiently high to yield 40 - 5- dB of cancellation. Physically, the justification for these high correlations is the very long wavelength in air, the medium carrying most of the background noise signal.

Multiple Auxiliary Sensors

For the multiple sensor analysis it was assumed that the auxiliary sensors were located by a random number generator. Two Monte Carlo cases were considered. The first case considered randomly located auxiliary sensors between radii of 75 to 225 meters with angles uniformly distributed in [0:2π]. The PEMI sensor and source are located at the origin. The 20 Monte Carlo runs were performed for a number of auxiliary sensors from 1 to 6. Each of Figures 3 to 5 show the composite auxiliary sensor locations over the 20 runs (20 for 1 auxiliary sensor, 40 for two, etc.) and a graph of "Degree of Noise Cancellation" representing the dB ratio of the noise without cancellation to that with cancellation as a function of bandwidth for 20 runs.

Figures 3, 4, and 5 show a general improvement in cancellation as the number of auxiliary sensors increases. The spread in cancellation performance over the runs is due primarily to the randomness in the auxiliary sensor locations. These results are encouraging considering the 40 - 50 dB of cancellation needed. It appears that with only one sensor that 45 to 50 dB of cancellation can usually be achieved.

Figures 6, 7, and 8 show a corresponding Monte Carlo treatment of the case where an attempt is made to place the auxiliary sensors symmetrically around the PEMI sensor. The sensors were placed at mean range of 150 meters at angles equal to 2π/n, where n is the number of auxiliary sensors. These mean positions were randomly perturbed by a Gaussian random variable having a

standard deviation of 15 meters in range and 0.1 radians in angle. This situation was supposed to represent actual operation where an attempt was made to place the auxiliary sensors symmetrically about the PEMI sensor but the locations are not exact either due to PEMI movement of because they were not accurately placed initially. Figures 6, 7, and 8, as in 3, 4, and 5, show the composite auxiliary sensor locations as well as the cancellation performance. The attempt to surround the PEMI sensor with auxiliary sources does little to improve the cancellation performance on the average. It does reduce the spread in performance on individual tries. As with the random sensor locations performance tends to increase with number of auxiliary sensors. The payoff in attempting to symmetrically locate them is of questionable value.

The canceler weights involve computing a square matrix inverse whose size equals the number of auxiliary sensors. This matrix becomes ill conditioned for low frequencies (long wavelength) and as the number of auxiliary sensors increases. Figures 9 through 14 correspond one-to-one with Figures 3 through 8 and show the distribution of singular values of the correlation matrix R_{pp} as a function of bandwidth. For more than 2 to 3 auxiliary sensors the spread of the matrix singular values (greater than 10^9 indicates that special attention will have to be paid to the inversion process to maintain stability in the results.

IMPLEMENTATION OF THE CANCELER

The application of this noise cancellation approach assumes that data is gathered from the auxiliary and PEMI sensors at times when the source signal is not present or is too small to affect the result. The correlation matrices R_{pp} and R_{pn} are computed periodically, perhaps iteratively, and from them the cancellation weights are computed. A tradeoff between computation rate, variance in the correlation estimates, and ability to cancel noise in a dynamic varying scenario must be made. Since the matrix size and the bandwidth are both small no great processing load is anticipated.
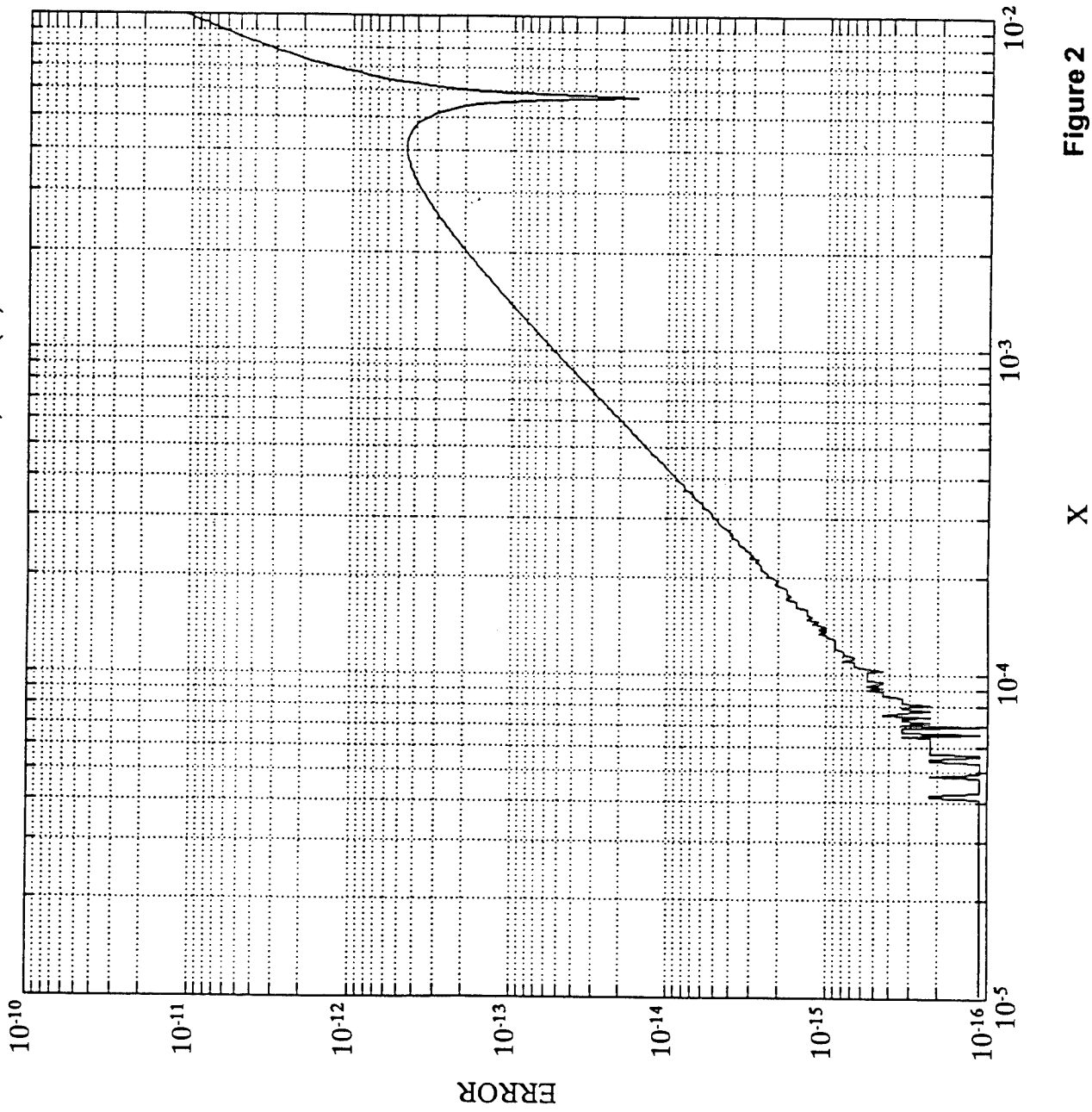
Error Between (1-.0555555*X^2) & SI(X)/X VS X
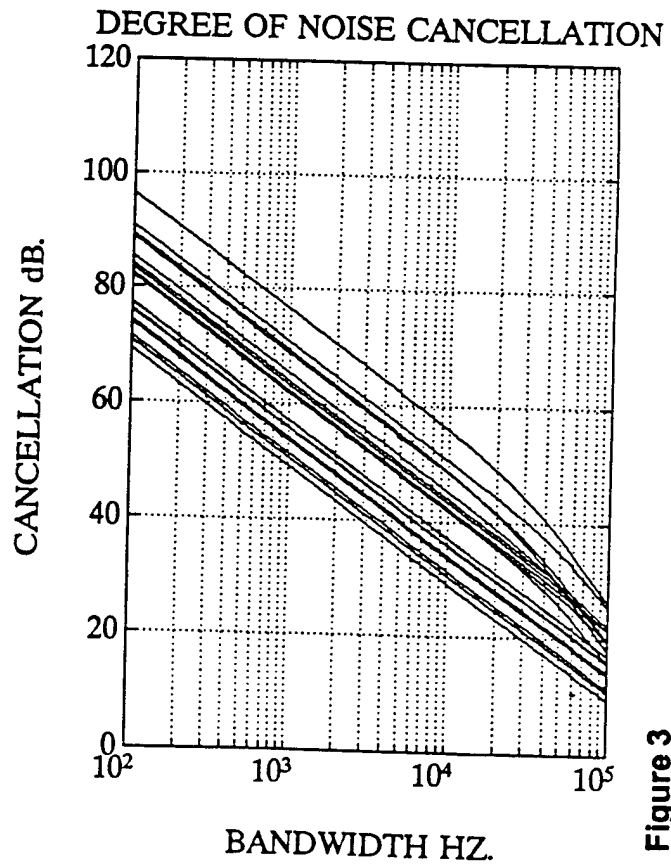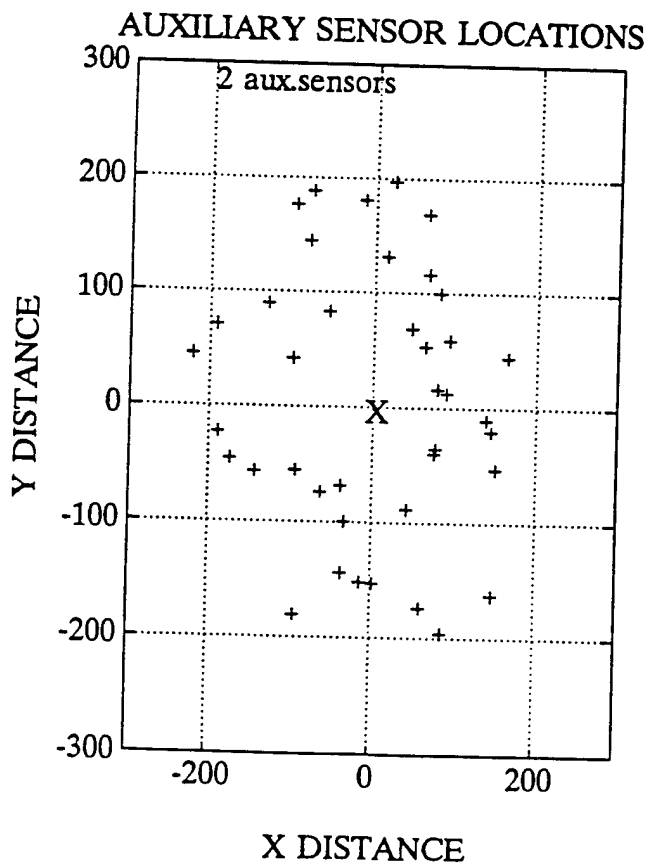
Figure 2
Error In Approximation
For Si(x)/x

A9
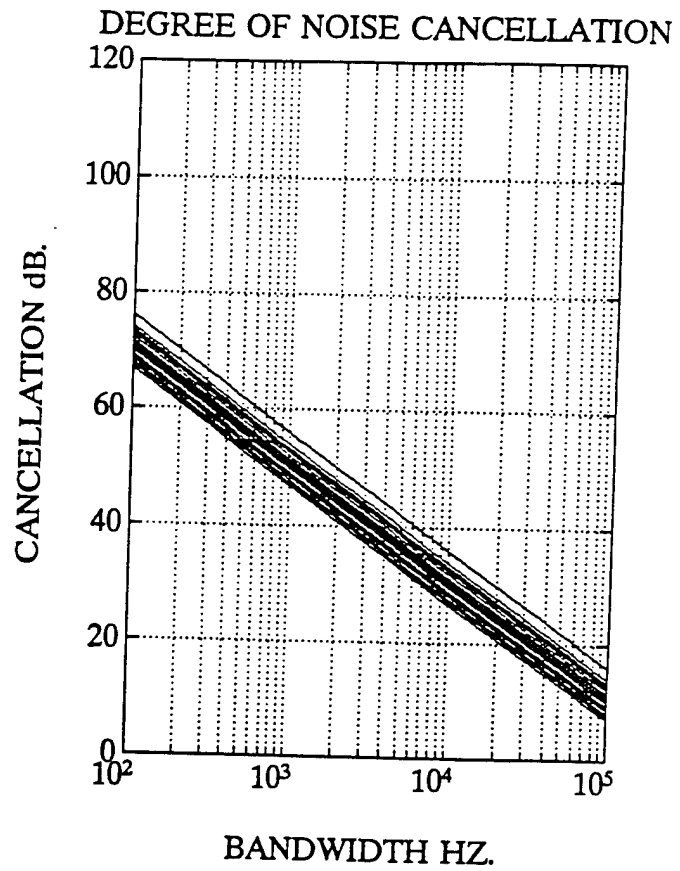
AUXILIARY SENSOR LOCATIONS

1 aux.sensors

X DISTANCE

Y DISTANCE

DEGREE OF NOISE CANCELLATION

CANCELLATION dB.

BANDWIDTH HZ.

AUXILIARY SENSOR LOCATIONS

2 aux.sensors

X DISTANCE

Y DISTANCE

DEGREE OF NOISE CANCELLATION
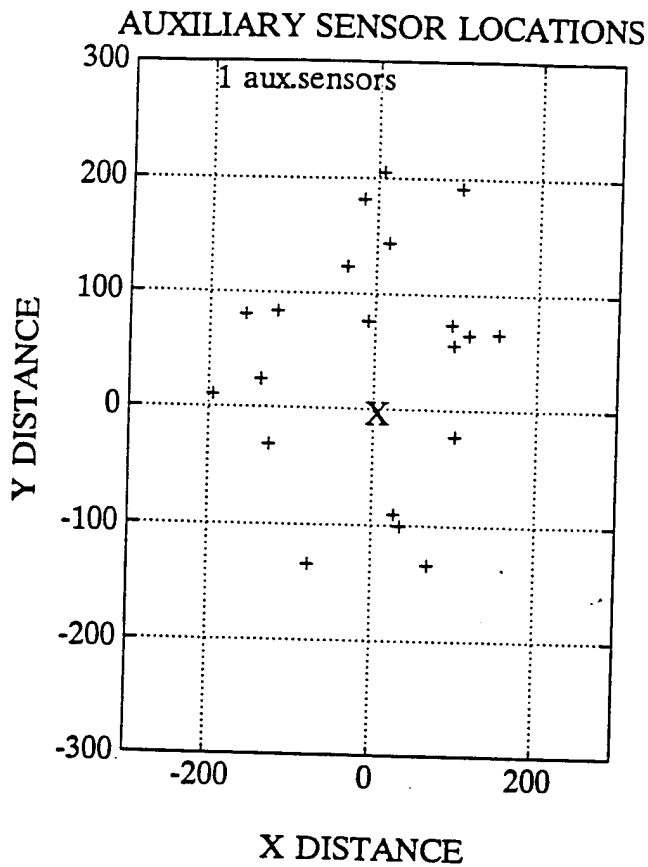
CANCELLATION dB.

BANDWIDTH HZ.

Figure 3
Degree Of Noise Cancellation For 20 Trials
& 1 and 2 Randomly Located Auxiliary Sensors

A 10

AUXILIARY SENSOR LOCATIONS

3 aux.sensors

DEGREE OF NOISE CANCELLATION

AUXILIARY SENSOR LOCATIONS

4 aux.sensors

DEGREE OF NOISE CANCELLATION

Figure 4
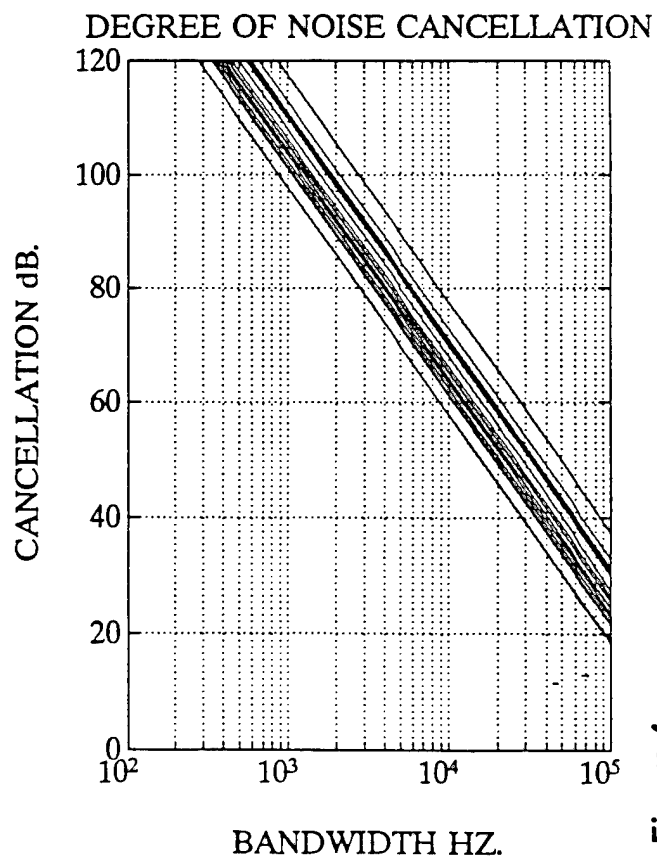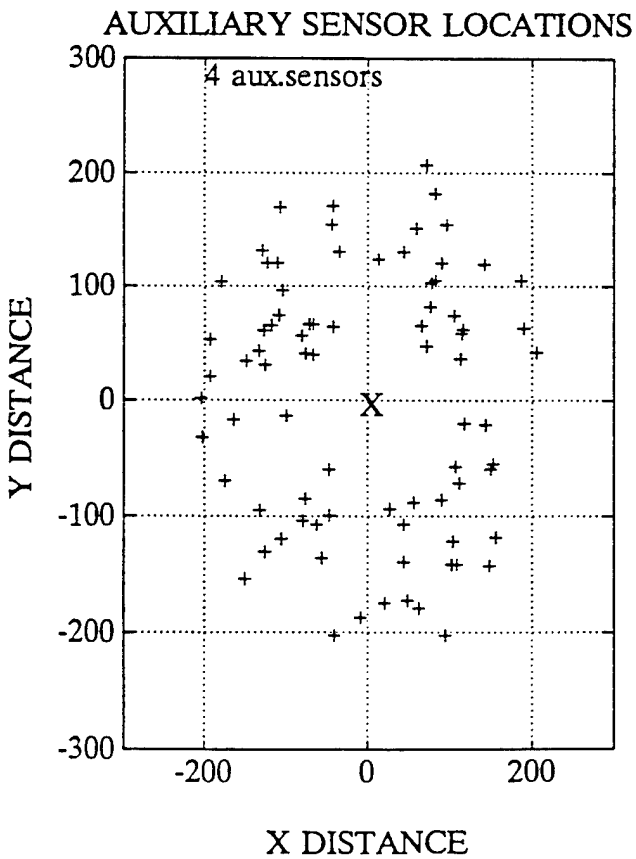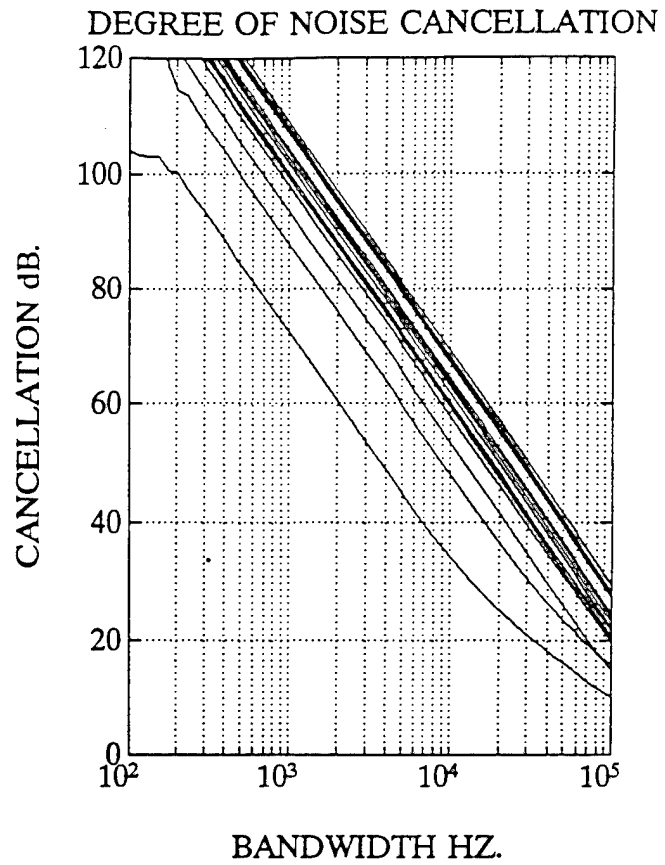**Degree Of Noise Cancellation For 20 Trials**
& 3 and 4 Randomly Located Auxiliary Sensors

AUXILIARY SENSOR LOCATIONS
(5 aux.sensors)

DEGREE OF NOISE CANCELLATION

AUXILIARY SENSOR LOCATIONS
(6 aux.sensors)

DEGREE OF NOISE CANCELLATION
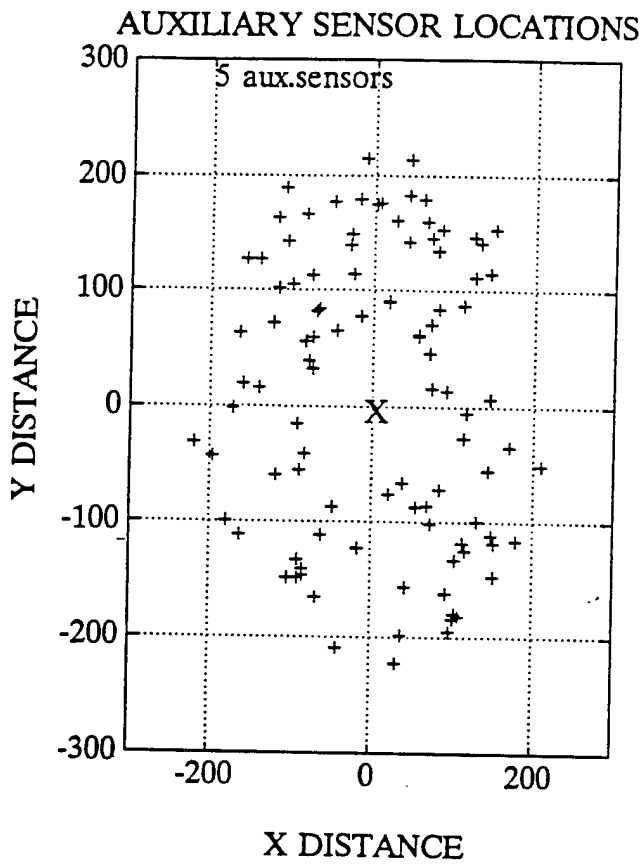
Figure 5
**Degree Of Noise Cancellation For 20 Trials
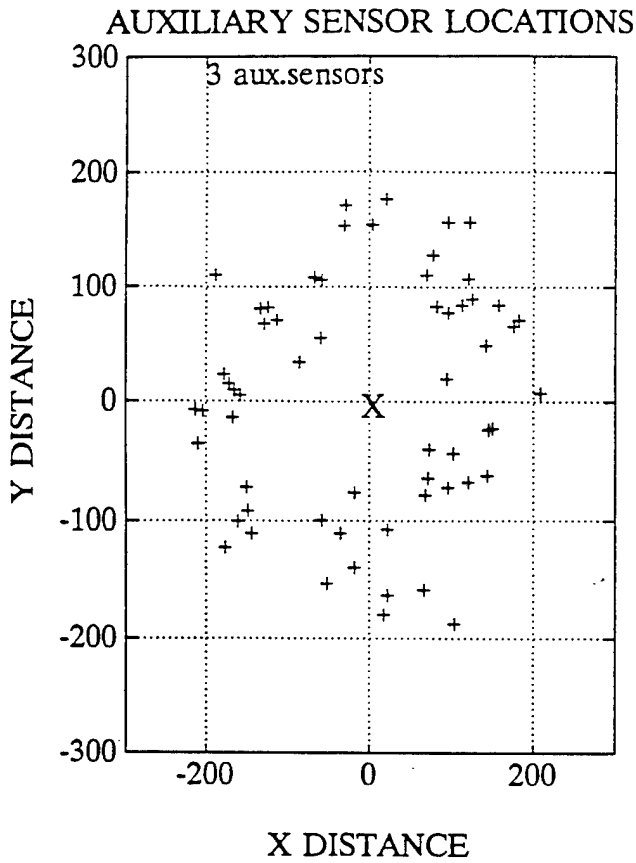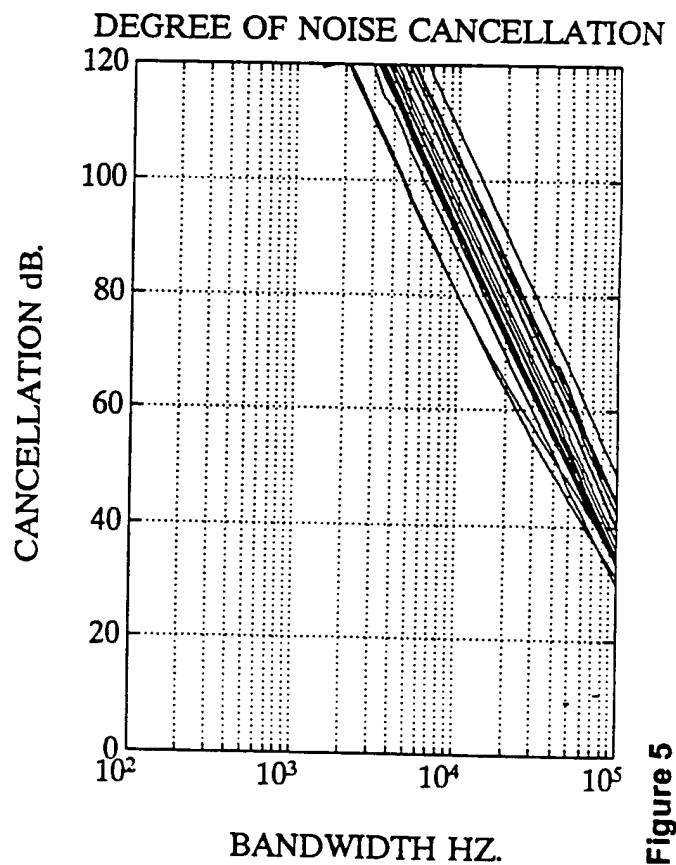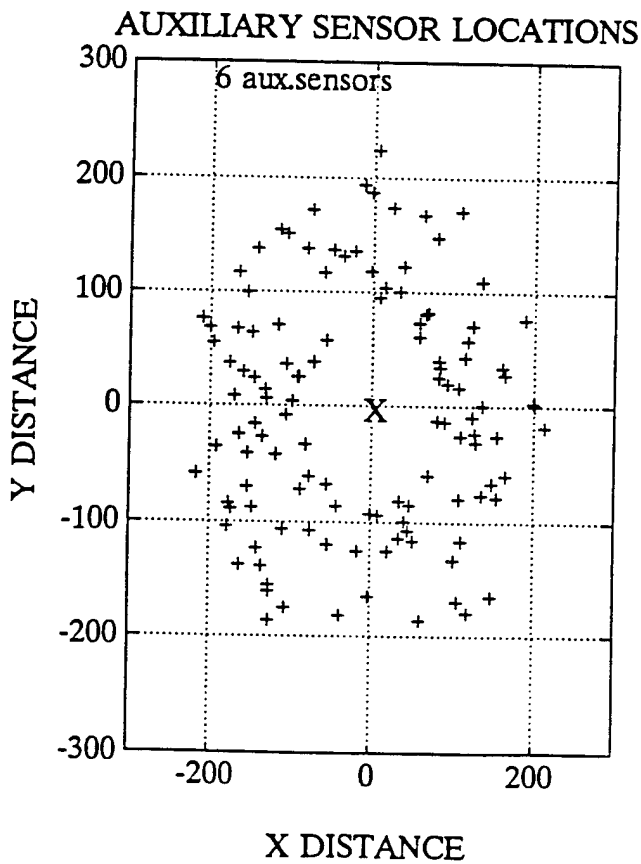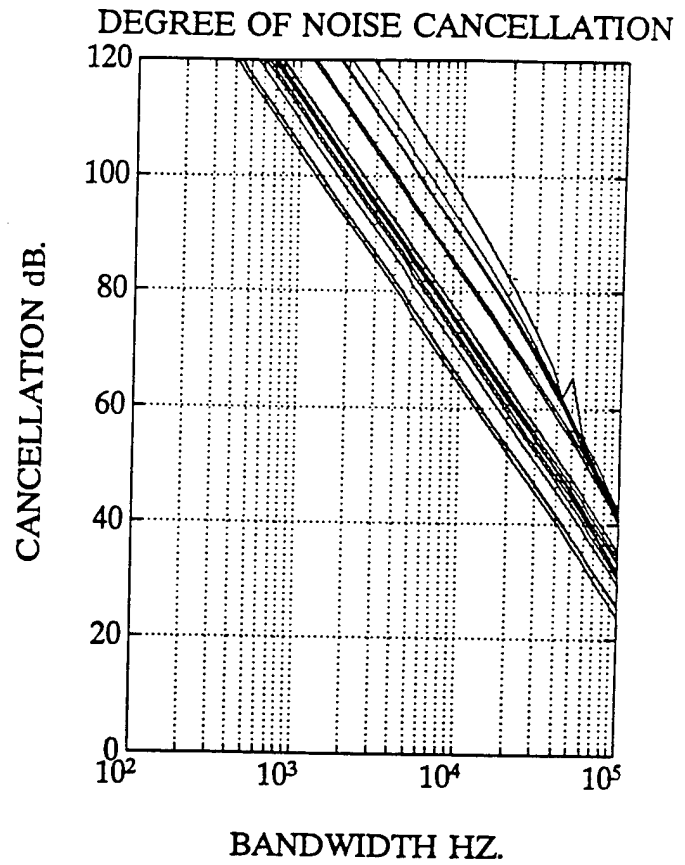& 5 and 6 Randomly Located Auxiliary Sensors**

Δ12

AUXILIARY SENSOR LOCATIONS

1 aux.sensors

DEGREE OF NOISE CANCELLATION

AUXILIARY SENSOR LOCATIONS

2 aux.sensors

DEGREE OF NOISE CANCELLATION

Figure 6
**Degree Of Noise Cancellation For 20 Trials
& 1 and 2 Quasi Uniformly Located Aux Sensors**

A 13

AUXILIARY SENSOR LOCATIONS

3 aux.sensors

DEGREE OF NOISE CANCELLATION

AUXILIARY SENSOR LOCATIONS

4 aux.sensors

DEGREE OF NOISE CANCELLATION
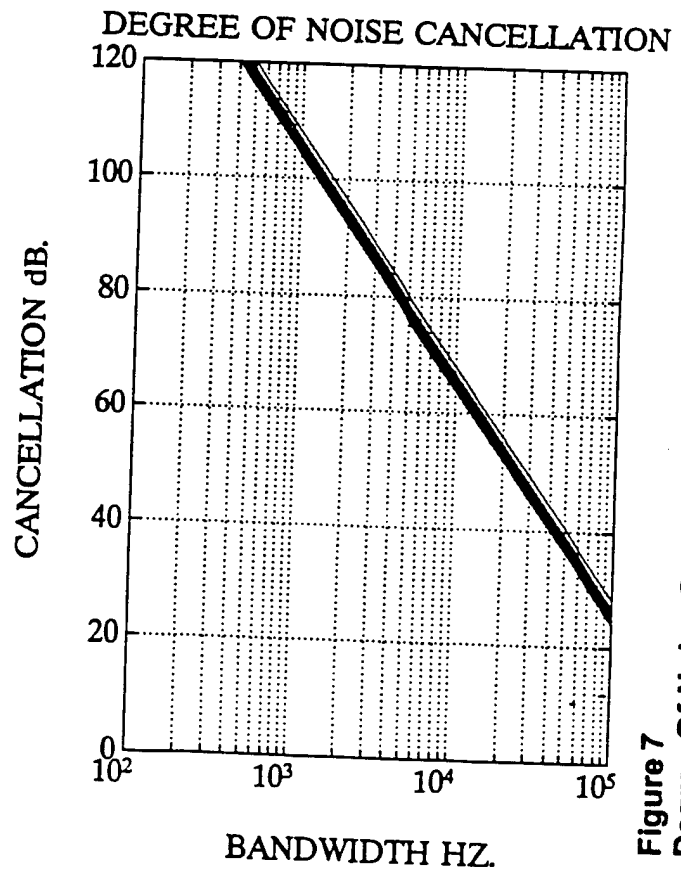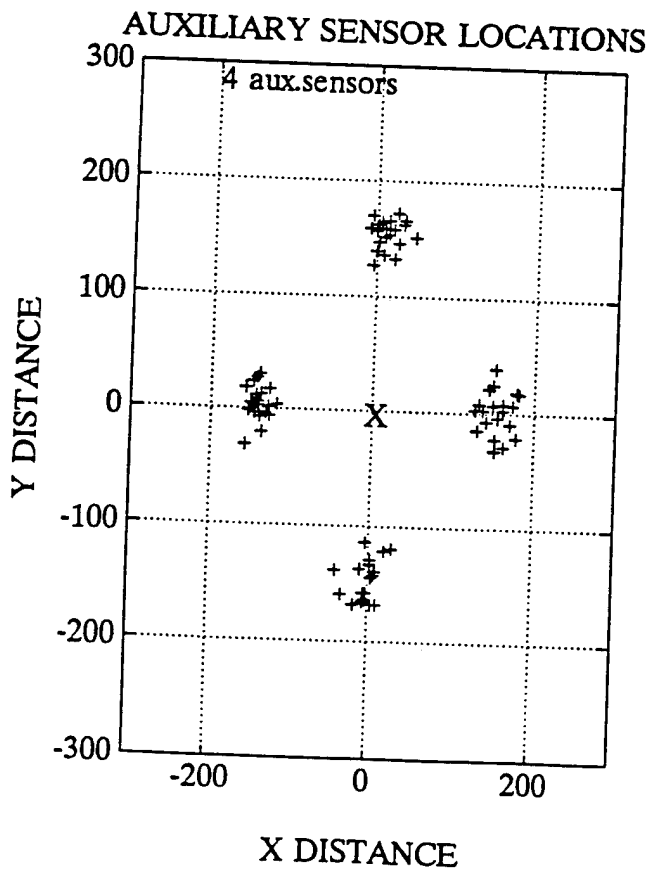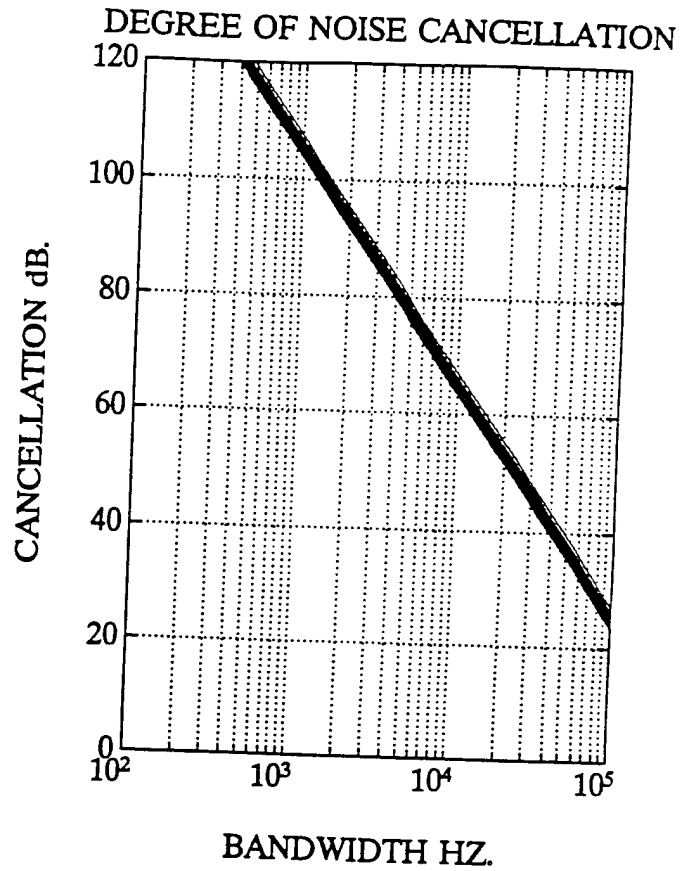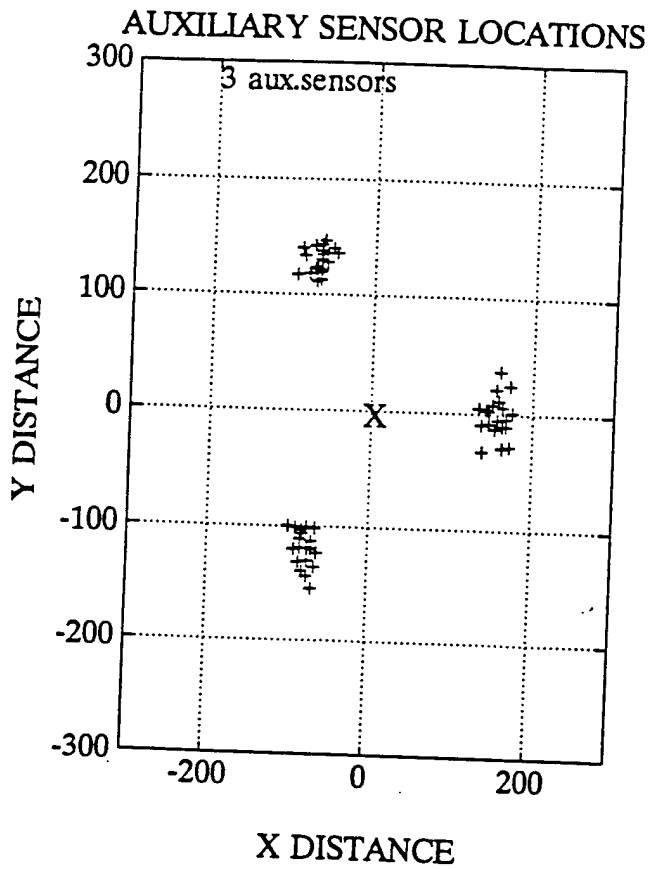
Figure 7
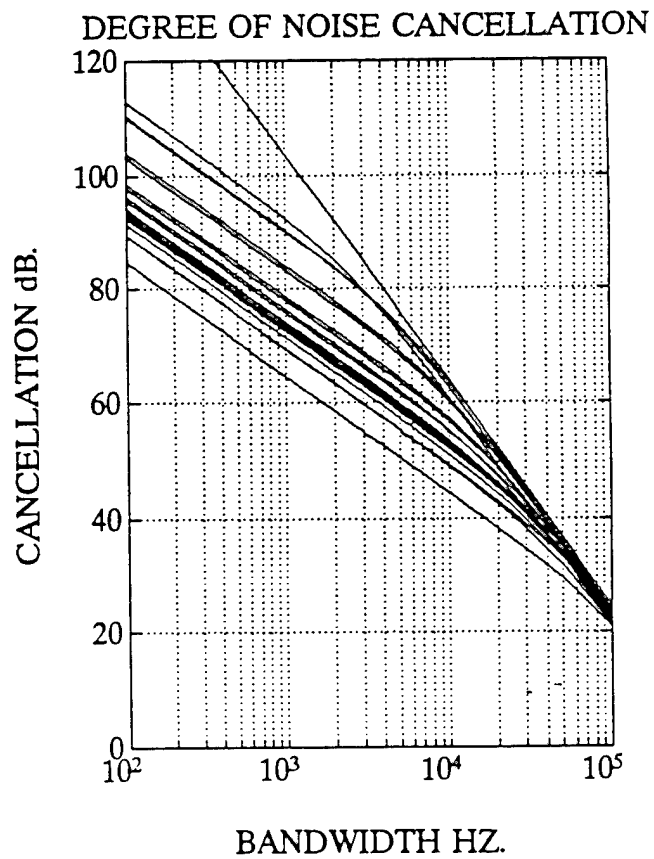**Degree Of Noise Cancellation For 20 Trials**
& 3 and 4 Quasi Uniformly Located Aux Sensors

A14

AUXILIARY SENSOR LOCATIONS

5 aux.sensors

DEGREE OF NOISE CANCELLATION

AUXILIARY SENSOR LOCATIONS

6 aux.sensors

DEGREE OF NOISE CANCELLATION
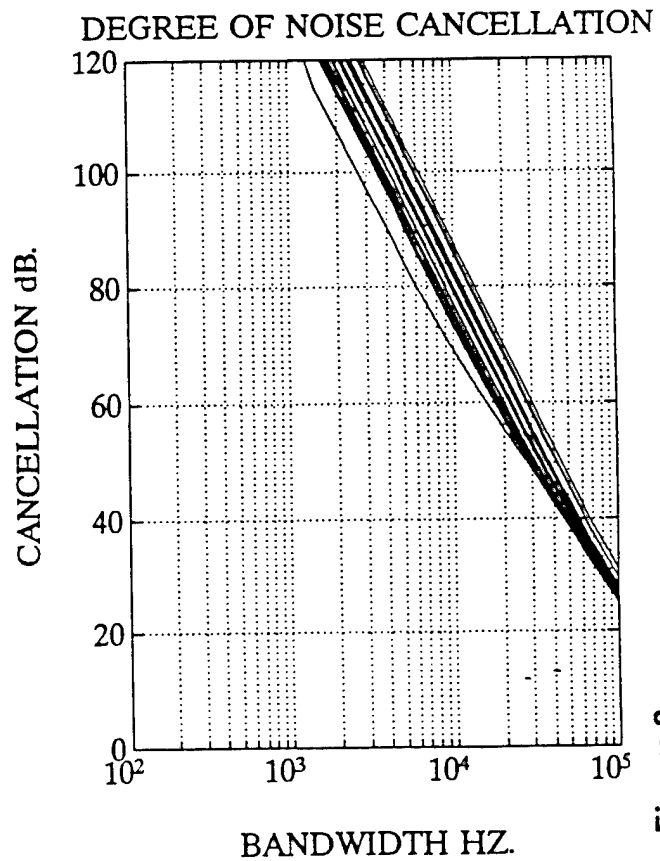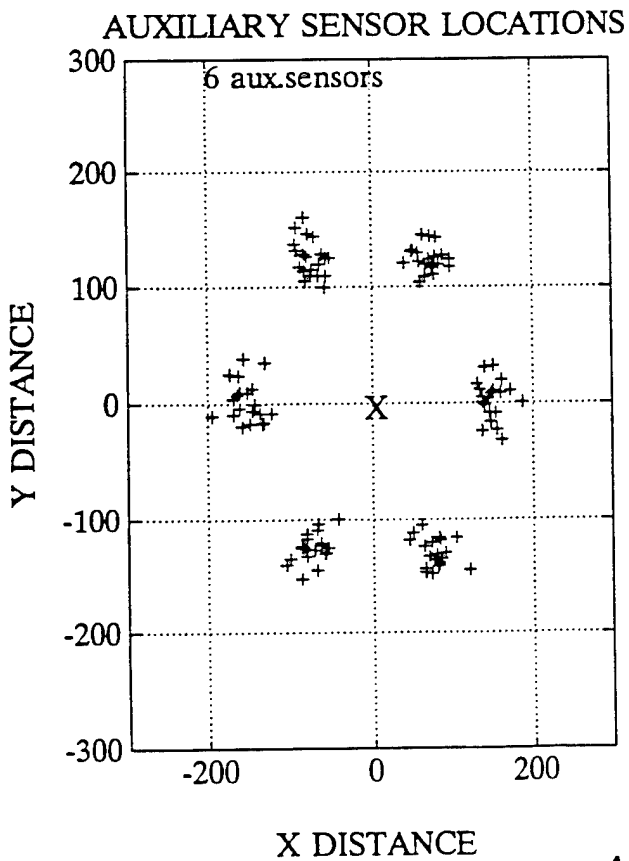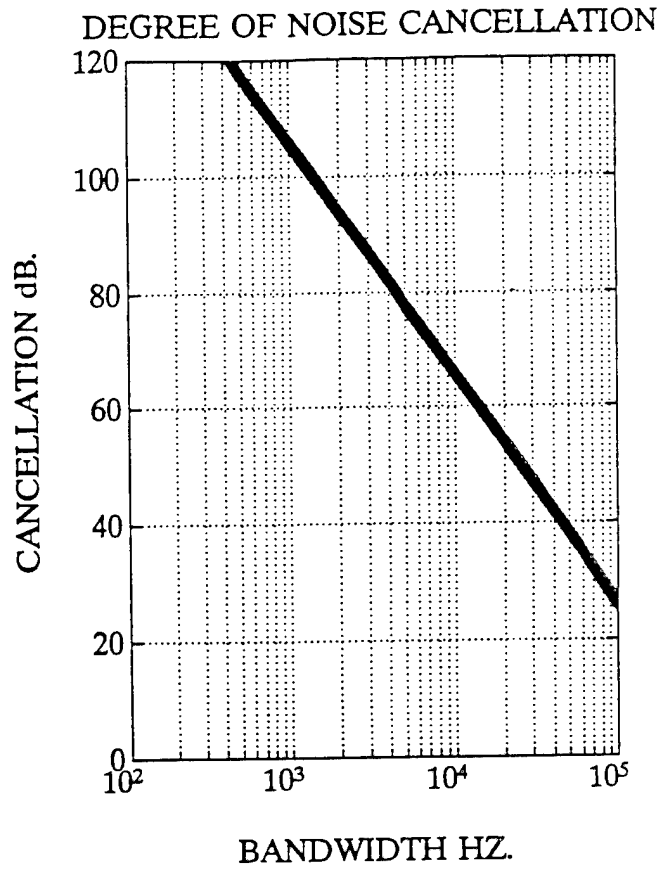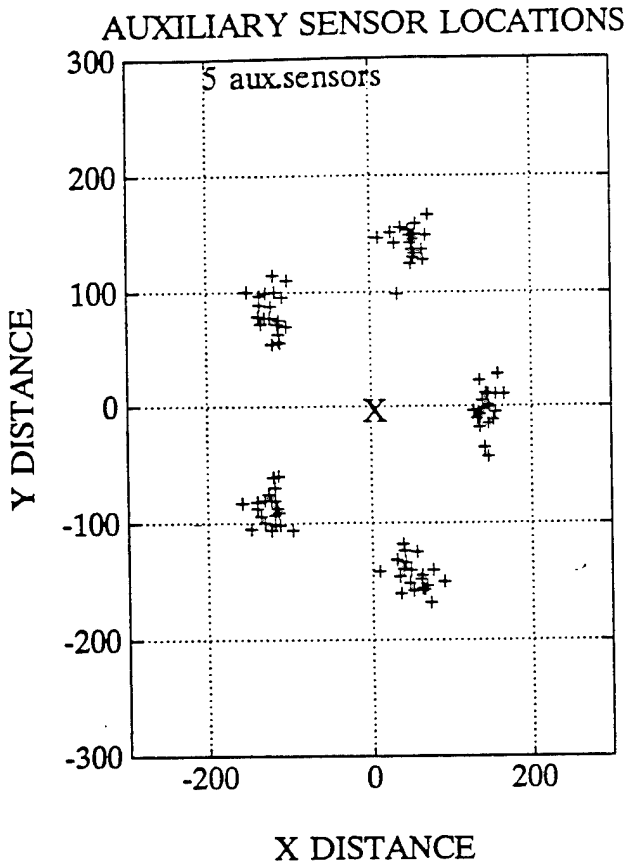
Figure 8
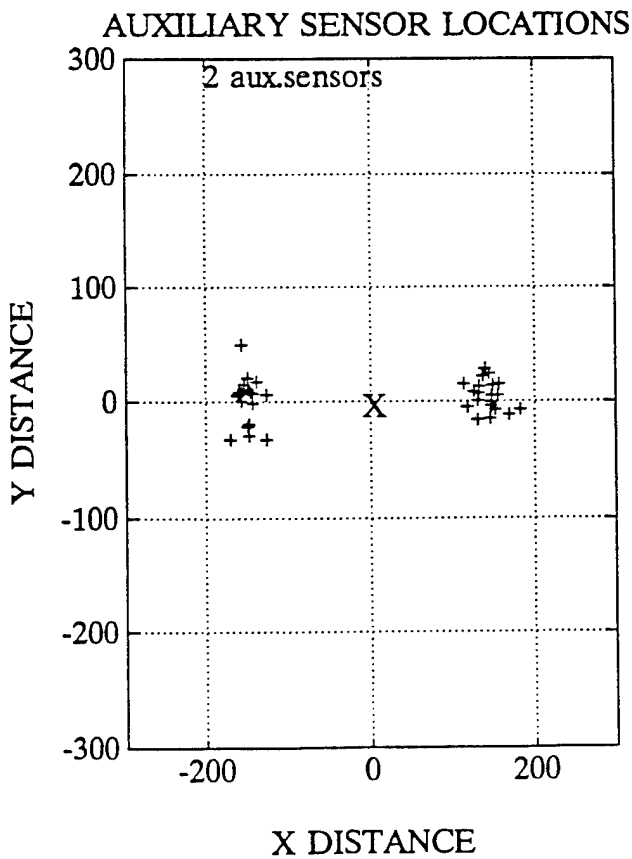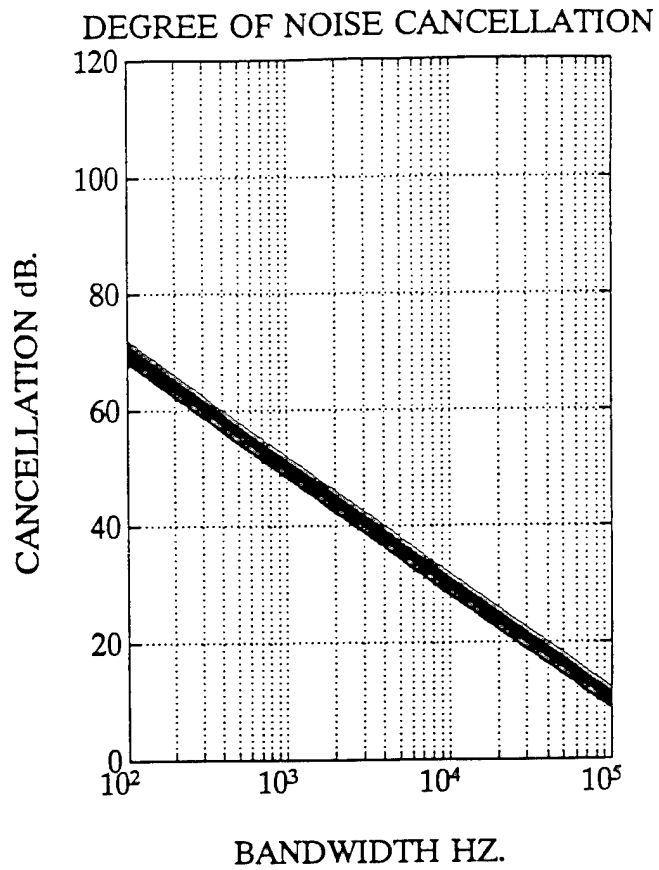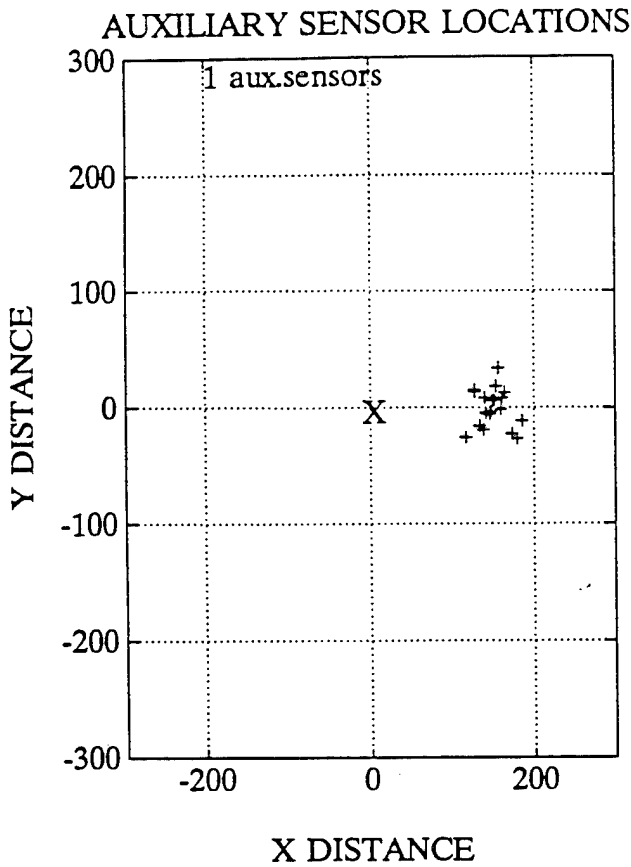**Degree Of Noise Cancellation For 20 Trials**
& 5 and 6 Quasi Uniformly Located Aux Sensors

A15

Singular Values for n = 1

BANDWIDTH INDEX
Index: 1 relates to 100 Hz
Index: 50 relates to 100 KHz

Singular Values for n = 2

BANDWIDTH INDEX
Index: 1 relates to 100 Hz

A16
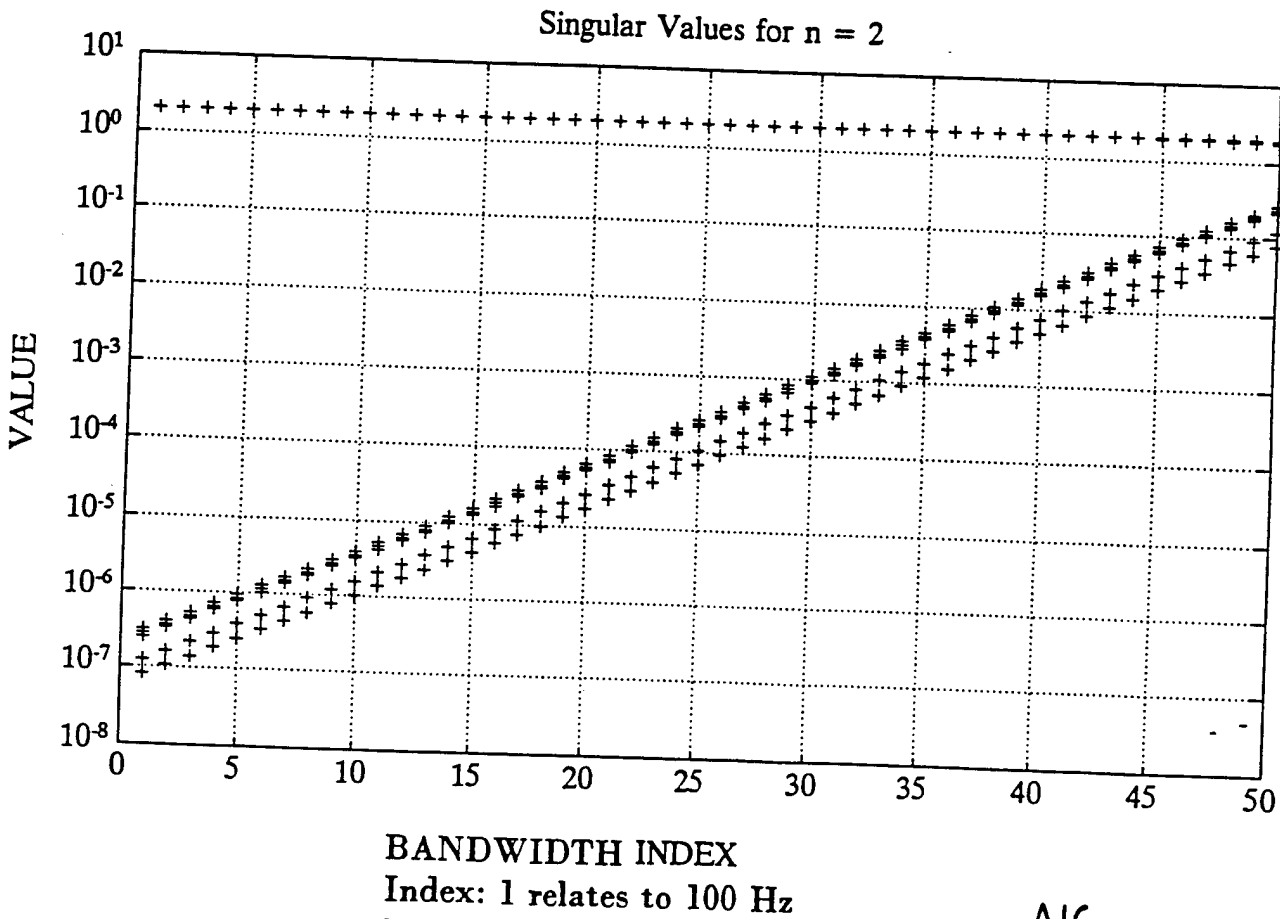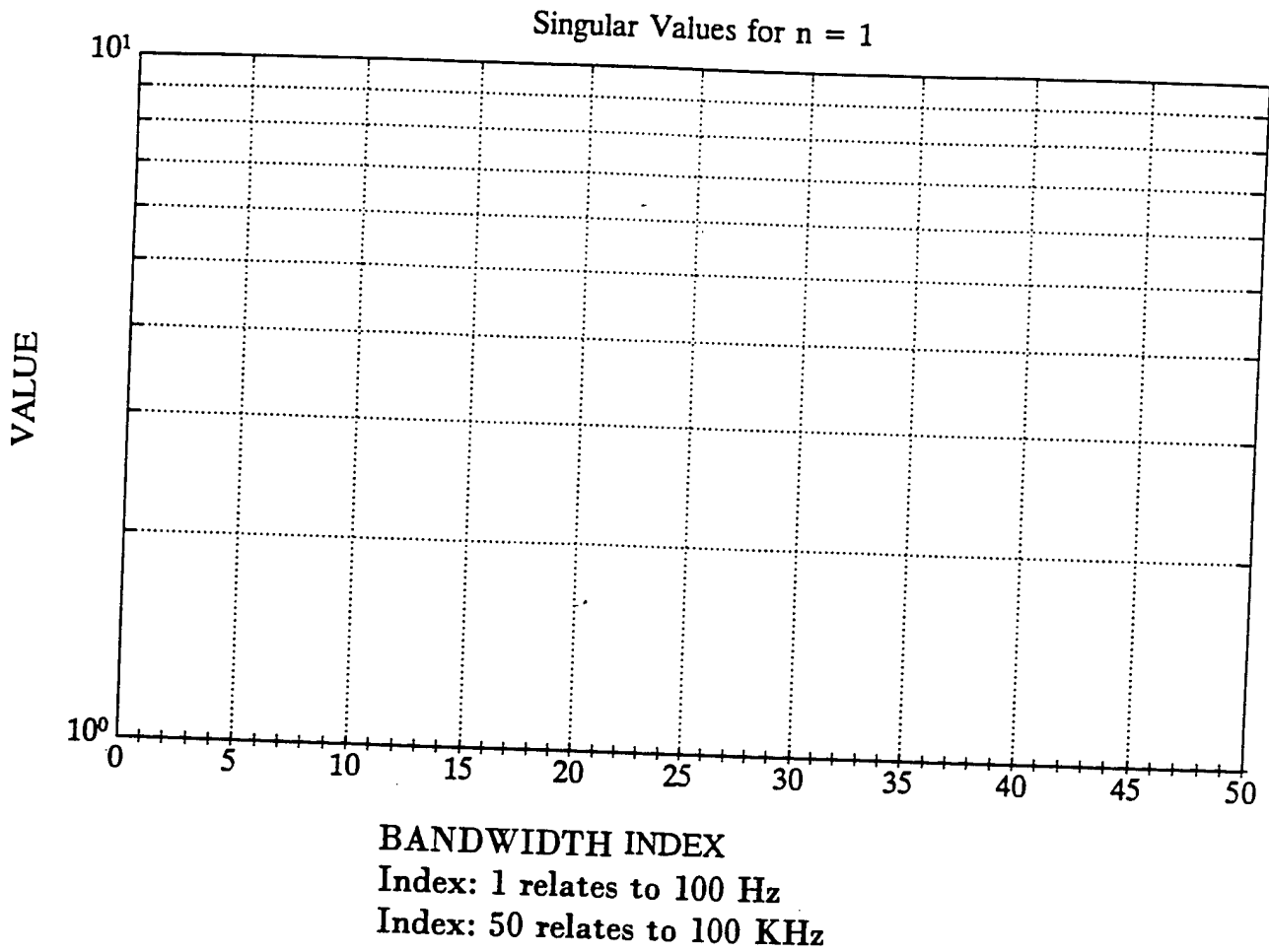
Figure 9
Singular Value Distribution For Rpp Correlation Matrix
For 1 and 2 Randomly Located Auxilliary Sensors

Singular Values for n = 3

VALUE

BANDWIDTH INDEX
Index: 1 relates to 100 Hz
Index: 50 relates to 100 KHz

Singular Values for n = 4

VALUE

BANDWIDTH INDEX
Index: 1 relates to 100 Hz

A17
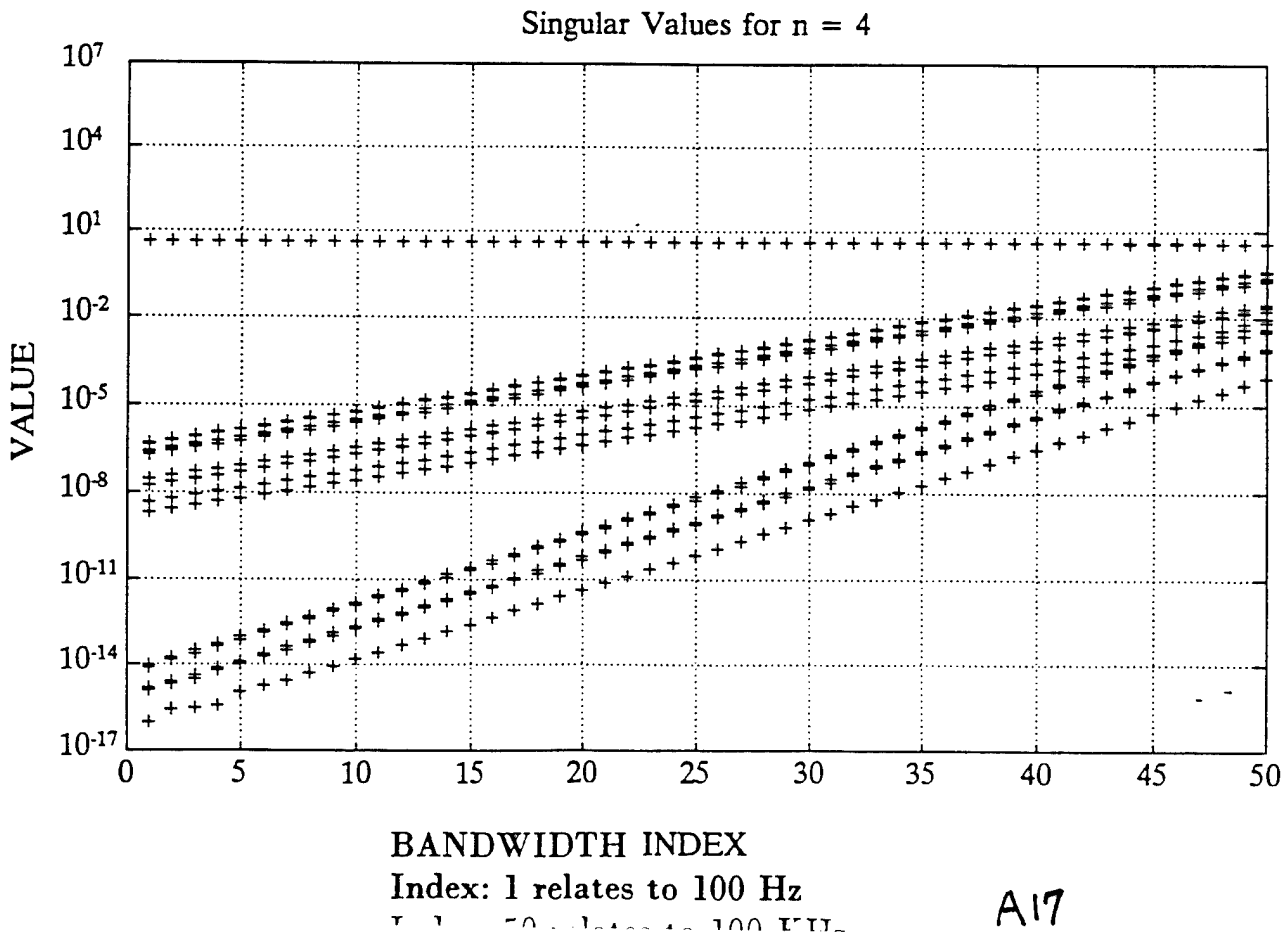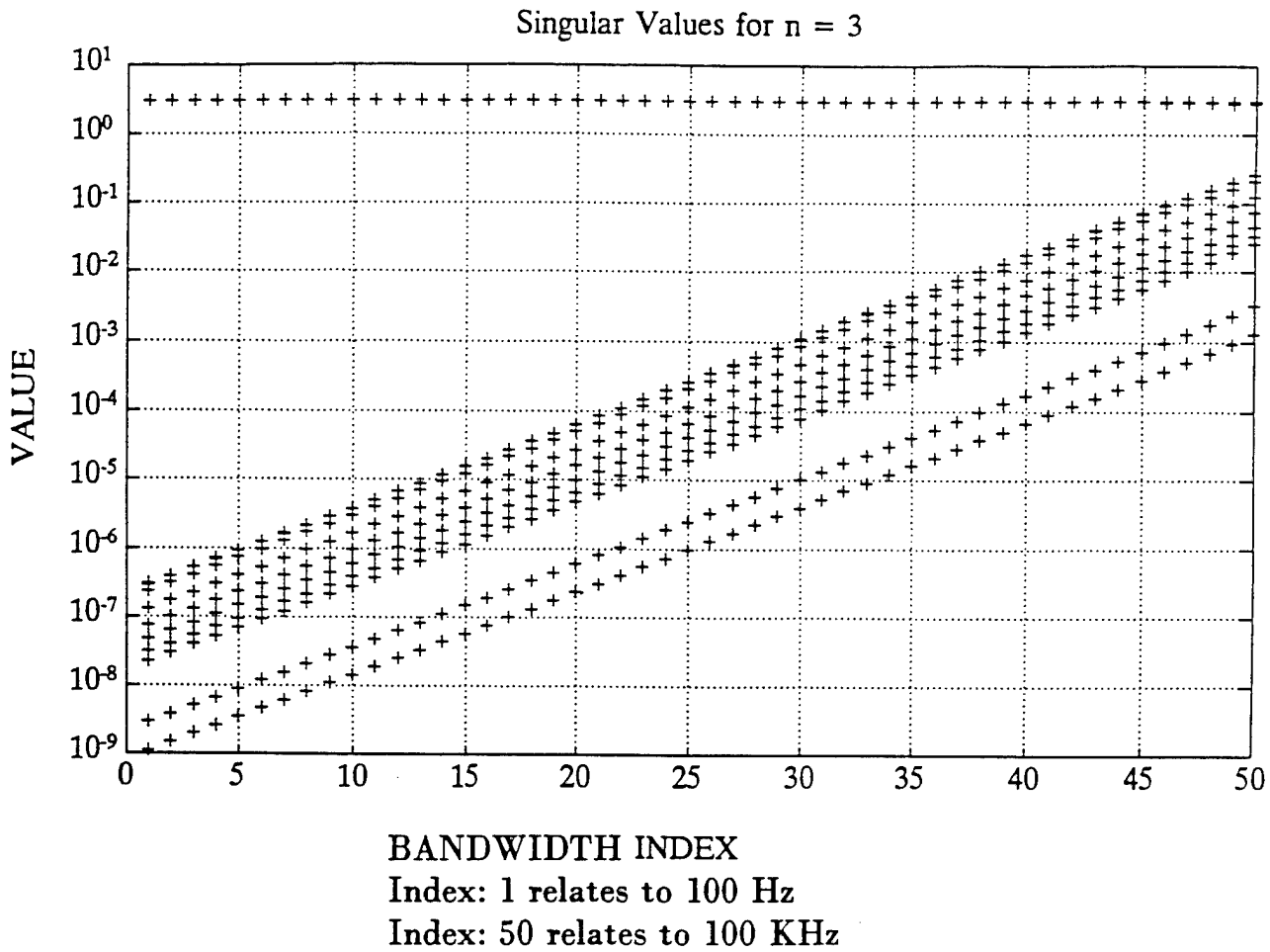
Figure 10
Singular Value Distribution For Rpp Correlation Matrix
For 3 and 4 Randomly Located Auxiliary Sensors

Singular Values for n = 5

BANDWIDTH INDEX
Index: 1 relates to 100 Hz
Index: 50 relates to 100 KHz

Singular Values for n = 6

BANDWIDTH INDEX
Index: 1 relates to 100 Hz
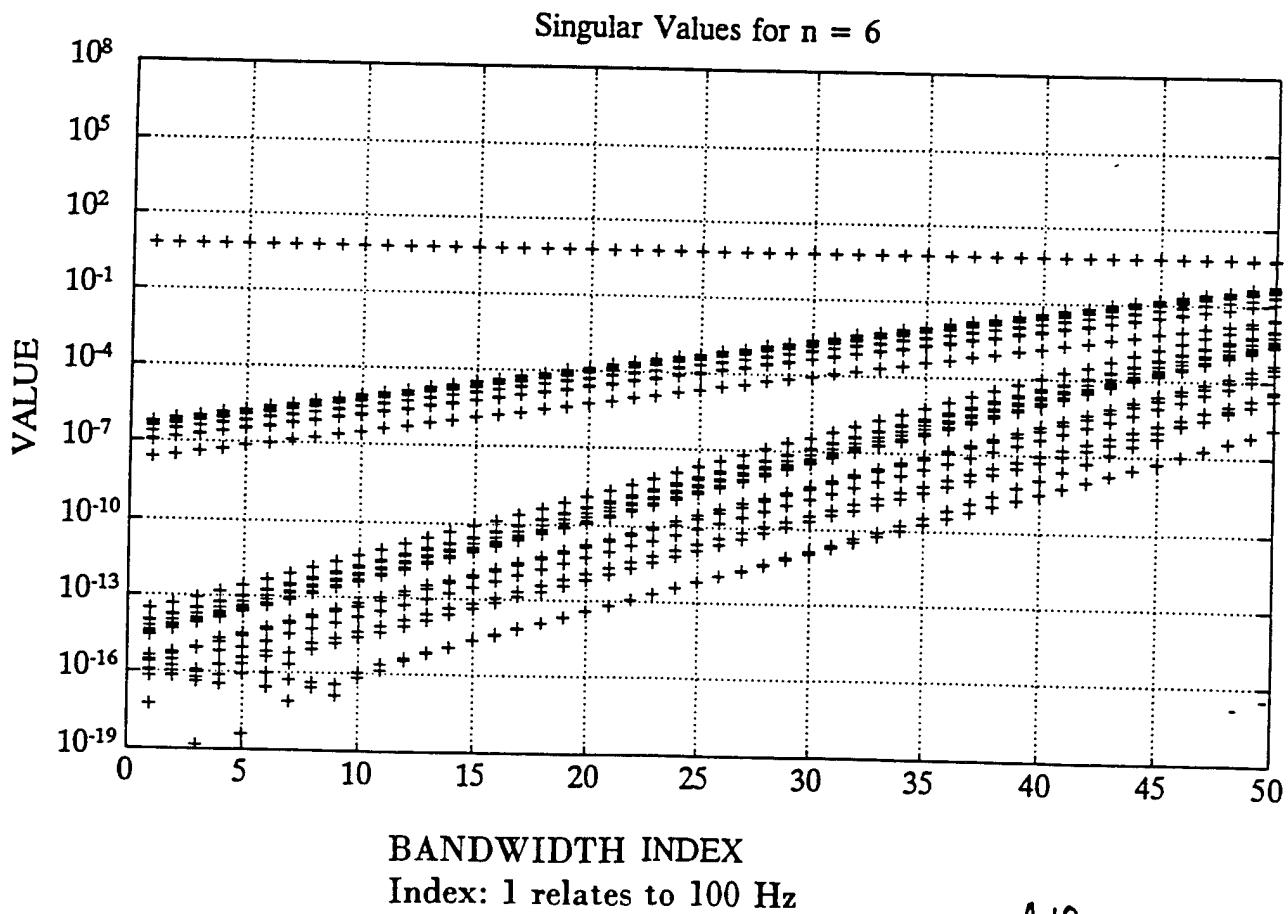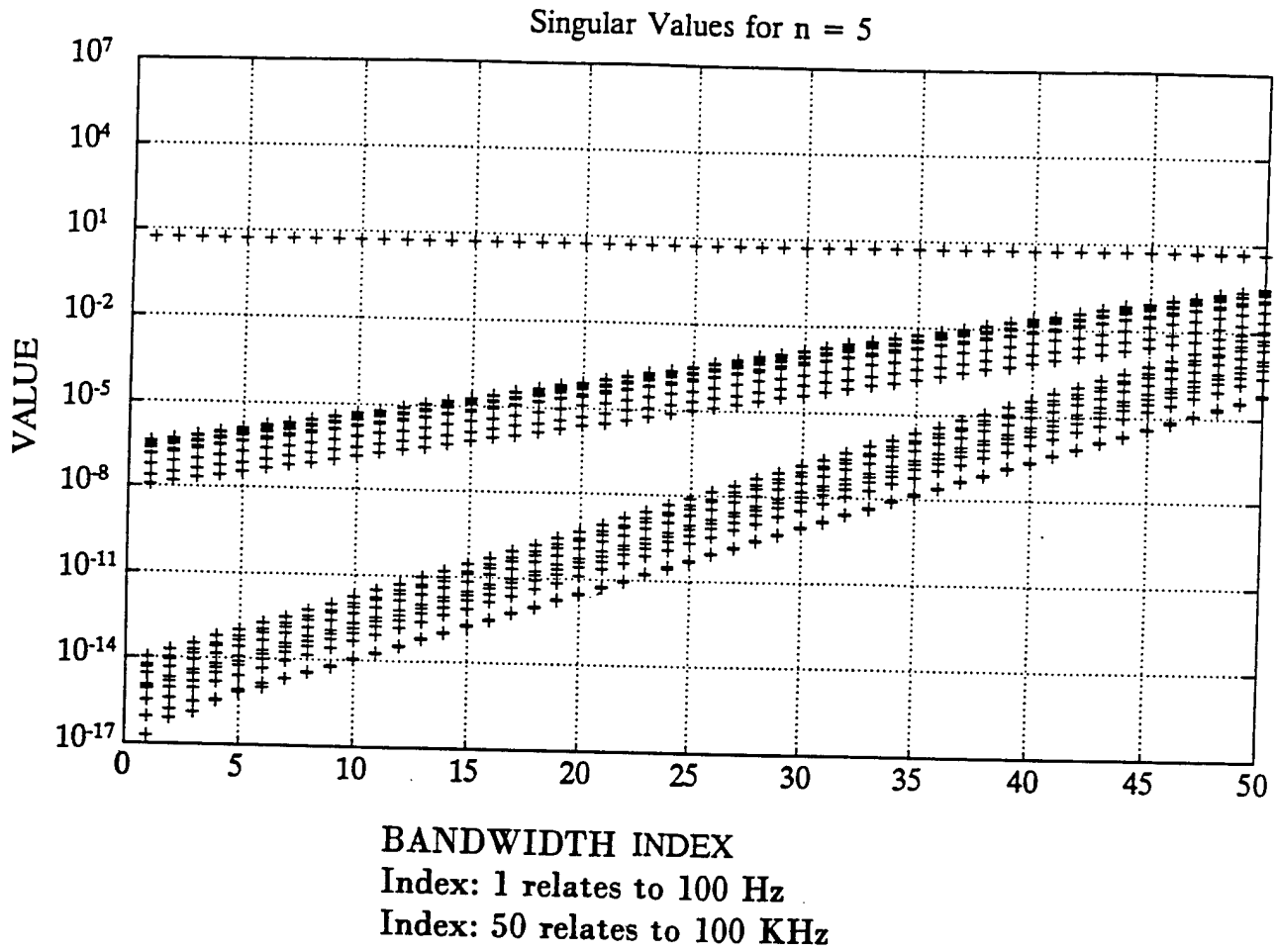
Figure 11
Singular Value Distribution For Rpp Correlation Matrix
For 5 and 6 Randomly Located Auxiliary Sensors
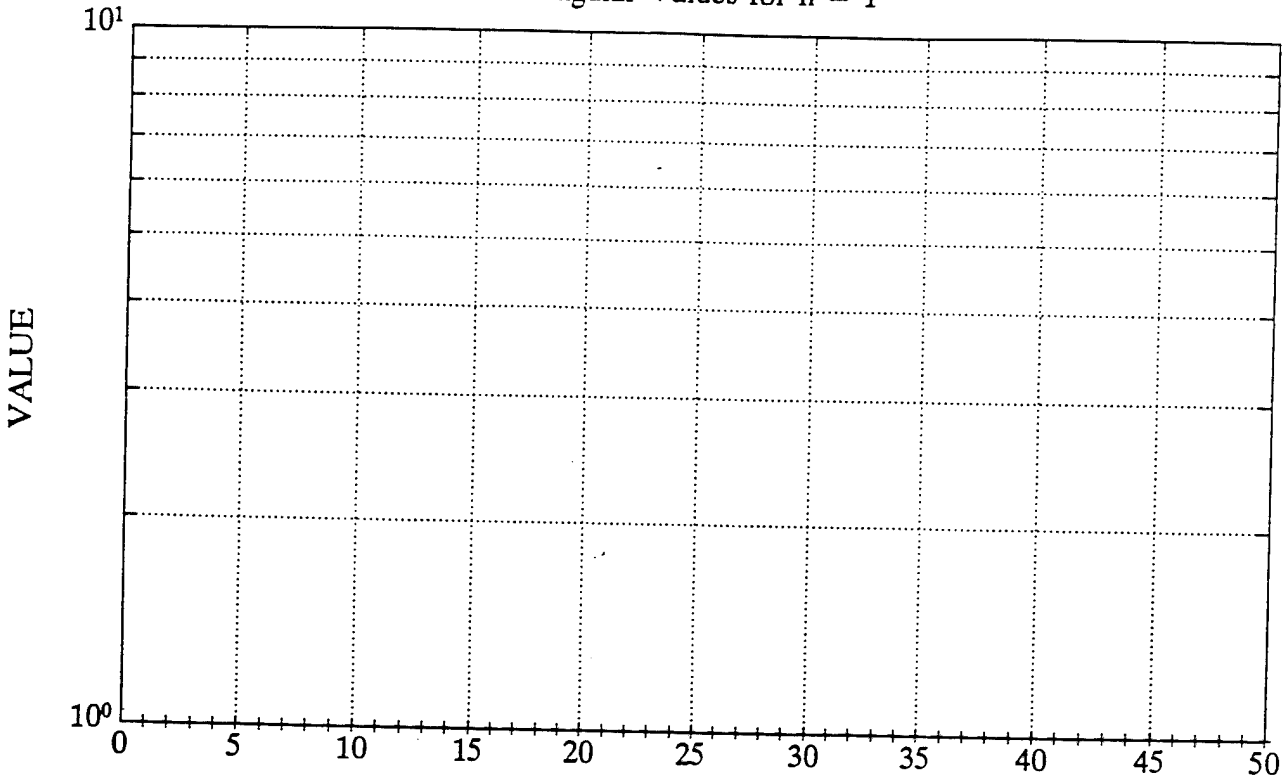
Singular Values for n = 1

BANDWIDTH INDEX
Index: 1 relates to 100 Hz
Index: 50 relates to 100 KHz

Singular Values for n = 2
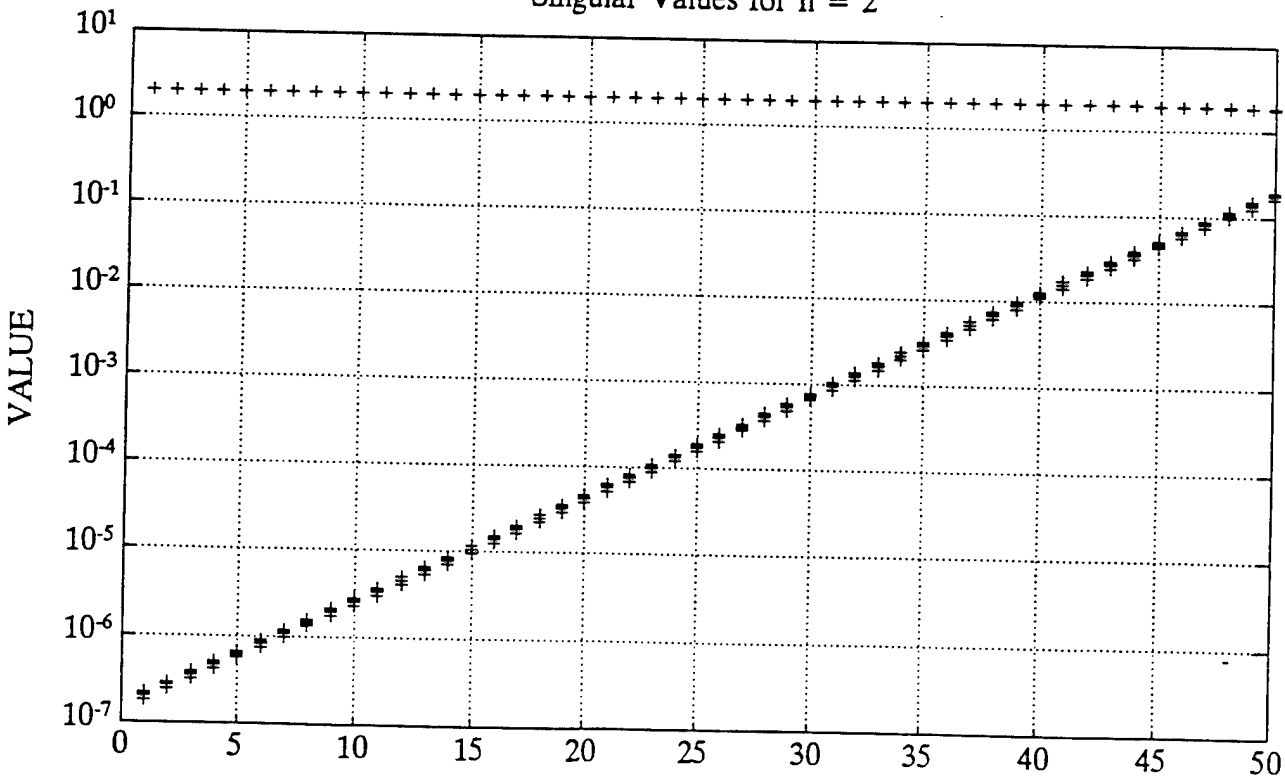
BANDWIDTH INDEX
Index: 1 relates to 100 Hz

Figure 12
Singular Value Distribution For Rpp Correlation Matrix
For 1 and 2 Quasi Uniformly Located Auxiliary Sensors
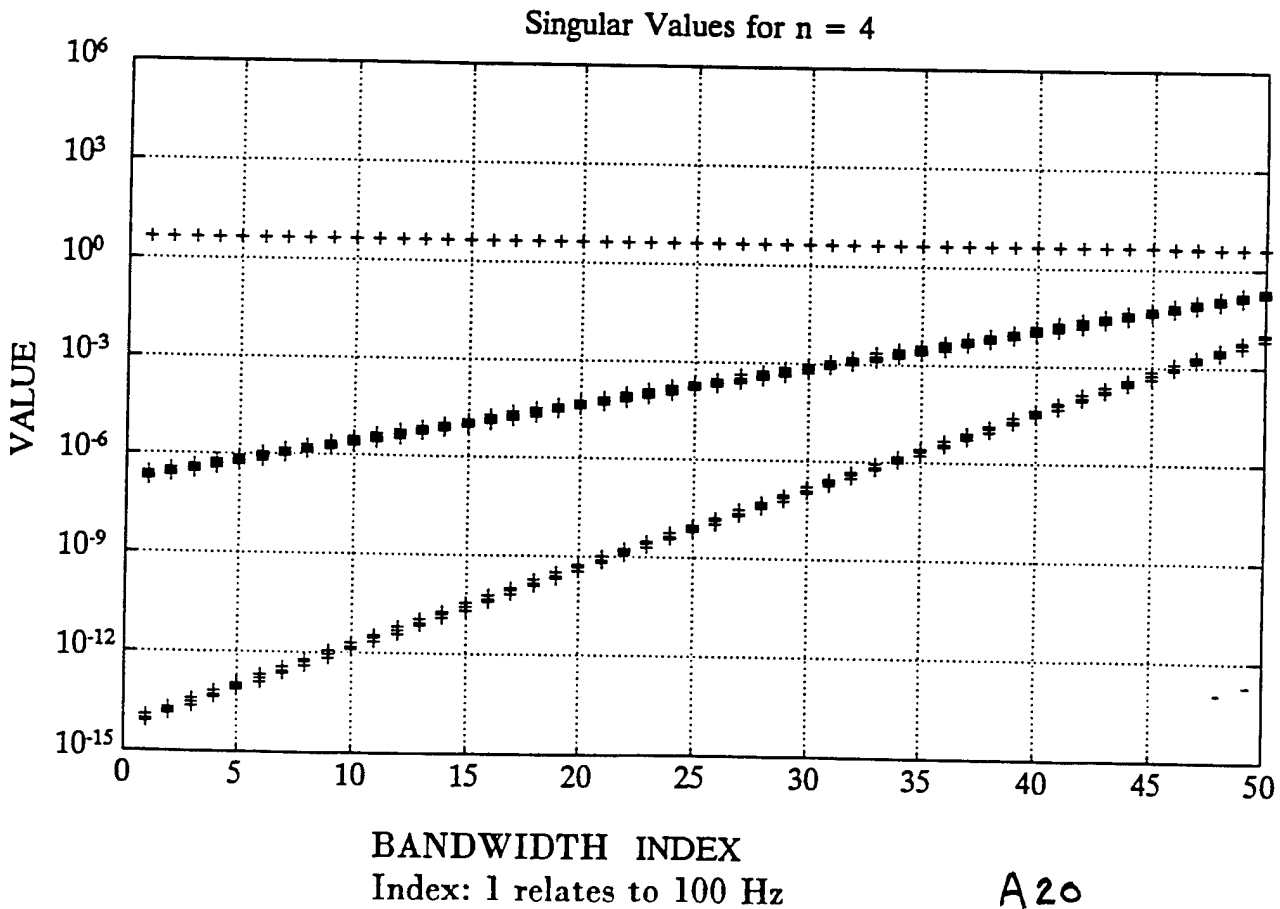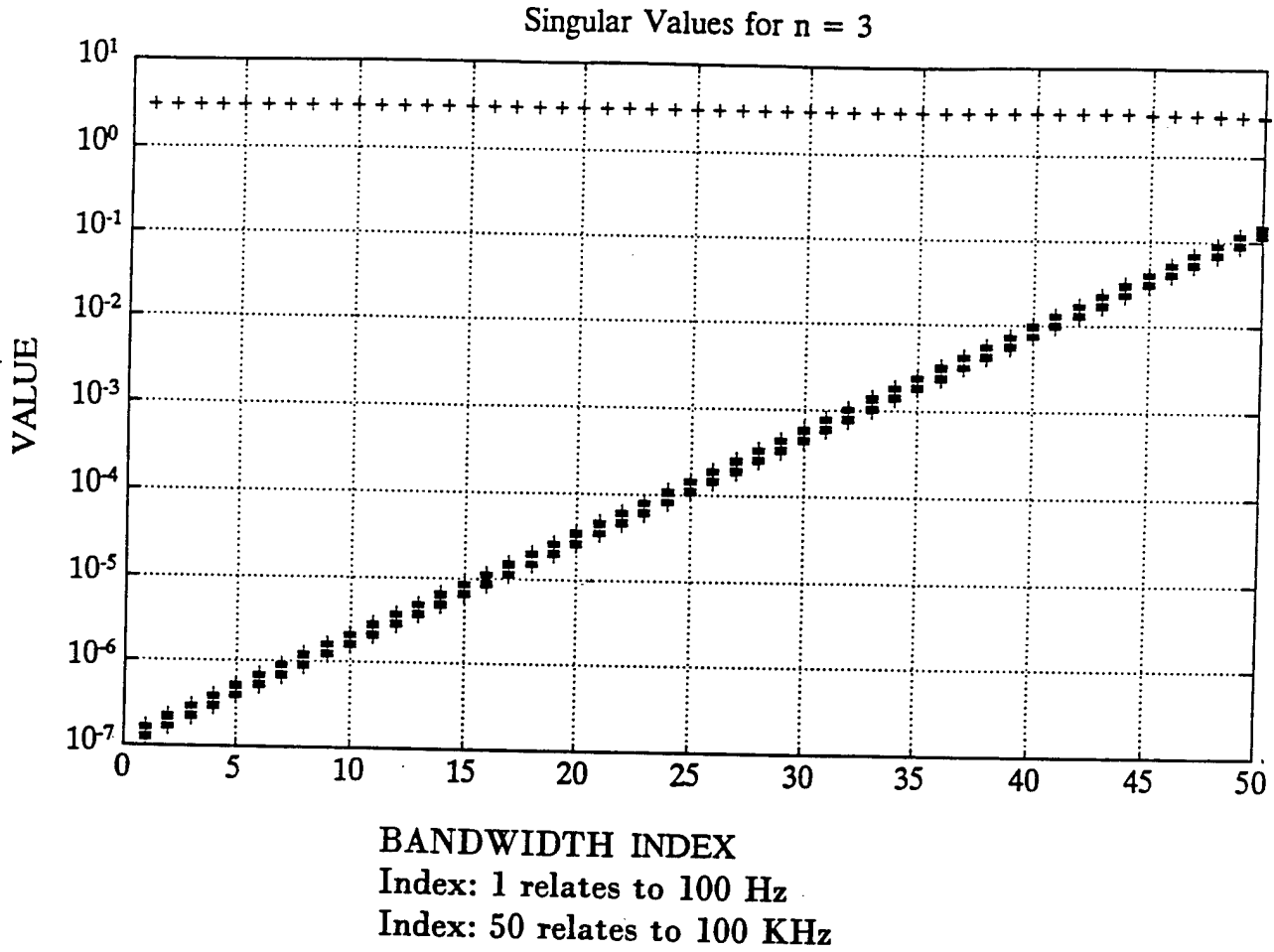
A 19

Singular Values for n = 3

BANDWIDTH INDEX
Index: 1 relates to 100 Hz
Index: 50 relates to 100 KHz

Singular Values for n = 4

BANDWIDTH INDEX
Index: 1 relates to 100 Hz

A 20

Singular Values for n = 5

BANDWIDTH INDEX
Index: 1 relates to 100 Hz
Index: 50 relates to 100 KHz

Singular Values for n = 6

BANDWIDTH INDEX
Index: 1 relates to 100 Hz

A 21
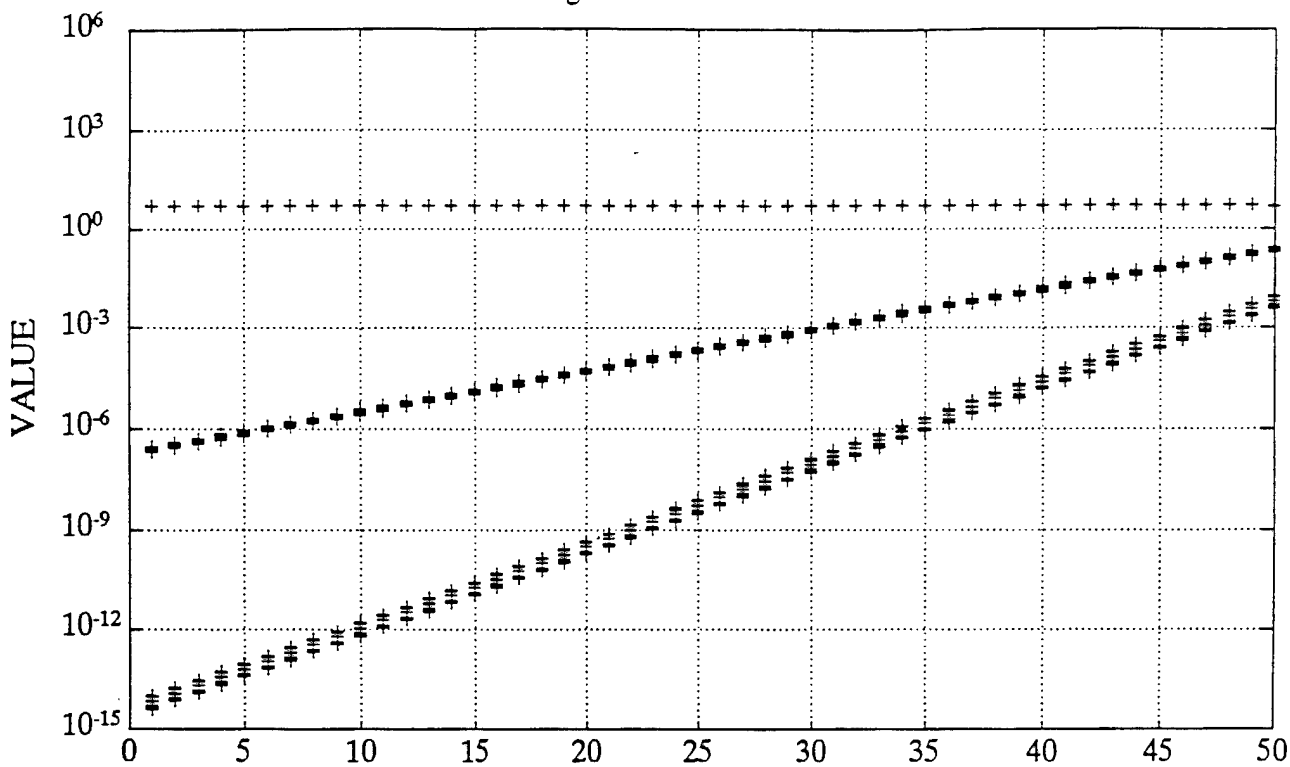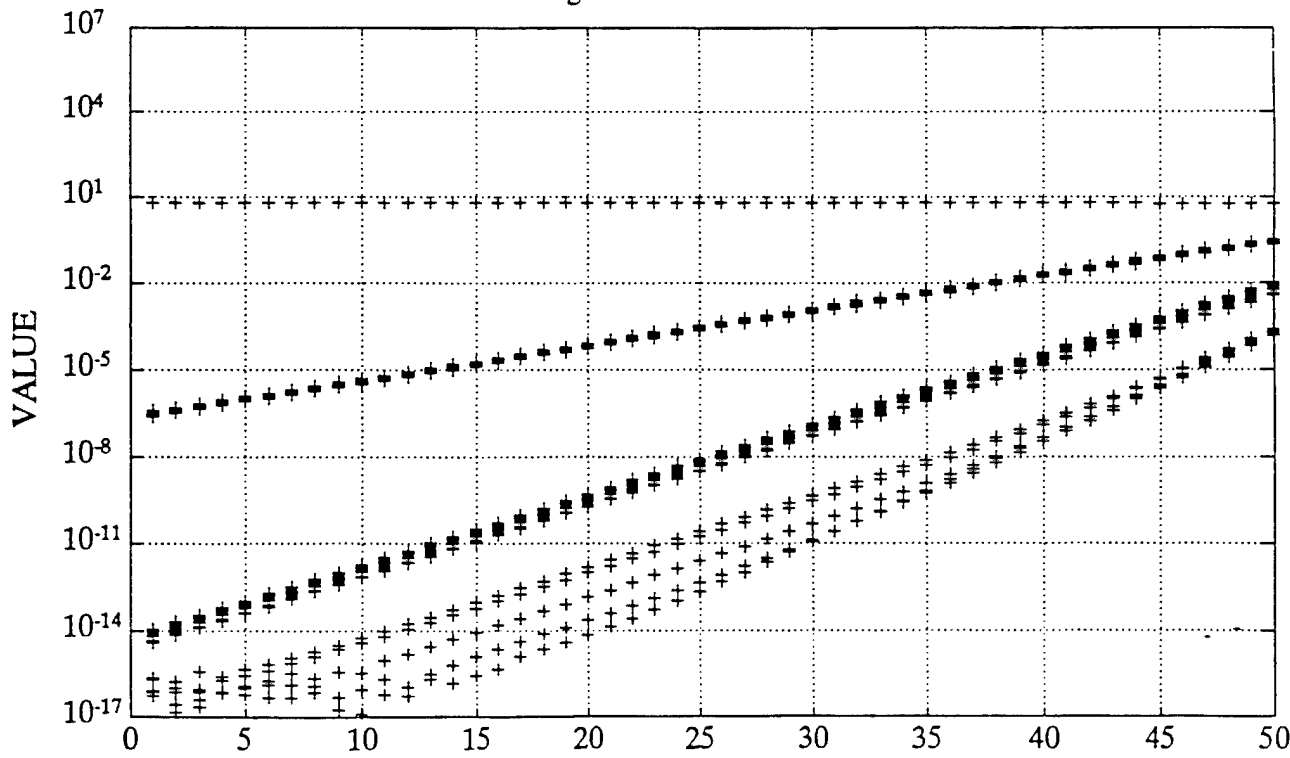
Figure 14
Singular Value Distribution For Rpp Correlation Matrix
For 5 and 6 Quasi Uniformly Located Auxiliary Sensors

APPENDIX
MATLAB ANALYSIS PROGRAM LISTINGS

```
% This program computes & plots the error between Si(x)/x and an approximation
% 1-.0555555 x^2 for small x.
%
% Program: SIX.M        Author: W. HARTHILL            Date: 6-15-94
%
axis('square')
x=logspace(-5,-2,500);
y=sixox(x);
ya=1-.0555555*(x.^2);
loglog(x,abs(ya-y),'-g')
grid
title('Error Between (1-.0555555*X^2) & SI(X)/X VS X')
xlabel('X')
ylabel('ERROR')
```

A23

```
% This program performs a simulation of the performance of the noise canceller.
% For PEMI Magnetic Induction Detector with an attempt to make sensors symmetric
%
% Program: UXOSNR5.M    Author: W. HARTHILL     Date: 6-14-94
%
!del q.met;
c=1e+08;r=150;nmax=6;kmax=20;rand('normal');
for n=1:nmax;% Loop over number of sensors
hold off;clg;
for k=1:kmax;% Loop for Monte Carlo
rho=r*(1+0.1*rand(1,n));% Set up Auxiliary Sensor Positions
if n==1
        th=0;
elseif n==2
        th=[0 pi];
elseif n==3
        th=[0 2*pi/3 4*pi/3];
elseif n==4
        th=[0 0.5*pi pi 1.5*pi];
elseif n==5
        th=[0 2*pi/5 4*pi/5 6*pi/5 8*pi/5];
elseif n==6
        th=[0 2*pi/6 4*pi/6 6*pi/6 8*pi/6 10*pi/6];
end
th=th+0.1*rand(1,n);
xd=rho.*cos(th);yd=rho.*sin(th);% Express aux. sensor positions in [x,y]
xp=reshape(xd,n,1);yp=reshape(yd,n,1);% Reshape data for plotting only
subplot(121);axis([-2*r 2*r -2*r 2*r]);
plot(xp,yp,'+w');grid;
text(-9,-14,'X');text(-200,275,[num2str(n),' aux.sensors']);
xxd=xd'*scones(xd)-scones(xd')*xd;yyd=yd'*scones(yd)-scones(yd')*yd;
d=sqrt(xxd.^2+yyd.^2);dn=sqrt(xd.^2+yd.^2)';% Correlation Matrices
x=[];y=[];
for b=logspace(2,5,50);
con=2*pi*b/c;rpp=sixox(con*d);rpn=sixox(con*dn);
del=-10*log10(1-rpn'*(rpp\rpn));x=[x b];y=[y del];
end
subplot(122);axis([2 5 0 120]);semilogx(x,y,'-w');grid;hold on
end
hold off;
subplot(121);title('AUXILIARY SENSOR LOCATIONS')
xlabel('X DISTANCE');ylabel('Y DISTANCE');
subplot(122);title('DEGREE OF NOISE CANCELLATION')
xlabel('BANDWIDTH HZ.');ylabel('CANCELLATION dB.');
meta q
end
gp q
```

```
% This program plots the singular values of the Correlation Rpp for symmetric
% Positions of the auxiliary sensors
%
% Program: UXOSNR6.M    Author: W. HARTHILL      Date: 6-14-94
%
!del q.met
c=1e+08;r=150;nmax=6;kmax=5;findmax=50;rand('normal');
for n=1:nmax;% Loop over number of sensors
hold off;clg;
x=[];y=[];sing=[];
%
for k=1:kmax;% Loop for Monte Carlo
rho=r*(1+0.1*rand(1,n));% Set up Auxiliary Sensor Positions
if n==1
        th=0;
elseif n==2
        th=[0 pi];
elseif n==3
        th=[0 2*pi/3 4*pi/3];
elseif n==4
        th=[0 0.5*pi pi 1.5*pi];
elseif n==5
        th=[0 2*pi/5 4*pi/5 6*pi/5 8*pi/5];
elseif n==6
        th=[0 2*pi/6 4*pi/6 6*pi/6 8*pi/6 10*pi/6];
end
th=th+0.1*rand(1,n);
xd=rho.*cos(th);yd=rho.*sin(th);
xxd=xd'*scones(xd)-scones(xd')*xd;yyd=yd'*scones(yd)-scones(yd')*yd;
d=sqrt(xxd.^2+yyd.^2);
for b=logspace(2,5,findmax);
con=2*pi*b/c;rpp=sixox(con*d);
[u dd v]=svd(rpp);dd=diag(dd);sing=[sing dd];
end
end
hold off;clg;
rovec=[1:findmax];
arg=[];
for i=1:kmax
        arg=[arg rovec];
end
x=scones(sing(:,1))*arg;
semilogy(x,sing,'+w');
grid;
title(['Singular Values for n = ',num2str(n)])
xlabel('INDEX')
ylabel('VALUE')
meta q;
end
gpp q;
```

527-1776

A25

```
% This program performs a simulation of the performance of the noise canceller.
% For PEMI Magnetic Induction Detector with random sensor locations
%
% Program: UXOSNR7.M   Author: W. HARTHILL      Date: 6-14-94
%
!del q.met;
c=1e+08;r=150;nmax=6;kmax=20;rand('uniform');
for n=1:nmax;% Loop over number of sensors
hold off;clg;
for k=1:kmax;% Loop for Monte Carlo
rho=r*(rand(1,n)+0.5);th=2*pi*rand(1,n);
xd=rho.*cos(th);yd=rho.*sin(th);% Express aux. sensor positions in [x,y]
xp=reshape(xd,n,1);yp=reshape(yd,n,1);% Reshape data for plotting only
subplot(121);axis([-2*r 2*r -2*r 2*r]);
plot(xp,yp,'+w');grid;
text(-9,-14,'X');text(-200,275,[num2str(n),' aux.sensors']);
xxd=xd'*scones(xd)-scones(xd')*xd;yyd=yd'*scones(yd)-scones(yd')*yd;
d=sqrt(xxd.^2+yyd.^2);dn=sqrt(xd.^2+yd.^2)';% Correlation Matrices
x=[];y=[];
for b=logspace(2,5,50);
con=2*pi*b/c;rpp=sixox(con*d);rpn=sixox(con*dn);
del=-10*log10(1-rpn'*(rpp\rpn));x=[x b];y=[y del];
end
subplot(122);axis([2 5 0 120]);semilogx(x,y,'-w');grid;hold on
end
hold off;
subplot(121);title('AUXILIARY SENSOR LOCATIONS')
xlabel('X DISTANCE');ylabel('Y DISTANCE');
subplot(122);title('DEGREE OF NOISE CANCELLATION')
xlabel('BANDWIDTH HZ.');ylabel('CANCELLATION dB.');
meta q
end
gp q
```

A26

```
% This program plots the singular values of the Correlation Rpp for random
% Positions of the auxiliary sensors
%
% Program: UXOSNR8.M     Author: W. HARTHILL     Date: 6-14-94
%
del q.met
c=1e+08;r=150;nmax=6;kmax=5;findmax=50;rand('uniform');
for n=1:nmax;% Loop over number of sensors
x=[];y=[];sing=[];
%
for k=1:kmax;% Loop for Monte Carlo
rho=r*(rand(1,n)+0.5);th=2*pi*rand(1,n);
xd=rho.*cos(th);yd=rho.*sin(th);
xxd=xd'*scones(xd)-scones(xd')*xd;yyd=yd'*scones(yd)-scones(yd')*yd;
d=sqrt(xxd.^2+yyd.^2);
for b=logspace(2,5,findmax);
con=2*pi*b/c;rpp=sixox(con*d);
[u dd v]=svd(rpp);dd=diag(dd);sing=[sing dd];
end
end
rovec=[1:findmax];
arg=[];
for i=1:kmax
        arg=[arg rovec];
end
x=scones(sing(:,1))*arg;
hold off;clg;
semilogy(x,sing,'+w');
grid;
title(['Singular Values for n = ',num2str(n)])
xlabel('INDEX')
ylabel('VALUE')
meta q;
end
!gp q;
```

8.   **Appendix B: Magnetometer Vendor Sheet**

GSM-19

GEM Systems

ADVANCED MAGNETOMETERS

Magnetometer
VLF System

Slow & Fast Sampling
Magnetometers
Gradiometers
Omnidirectional VLF

82

GSM-19 Magnetometer / VLF System

The GSM-19 is a state-of-the-art magnetometer / VLF system that delivers both the quality of data and the extensive capabilities required to perform a broad spectrum of applications. Whether the application calls for detailed ground surveys, high-resolution marine surveys, or remotely controlled magnetic observatory measurements, you can count on the GSM-19 system to meet your goals.

The GSM-19 can be configured as either an Overhauser effect proton precession magnetometer or a conventional proton unit.

GEM's advanced Overhauser version employs continuous radiofrequency polarization and special sensors to maximize the signal-to-noise ratio. Instrument sensitivity (0.05 gamma), resolution (0.01 gamma) and absolute accuracy (0.2 gamma) set new performance standards. Moreover omnidirectional sensors ensure a high quality of data even in low magnetic latitudes.

You can also take advantage of versatile options that reduce field costs and increase survey productivity. And the lightweight Overhauser unit is easy to transport and operate in the field (console with rechargeable batteries weighs only 2.1 kilograms).

The modular design of the GSM-19 Overhauser magnetometer ensures that the system can be upgraded as workloads change. You can select from a number of building blocks, including:

- Simultaneous gradiometer.
- Continuous profiling "Walking" magnetometer / gradiometer.
- Very fast sampling (up to 5 readings per second) magnetometer/gradiometer.
- Omnidirectional VLF.
- Shallow or deep marine operation.
- Remote control for observatory and airborne base station applications.

If your application does not yet require the extended capabilities or the cost benefits of an Overhauser unit, a conventional GSM-19 unit is available. This dedicated proton magnetometer can be equipped with gradiometer or VLF options, and is upgradable to an Overhauser magnetometer.

The Overhauser and conventional magnetometers share many powerful features:

- Easy to learn interactive menu.
- Streamlined grid coordinate system with "end of line" quick change capability.
- 128 kilobyte basic memory, expandable to 2 Megabytes.
- Programmable RS-232 high-speed data transfer (to 19.2 kilobaud).
- 50 and 60 Hz filters, user selectable.
- Automatic tuning and base station synchronization.

Type of Magnetometer		Gradiometer	"Walking" Mag	"Walking" Grad	Hip-Chain Mag	Hip Chain Grad	VLF	Shallow Marine	Remote Control
Conventional Proton		✓					✓		✓
Overhauser Proton	Total Field	✓	✓	✓	✓	✓	✓	✓	✓
	"Walking"			✓	✓	✓	✓	✓	✓
	Hip-Chain		✓	✓		✓	✓	✓	

Building Blocks (Upgrade Options)

A Proton Total Field system may be upgraded to an Overhauser system, which allows further upgrade to "Walking" and Hip Chain models.

GSM-19 Overhauser System
A Full Range of Building Blocks

Simultaneous Gradiometer

Many mining, environmental, and archaeological applications call for high-sensitivity gradiometer surveys. The GSM-19 meets these needs in several ways. For example, simultaneous measurement of the magnetic field at both sensors eliminates diurnal magnetic effects. And Overhauser proton precession improves data accuracy and precision. The net result is a true gradient reading that resolves even weak anomalies (less than 0.25 gamma).

Omnidirectional VLF

With GEM's omnidirectional VLF option, up to three stations of VLF data can be acquired without orienting. Moreover, the operator is able to record both magnetic and VLF data with a single stroke on the keypad.

A 12-bit A/D converter has also been incorporated in the VLF instrumentation to enhance resolution of near-surface electromagnetic conductors.

"Walking" Magnetometer / Gradiometer

GEM's unique "Walking" option enables acquisition of nearly continuous data on survey lines. Similar to an airborne survey in principle, data is recorded at discrete time intervals (up to 2 readings per second) as the instrument travels along the line. At each major survey picket (fiducial), the operator touches a designated key. The "Walking Mag" automatically assigns a linearly interpolated coordinate to all intervening readings.

A main benefit of the "Walking" option is that the high sample density improves definition of geologic structures. And because the operator can record data on a near-continuous basis, the "Walking Mag" increases survey efficiency and minimizes field expenditures -- especially for highly detailed ground-based surveys.

As shown below, near-continuous measurements increase definition. Results from the GSM-19 "Walking Mag" (273 readings over 150 m with 2 sec. cycle time) were compared with results from a standard magnetometer (13 readings over 150 m).

Near-Continuous Surveys Improve Definition of Magnetic Anomalies

Data Courtesy of VAL D'OR GEOPHYSIQUE LTEE

B 4   Position (m)
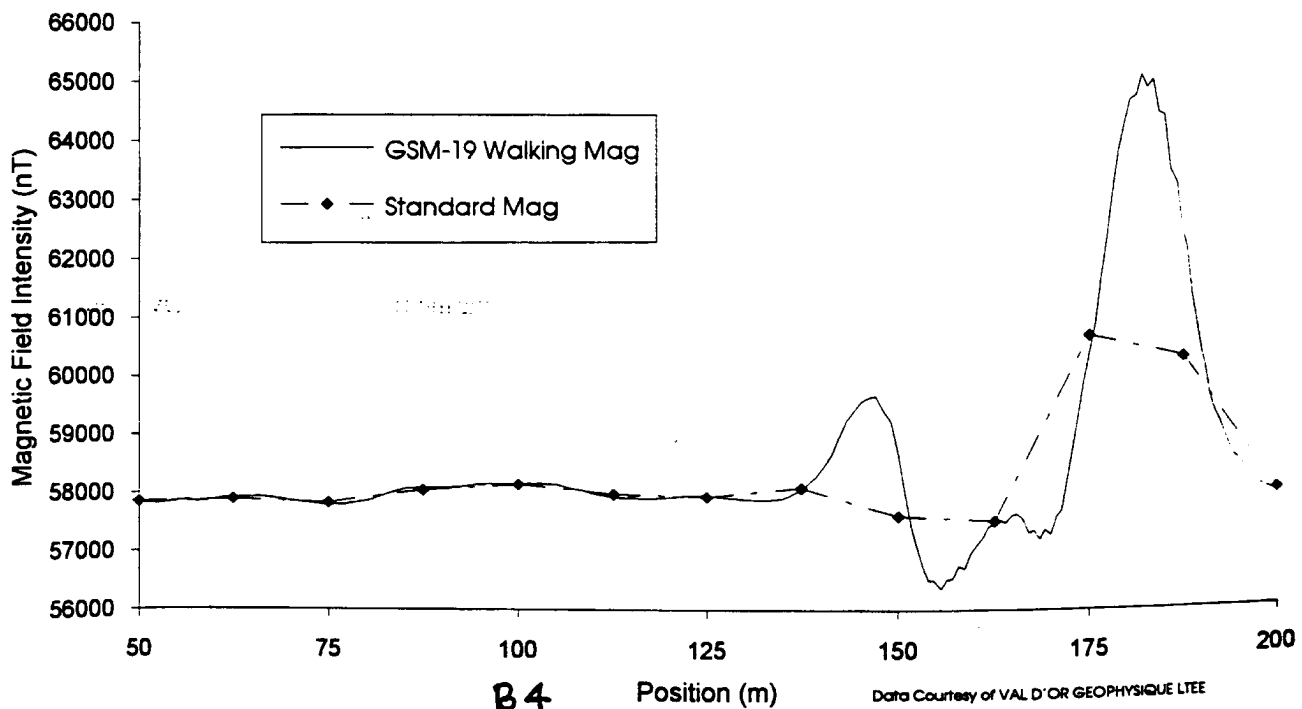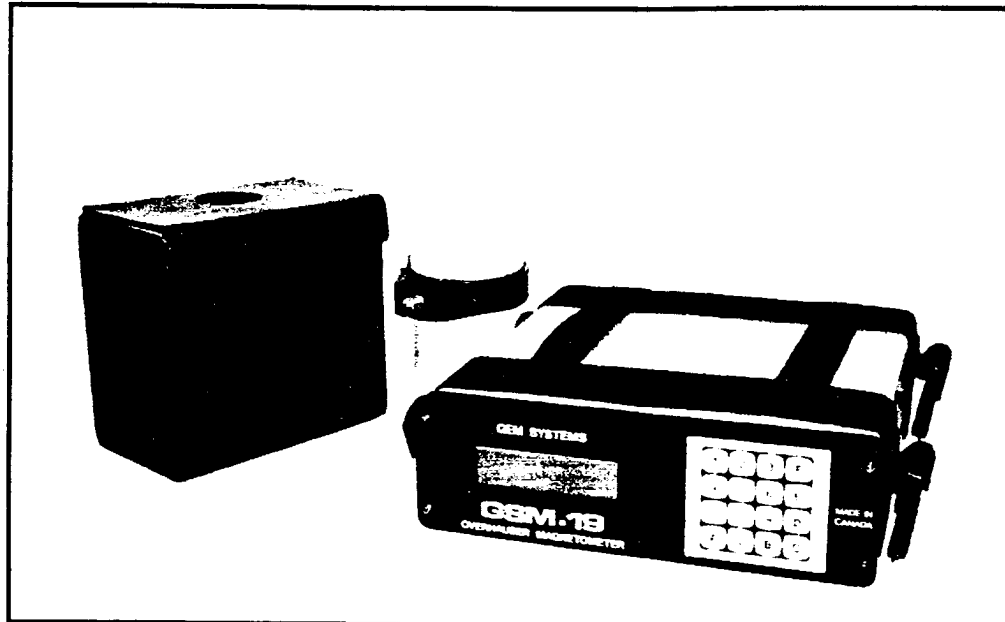
GSM-19 console with magnetic and VLF sensors

Fast Sampling Magnetometer / Gradiometer

The GSM-19 fast sampling option allows you to collect data at rates as high as 5 readings per second. Fast sampling provides the high spatial resolution needed in detailed marine. or vehicle-borne surveys, and in anomalous magnetic terrains.

This fast sampling capability is also used in the Hip Chain magnetometer/gradiometer -- developed primarily for environmental and archaeological applications.

The Hip Chain system minimizes the need for pickets and reduces line preparation costs. Operators simply affix a cord at one end of the survey line, attach the Hip Chain to the waist, and walk along the line. Readings are triggered automatically as the cord unwinds.

Remote Control Operation

Targeted to observatory, marine. and airborne base station applications, this option allows users to set parameters and initiate measurements from a computer terminal using standard RS-232 commands.

A real-time transmission capability is provided so that data quality can be monitored while marine or vehicle-borne surveys are in progress.

And to ensure that the GSM-19 is fully compatible with existing marine or airborne data acquisition systems, GEM has included one and two-channel analog output capabilities.

Shallow and Deep Marine

GEM has developed two marine versions of the GSM-19 Overhauser magnetometer to meet the highly specialized requirements of petroleum explorationists. The maximum depth for the shallow unit is 100 metres, and deep marine units are routinely operated at depths exceeding 400 metres.

With a shallow marine unit, a sealed fish houses an Overhauser sensor. Signals are transferred via a tow cable to a console where they are counted into magnetic field data, and stored in memory, or transmitted via ASCII serial output.

An important advantage of the shallow marine unit is its low power consumption. A standard 12 or 24 Volt battery is sufficient to run the magnetometer for days at a rate of two readings per second.

The deep marine fish houses both an Overhauser sensor, and microprocessor-based electronics. Complete measurement is performed within the fish, and data are sent digitally through a tow cable that also supplies power.

The main benefits of the deep marine unit include high resolution (signals up to 0.01 gamma resolution can be acquired using a sensor of only 0.2 litre volume), virtually unlimited cable length, ease of operation, and reliability. Temperature and pressure sensors can also be provided.

B5

GSM-19 Advanced Features

An instrument's effectiveness is measured by its ability to handle highly specialized user demands. With the GSM-19. these requirements can be met through a number of advanced features.

Compatible With Different Magnetometers

To protect our customers' investments in purchased equipment. GEM has adopted an Open Systems approach. The lightweight Overhauser magnetometer can be used as a field unit in combination with another manufacturer's base station.

Memory Expandable to 2 Megabytes

A GSM-19 field magnetometer can store up to 8,000 readings with 128 kb memory, and 131,000 readings with 2 Mb. A base station will store, respectively, between 43,000 and 700,000 readings. A "Walking" magnetometer will store 21,000 readings with 128 kb memory, and 340,000 with extended memory.

Automatic Tuning

Tuning is automatic in all modes of operation with initial preset. An override option is also provided for manual and remote modes. Tuning steps are 1,000 gammas wide.

Adaptability to High Gradients

In standard instruments, a gradient in the magnetic field across the sensor volume can shorten the decay time of the proton precession signal. However, the GSM-19 monitors the signal decay, and calculates the optimal time interval for measurement. Warning messages appear on the display when the measuring interval becomes too short.

Alphanumeric Display and Keyboard

The GSM-19 has a comfortable 4 x 20 character alphanumeric display and a 16 key keypad with tactile feedback. Operation is menu driven, and simple enough for a beginner to operate with confidence. The keypad enables operators to enter fully worded comments with no limit in the length of text.

Overhauser Proton Precession

With Overhauser proton precession. an electron-rich fluid (containing free radicals) is added to a standard hydrogen-rich fluid. This mixture increases the polarization by a factor of 5000 in comparison with standard liquids. And in contrast to conventional proton precession methods. Overhauser proton precession uses a radiofrequency (RF) magnetic field -- and requires only a fraction of a Watt of RF power. rather than a high-power direct current field.

Overhauser magnetic systems therefore maximize resolution and minimize power consumption. Another advantage is that polarization and measurement can occur simultaneously. GEM has used this capability to develop its "Walking" magnetometer / gradiometer and Fast Sampling options.

GEM Systems Inc.

With more than a decade of research and development incorporated into the GSM-19 Overhauser and proton precession magnetometers, GEM Systems is committed to providing its customers with state-of-the-art instrumentation.

In addition to offering the GSM-19, GEM also designs and builds solar-powered proton magnetometers for land-based applications, and optically pumped potassium magnetometers for airborne and other applications.

terraplus

TERRAPLUS USA INC.
625 West Valley Road   (303) 799-4140
Littleton, Colorado 80124   Fax (303) 799-4776

☛9329

Specifications

Performance

	Overhauser	Proton
Resolution:	0.01 nT	0.01 nT
Relative Sensitivity:	0.02 nT	0.2 nT
Absolute Accuracy:	0.2 nT	1 nT
Range:	20.000 to 120.000 nT	20.000 to 120.000 nT
Gradient Tolerance:	Over 10.000 nT/m	Over 7.000 nT/m

Operating Modes

Manual:	Coordinates. time, date and reading stored automatically at min. 3 second interval.
Base Station:	Time, date and reading stored at 3 to 60 second interval (higher speeds available).
"Walking":	Time, date and reading stored at coordinates of fiducial with 1 or 2 sec. cycle time.
Hip Chain:	Equidistant coordinates. time, date and reading stored automatically. Distance interval of readings is programmable.
Remote Control:	Optional remote control using RS-232 interface.
Input/Output:	RS-232 or analog (optional) output using 6 pin weatherproof connector.

Operating Parameters

Power Consumption:	Only 2 Ws per reading for Overhauser, and 12 Ws per reading for Proton magnetometer. Will operate continuously for 45 hours on standby.
Power Source:	12V 1.9 Ah sealed lead acid battery standard, other batteries available.
Operating Temperature:	-40°C to +60°C.

Storage Capacity

Manual Operation:	8,000 readings standard, 131,000 optional. With 3 VLF stations 3,100 standard, 58,000 optional.
Base Station:	43,000 readings standard, 700,000 optional (580 hour or 24 day uninterrupted operation with 3 sec. interval).
Gradiometer:	6,800 readings standard. 110,000 optional. With 3 VLF stations 2,900 standard, 46,000 optional.

Omnidirectional VLF

Performance Parameters:	Resolution 0.5% and range to +/- 200% of total field. Frequency 15 to 30 kHz.
Measured Parameters:	Vertical in-phase & out-of-phase, 2 horizontal components, coordinates. date, and time.
Features:	Up to 3 stations measured automatically, in-field data review, displays station field strength continuously, and tilt correction for up to +/- 10° tilts.
Dimensions and Weight:	93 x 143 x 150 mm and weighs only 1.0 kg.

Dimensions and Weights

Dimensions:	• Console 223 x 69 x 240 mm. • Sensor 170 x 71 mm diameter cylinder.
Weight:	• Console 2.1 kg. • Sensor and staff assembly 2.0 kg.
Standard Package:	• Console with batteries, harness, charger, and case. Sensor with cable, connector and staff.

This page is intentionally left blank

9.   **Appendix C: NAVEODTECHDIV Magnetometer Test Range Test Plan**

ALLIANT TECHSYSTEMS INC.

Marine Systems West
6500 Harbour Heights Parkway
Mukilteo, WA 98275-4844

LETTER OF TRANSMITTAL

TO: Receiving Officer
Attn: EODTD Code 50B22
Indian Head Division
Naval Surface Warfare Center
101 Strauss Avenue
Indian Head, MD 20640-5035

LETTER S/N: ___2120-012___

DATE: ___28 June 1995___

PROGRAM: ___Pulsed Electromagnetic___
___Induction (PEMI)___

DATA ITEM: ___Test Plans/Procedures___

CONTRACT NO.: ___N00174-94-C-0083___

CLIN: ___0002___

CDRL NO.: ___A002___
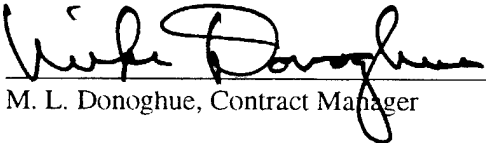
☐ REVIEW REQUIRED

☐ APPROVAL REQUIRED

☐ NO APPROVAL REQUIRED

☒ FOR INFORMATION

REMARKS: Enclosed for review and information is CDRL A002, Test Plans/Procedures Document for the 5-Day Field PEMI Demonstration scheduled for July 24-28 1995, at NAVEODTECHDIV Indian Head Division, MD.

BY: _M. L. Donoghue, Contract Manager_

CDRL DISTRIBUTION:

ADDRESSEE	COPIES/REPRO
NEODTD 50B22	5/1
AEC	1/0
NAVSURWARFCEN	1/0

C2

DOCUMENT NO.: __0083-94-011__

DATE: __28 June 1995__

REVISION: _____

PULSED ELECTROMAGNETIC INDUCTION (PEMI)

DATA ITEM COVER SHEET

DATA ITEM TITLE: **Test Plans/Procedures**

DD 1423 NUMBER: **A002**

CONTRACT NUMBER: **N00174-94-C-0083**

SECURITY CLASSIFICATION: **UNCLASSIFIED**

PREPARED BY: _P. Kaczkowski_
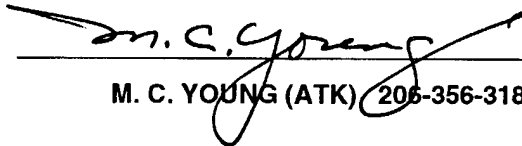
P. KACZKOWSKI (APL/UW) 206-543-1283

PREPARED BY: _E. Rissberger_

E. J. RISSBERGER (ATK) 206-356-3490

REVIEWED BY: _M. C. Young_

M. C. YOUNG (ATK) 206-356-3184

ALLIANT TECHSYSTEMS

Marine Systems West

6500 Harbour Heights Parkway

Mukilteo, WA 98275-4844

C3

This page is intentionally left blank

PULSED ELECTROMAGNETIC INDUCTION (PEMI)
Test Plans/Procedures
June 1995
CDRL A002

Table of Contents

This page is intentionally left blank

PULSED ELECTROMAGNETIC INDUCTION (PEMI)
N00174-94-C-0083

Section I Introduction

The FY95 Pulsed ElectroMagnetic Induction (PEMI) program has been carried out by the Applied Physics Laboratory (APL), University of Washington, Seattle, and Alliant Techsystems (ATK) , Mukilteo, for the Naval Explosive Ordnance Disposal Technology Division (NAVEODTECHDIV) in Indian Head, Maryland. The program includes several phases of work: modeling and simulation, assembling data collection hardware, performing a first field experiment in March/April 1995 in Washington state, and a second field demonstration to be conducted at the NAVEODTECHDIV magnetometer test range in Indian Head, MD. This test plan describes the objectives, plans and procedures, and schedule for the proposed test.

Section II Background

The PEMI method (Pulsed ElectroMagnetic Induction) is a technique used in geophysical prospecting for finding conductive ore bodies and in this program is adapted to the problem of locating and identifying buried unexploded ordnance (UXO). The physical scale of the problem is much smaller than that encountered in mining prospecting, but the large difference in conductivity between the materials making up many types of ordnance and the earth make inductive methods promising candidates for locating such buried targets. Indeed, continuous wave inductive systems are currently being used to find ordnance. However, in many sites the problem of distinguishing between false targets such as shrapnel and whole ordnance is not easily solved, leading to a high false alarm rate and consequently elevated remediation costs. This false alarm problem is common with methods based on magnetometers as well.

The PEMI method uses a pulsed transmission signal (broadband) in order to obtain more classification information than is commonly obtainable with single-frequency systems. Consequently, the PEMI method will be superior to a single-frequency method in a highly cluttered environment where distinguishing between different size targets is helpful. A single-frequency method may have the advantage over a pulse technique in an environment with high levels of ambient electromagnetic noise because the PEMI sensor must be sensitive over a broad band of frequencies. The one-year program funded by NAVEODTECHDIV seeks to examine the applicability of the PEMI method to the problem of locating and identifying buried UXO by developing simple models and testing them against data collected with an off-the-shelf geophysical PEMI system. The first test validated the proposed models by comparing model predictions to measured PEMI responses from simple test targets. (It should be noted that the commercial sensors did not prove to be practical in the UXO application, and two three-axis receivers were designed and built to take the data.) Several UXO responses were also measured and found to be relatively well characterized by simple PEMI models. The measurements are by no means exhaustive, but do provide a partial database of UXO responses to a PEMI system which suggest that the PEMI method can be very useful in UXO remediation.

Section III Objectives

The test to be conducted at the NAVEODTECHDIV site is an engineering test of the PEMI method. The experiment will help NAVEODTECHDIV evaluate the promise of the PEMI method in addressing the UXO problem and in assessing the potential for proceeding with follow-on work. The test has several specific objectives:

C5

PULSED ELECTROMAGNETIC INDUCTION (PEMI)
N00174-94-C-0083

1. To mobilize the PEMI system to Indian Head and survey selected sites of NAVEODTECHDIV 's choosing (3 sites measuring 10m on a side), of which no prior knowledge on either the location or quantity of UXO buried there has been made available.

2. To interpret the data collected on each site and attempt to locate and characterize any conductors found therein. Specifically the conductor characterization includes localization in 3 dimensions, orientation, and approximate size. Identify any UXO if possible.

3. To demonstrate the PEMI system to NAVEODTECHDIV personnel, including demonstrating the survey hardware, data collection procedures, data processing approaches, and interpretation.

4. To provide a report of the test in the final program technical report

Section IV Schedule

The test at the NAVEODTECHDIV site is scheduled for the week of July 24-28, 1995. The plans include for up to a week of testing in Washington state, followed by shipment of the equipment to Maryland for collection of data. The plan is to conduct surveys of three independent sites; it is anticipated that the first day (Monday 24) will be used to set up the equipment, and that each site will take one day to survey. The fifth day (Friday 28) will be reserved for contingencies or repeated measurements and disassembly of the equipment. The program schedule is shown in Figure 1.

Section V Methods and Procedures

The PEMI system must first be reassembled after shipment and tested for functionality. Test targets will be included with the PEMI equipment to aid in verification of the system. A commercially available magnetometer shall also be included to augment the PEMI system in the initial identification of anomalies.

The lack of electrical utility power at the test site will require use of a portable power generator. A 1 kW portable generator shall be acquired in Seattle and shipped to the test site with the rest of the PEMI instrumentation. This may be a strong source of noise and we will have to experiment with the distance required to reduce the interference of the power source. For this purpose, a 700 foot long power cable used in the first experiment at Mukilteo will be shipped with the equipment. One aspect of the signal processing is specifically designed to reduce the influence of power line noise by effectively notch filtering the data in a narrow band around the line frequency. The success of this technique depends on the stability of that power line frequency. Undoubtedly, fine tuning of this approach will be required since the generator is not expected to be as stable as a utility feed.

Measurements of ambient noise will be carried out using one sensor and also using two sensors, spatially separated at varying distances to measure the coherence of the ambient electromagnetic field. Strong coherence over tens of meters is necessary to take advantage of coherent noise cancellation using an auxiliary sensor.

At each 10 meter test site the first step will be to establish a local coordinate system and a one-meter grid. Stakes and strings shall be used to mark the grid during the duration of the

demonstration. A water level, used to measure the elevation of the receiver coils at each station, is installed along with a reference grade marker. Then, the square transmitter loop (5 meters on a side) is laid out in the center of the site. Finally, the cables to the transmitter coil and the receiver coil(s) are routed back to the data acquisition system. To protect the system from the elements, the equipment will likely be placed inside a van or small truck placed at a sufficient distance from the site so as not to cause any interference.

At each station in the grid, the receiver coil is carefully placed in the same orientation (for example, with respect to North) and leveled. The receiver coils are mounted on a tripod which includes a two axis bubble level that is used in conjunction with adjustable length legs for leveling at each location. The elevation of the center of the coils is measured and recorded. The 3-axis time series data is then collected and plotted on a semilogarithmic scale; visual examination is usually sufficient to assess the signal-to-noise level and overall quality of the data. Noise reduction is most easily done by averaging data from several pulses. The optimal number of pulses, which strikes a balance between signal-to-noise and data acquisition time, is usually between 10 and 30 pulse sequences. The noise level after averaging is easily monitored immediately after each acquisition so that the number of pulses can be changed if necessary.

Each site will be surveyed at two levels of detail. First, each station on the one-meter grid will be measured and the data processed to locate anomalous areas with above average readings (signal amplitude and decay constant). The magnetometer will also scan the area, and be used in conjunction with the PEMI for identification of areas containing possible anomalies. To interpret the responses from anomalous areas, a finer grid of data will be required, usually in the form of two perpendicular profiles crossing in the vicinity of the anomaly. Depending on the sharpness of the response, the second grid may be as finely sampled as to have stations every 25 cm, for a total of up to twenty additional stations per anomaly.

Finally, the data from the fine grid is processed to determine the decay constant characterizing the target conductor and the spatial response of the target. The latter is fit to a PEMI model based on a simple ring conductor to give an estimate of target position and orientation information.

Section VI Time Table

Setting up the coordinate system and installing the transmitter loop is expected to take about two hours. During this period a quick magnetometer scan of the area will be taken. At each station, the PEMI sensor is expected to take between one and two minutes to record, leading to an estimated time for the coarse survey of a site of about 4 to 6 hours. Once the coarse site data is collected, the data is processed to find any anomalies. Each anomaly is expected to take about one hour to measure in detail. The rest of each day will be used to process the data from the finer grid.

Section VII Expected Results

The data can be processed in the field to obtain a good assessment of the data quality and to provide a first cut interpretation of the measurements. A more careful study of the data will be performed upon returning to Seattle.

The expected targets are UXO, with sizes possibly varying between 55 mm and 155 mm mortars, as well as some larger bombs. Also possible are bits of shrapnel and other metallic debris. The targets are not expected to be deeper than a meter or two at most. The number of targets in each site and their orientation and condition are unknown. The time series processing will lead to an estimate of the decay time constant which will provide the classification information for the object. The spatial response will provide an estimate of the position of the object, to be verified by NAVEODTECHDIV. Past experience has shown that the precision of the estimate can be within 10 cm of the true location, but has rarely been more than 30 cm in error. The tilt angle estimate is within 10 degrees for the 155 mm and 122 mm UXO previously tested. The pointing angle exhibits similar accuracy with the exception for the ambiguity in pointing angle when the tilt is near zero.

Section VIII Pass/Fail Criteria

Pass/fail criteria do not apply in this test unless NAVEODTECHDIV desires to compare actual positions of UXO known to be buried on the test sites with the interpretations provided via the collected PEMI data. The results for each site will include a map of the locations of detected conductors and a table listing the specific positions obtained from the model inversion, as well as the size estimate of the object, or its identification if it falls into the class of UXO previously studied in the first test, as well as some measure of the confidence with which the time constant (from which identification is derived) is estimated.

Section IX Hold Test Criteria

The main impediment to proceeding with the test is equipment failure. Most components of the PEMI system have replacement spares or backup devices. The Geonics transmitter is a rugged and reliable piece of field equipment, but is a critical part of the system. Obtaining a replacement would probably take two days, subject to availability during a busy time for geophysical field work.

Severe weather could also pose a problem in that wind and rain impact would perturb the sensor coils and add noise to the data. Steady, gentle rain would not be a limitation other than making the work less pleasant for the field crew. Lightning is a hazard to both field crew and equipment, and operation would be suspended until a thunderstorm passes. Some equipment may be disconnected during a lightning storm to protect it in the event of a nearby strike.

In the event of weather induced interruptions to the demonstration, the test plan may be altered. Priority will be given to completing surveys at all three sites. This may be accommodated by reducing the spatial density of the test samples with an accompanying decrease in object location and identification accuracy. However, this objective must be balanced against the need for acquiring an adequate amount of data at each site for reliable PEMI performance

Section X Test Site Requirements

The NAVEODTECHDIV sites must be clearly marked and clear of tall grass. Any coordinate system used by NAVEODTECHDIV should also be clearly identified. Access to the survey site must be provided by NAVEODTECHDIV for at least 8 hours per day, but preferably with no time limitation. It is desired to leave the equipment and one vehicle on site, and commute to

the site using a second vehicle. Demonstration of the PEMI system operation can be accommodated at any time once it is operational; some advance notice is preferred.

Section XI Test Plan Change Authorization

Upon NAVEODTECHDIV's request, changes to the basic elements of the test plan will be made, provided such changes do not alter the one week test duration. It is also requested that NAVEODTECHDIV allow changes to the test plan if unexpected circumstances prevent carrying out the test as described above.

Section XII Post Test Evaluation

All equipment will be recovered from the site following completion of the test. The final report submitted to NAVEODTECHDIV at the end of the program will include detailed and careful processing and interpretation of the data. Unless given actual UXO position data by NAVEODTECHDIV, no quantitative evaluation of the accuracy of the results can be provided, aside from reporting on the signal-to-noise levels and their impact on the data interpretation.
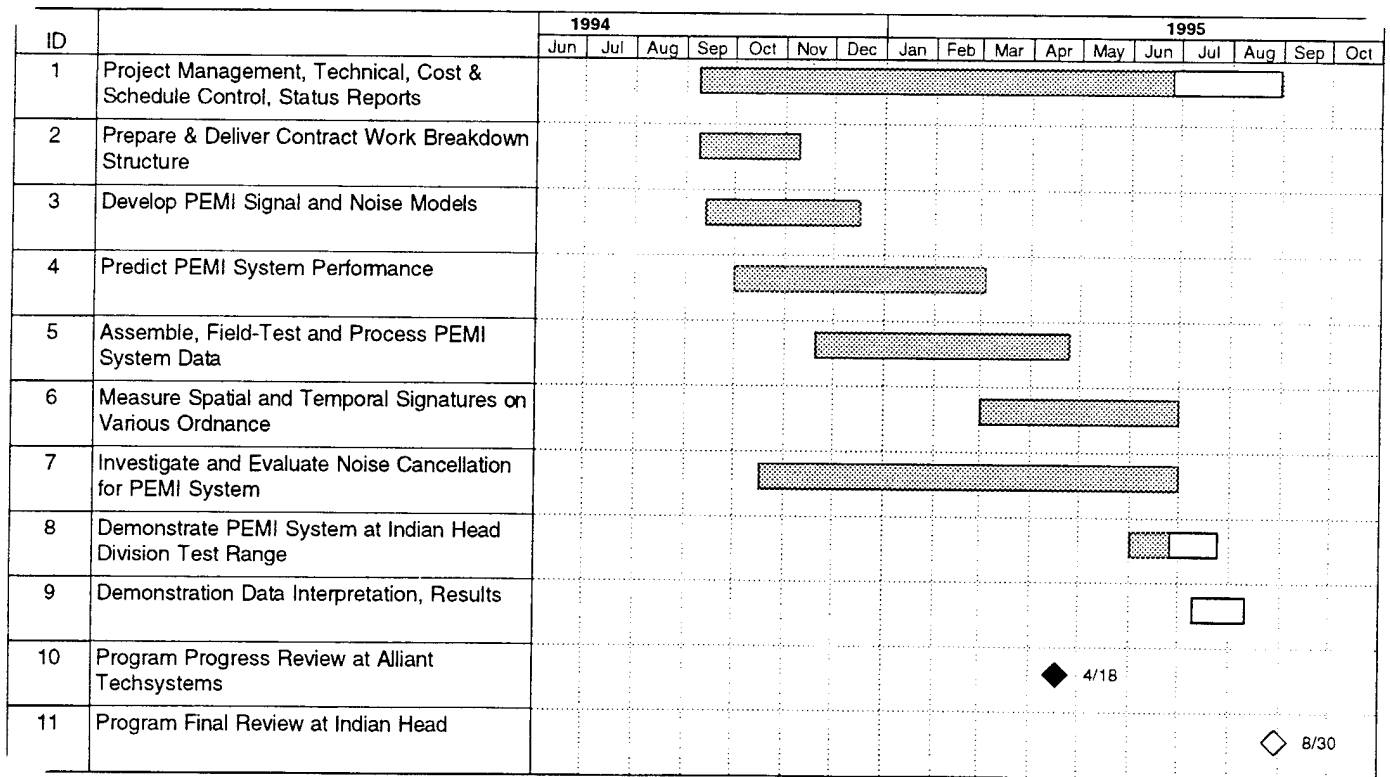
PEMI PROGRAM SCHEDULE

Figure 1: Program Schedule

Pulsed Electro-Magnetic Induction (PEMI)
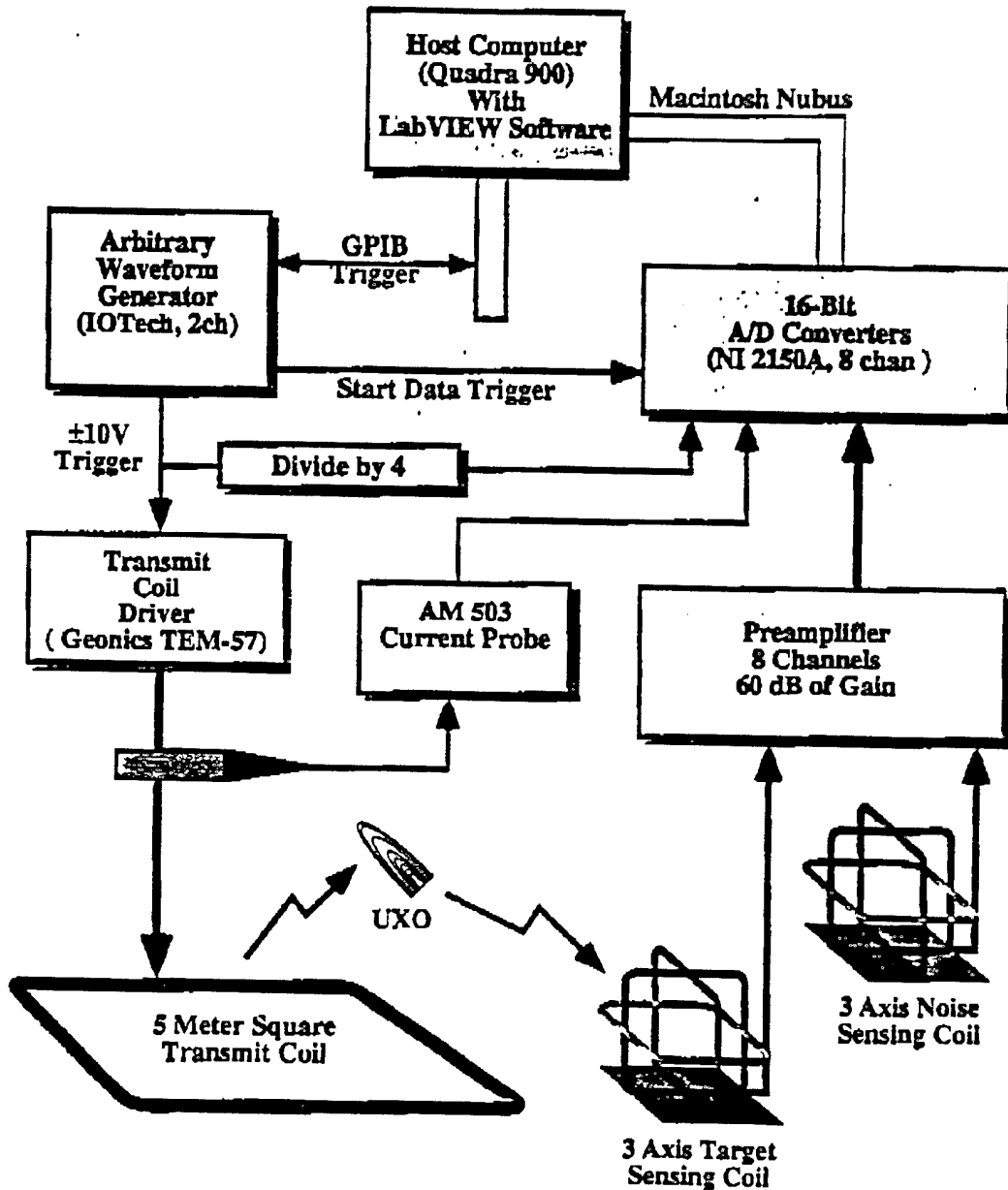## APL Data Collection Hardware Block Diagram

Figure 2: Data Acquisition Hardware Block Diagram

PULSED ELECTROMAGNETIC INDUCTION (PEMI)
N00174-94-C-0083

$\mathbf{P}$ulsed $\mathbf{E}$lectro-$\mathbf{M}$agnetic $\mathbf{I}$nduction (PEMI)
APL Data Collection Software Block Diagram

Enter Test
Setup Data
&
Target Data

Do for N LOOP

Setup 16-Bit
A/D Converters

Trigger Arbitrary
Waveform
Generator
Over GPIB

Hardware Trigger
A/D Converters
From DAC488

Collect and Average
Data
8 Channels

Find± Pulse Pairs
Process &Exponential
Fit Data

Write Header File

Plot target
data & Fit Data

Write Data File

Plot Drive Current
And X:Y ratio

Write Raw Data
File
for All Channels
If Requested

Plot Raw Data
for All Channels
If Requested

Figure 3: Data Acquisition Software Block Diagram

C.II

Appendix A: Equipment Description

The PEMI hardware is composed of three principal parts: the PEMI transmitter, the receiver, and the data acquisition computer system. A block diagram of the PEMI hardware is shown in Figure 2. The data processing is done on a separate Macintosh computer, using programs written primarily in MATLAB.

Data Acquisition System (DAS)

Computer

The heart of the DAS is a Mac Quadra 900 computer with National Instruments NB-A2150 analog to digital converter cards, and a GPIB interface card which allows remote control of the receiver amplifiers and the transmitter trigger waveform generator. The system is controlled by a program written in LabVIEW, a graphical instrument control language available from National Instruments. This program controls the entire data acquisition process, including sending out the transmitter triggers, digitizing the amplified receiver voltages, displaying the data upon acquisition, and finally storing the data to disk. A software block diagram is shown in Figure 3.

AC Power Supply

A portable generator is required to provide AC power to the two computers, the transmitter and the various other components of the data acquisition system. A 1 kW portable generator shall be acquired in Seattle and shipped to the test site with the rest of the PEMI instrumentation. A long power cord (700 ft) will help reduce the electromagnetic noise from the unit.

Miscellaneous Test Equipment

An oscilloscope, a function generator, a power supply, and a frequency counter are included in the list of ancillary laboratory equipment needed for verifying that the system is functioning properly, or to repair it in the event of a failure.

Transmitter

Geonics TEM-57

The TEM-57 is a commercially available transmitter, designed for exploration geophysics application in mineral prospecting and hydrology. The transmitter establishes a DC current on the order of 20 Amps in a large loop of wire laying on the ground and then sharply turns off this current to create an electromagnetic pulse. The transmitter is controllable by an external trigger waveform as done in this PEMI system, or by an internal crystal clock. For safety, only 20 volts are supplied to the coil terminals, requiring a low impedance wire loop.

Transmitter coil

The coil must be designed to have about 1 ohm resistance. In this case, a 5 meter square loop is used, comprised of 14 turns of number 8 copper wire. Standard insulated household

wire is well suited to this application and poses no risk to field operators because of the low voltages used.

IOTech Arbitrary Waveform Generator

The IOTech is a programmable waveform generator, used to trigger the transmitter at precise time intervals. Flexible programming of these timing waveforms allows cancellation of specific noise frequencies such as power line noise. The IOTech is controlled by the PEMI LabVIEW program and programmed over the GPIB bus.

Receiver

Receiver coils

The original plan was to use receiver coils manufactured by Geonics, but these proved (in the first test) not to be practical for this application. Consequently, two 3-axis sensors using 200 turns of 24 gauge wire wrapped around a square frame 50 cm on a side were built. Three perpendicular concentric coils and a simple terminating circuit make up each sensor. The sensor is mounted on a platform with a bubble level and adjustable legs to make leveling quick and easy.

PF filter/amplifier

The Precision Filters filter/amplifier is a multi-channel programmable signal conditioning instrument. It is also controlled by the PEMI LabVIEW program, and programmed over the GPIB bus.

Pre amplifier

The Precision Filters unit was not available at the time of the first experiment, and a simple 8 channel preamplifier was built. It will only be used as a backup in this demonstration.

Additional Sensors

Magnetometer

To augment the PEMI sensor in the rapid detection of anomalies a commercial magnetometer will be used. The GSM-19 is a portable, high sensitivity, Overhauser effect total field magnetometer with an absolute accuracy of 0.2 nT and resolution of 0.01 nT.

This page is intentionally left blank

10.   Appendix D: References

References

[1] Kaufman, A.A., "Frequency and transient responses of electromagnetic fields created by currents in confined conductors," Geophysics vol. 43, pp. 1002-1010, 1978

[2] Mc Neill, J.D., "Application of transient electromagnetic techniques," Technical Note TN-7, Geonics Limited, Mississauga, Ontario, Canada, 1980.

[3] Kaufman, A.A., "Resolving capabilitites of the inductive methods of electroprospecting," Geophysics, vol. 43, pp 1392-1398, 1978

[4] Stratton, J.A., "Electromagnetic Theory," McGraw Hill, 1941

[5] Kaufman, A.A. & Keller, G.V., "Frequency and transient soundings," Elsevier Scientific, 1983

[6] Mc Neill, J.D., R.N. Edwards, and G.M. Levy, "Approximate calculations of the transient electromagnetic response from buried conductors in a conductive half space," Geophysics Vol. 49, pp. 918-924, 1984

[7] Levenberg, K. "A Method for the solution of certain nonlinear problems in least squares". Quart. Appl. Math., 2:164-168, 1944

[8] Marquardt, D.W. "An algorithm for least squares estimation of nonlinear parameters", J. Soc. Industrial and Applied Math., 11:431-441